

DEVELOPMENT OF A MULTIFUNCTIONAL BIOSENSING PLATFORM WITH
APPLICATIONS ACROSS VARIOUS CONSUMER
MARKETS AND INDUSTRIES

by

Hunter Stevenson

APPROVED BY SUPERVISORY COMMITTEE:

Dr. Shalini Prasad, Chair

Dr. Allison Case

Dr. Danieli Rodrigues

Dr. Todd W. Polk

Copyright 2019

Hunter Stevenson

All Rights Reserved

To my partner Michael Cole: You have sacrificed so much to help achieve my dreams,
and I can't wait to repay the favor in our next adventure.

&

To my parents Clint and Deena Stevenson and my sister Kendra Miller:

Each of you has shown me to find passion in my work and keep my sights set on the stars.

DEVELOPMENT OF A MULTIFUNCTIONAL BIOSENSING PLATFORM WITH
APPLICATIONS ACROSS VARIOUS CONSUMER
MARKETS AND INDUSTRIES

by

HUNTER STEVENSON, BS

DISSERTATION

Presented to the Faculty of
The University of Texas at Dallas
in Partial Fulfillment
of the Requirements
for the Degree of

DOCTOR OF PHILOSOPHY IN
BIOMEDICAL ENGINEERING

THE UNIVERSITY OF TEXAS AT DALLAS

May 2019

ACKNOWLEDGEMENTS

I would like to first express my deepest thanks to my advisor, Dr. Shalini Prasad, for guiding me along this journey within the Biomedical Microdevices and Nanotechnology Laboratory over the past 3.5 years. I am so thankful for all the opportunities she has provided me to grow and learn as a scientist and as a person. She was so invested in my education, even before I was a student at UTD, always providing me the spark to ignite my passion for research. She has taught me to push my boundaries beyond my comfort zone and helped me foster confidence in everything I do. It wasn't always an easy process and there were times where I questioned my position here, but Dr. Prasad was always accommodating and encouraging me to strive for excellence. Thank you to the rest of my advisory committee for assisting me on my journey, with a particularly special thank you to Dr. Case for not only assisting me in my research but also being such a wonderful professor to assist throughout my time as a TA here at UTD.

I also would like to thank my Biomedical Microdevices and Nanotechnology Laboratory (BMNL) teammates, both past and present, who have been an amazing support system. I'd like to personally thank Jordan Pin, Amanda Bacon, Varsha Thomas, Faysal Anis, Kathy Joseph, and all the other undergrads that have passed through BMNL on my projects. I wish you all the best in your future research and careers. I hope you walk away from your time in the lab proud of what you have accomplished. And I hope you learned a few things along the way. I've always loved being a mentor/teacher first and foremost, and I hope that you enjoyed (and continue to enjoy for some) your time in the lab. I would not have gotten here without all your help. I'd like to also thank David Kinnamon for being a friend and second opinion on so many of my projects. You've been more support than you know.

Finally, I'd like to thank my partner in life, Michael Cole. His love and support has been unwavering throughout my graduate school journey. I cannot wait to see what is next in store for us.

November 2018

DEVELOPMENT OF A MULTIFUNCTIONAL BIOSENSING PLATFORM WITH
APPLICATIONS ACROSS VARIOUS CONSUMER
MARKETS AND INDUSTRIES

Hunter Stevenson, PhD
The University of Texas at Dallas, 2019

Supervising Professor: Dr. Shalini Prasad

The purpose of this work is to develop a point-of-use affinity-based biosensing platform capable of detecting biomarkers across complex matrices – ranging in electrolyte and macromolecule composition – with applications in consumer industries and regulatory marketspaces. This work focuses on the sensor and hardware development process to promote highly sensitive biomarker detection. First, this work explored how to enhance sensor performance while maintaining a compact design. The ideal placement of the electrodes was determined to stabilize the biosensor's baseline electrochemical characteristics. Additionally, the signal response was monitored with varying input signals and electrolyte constituency. Next, interactions between the sensor and target biomarker were explored in the presence of complex matrices. Both capacitive and resistive responses were recorded to identify the best detection modality for each biomarker/matrix combination. Last, the sensor performance was evaluated to predict the presence of the biomarker in each complex matrix. A limit-of-detection was identified for each biomarker/matrix combination, and a model was erected to accurately predict the presence of the biomarker. The sensor platform demonstrated stable faradaic detection of GMO proteins in plant and food extracts; non-faradaic detection of two strains of wheat viruses in reconstituted plant samples; non-faradaic detection of antibiotics in meat; as well as non-faradaic detection of a psychoactive marijuana compound within human saliva. This platform displayed excellent translatability when exploring numerous biomarkers in an array of complex matrices by leveraging a more intuitive understanding of the electrode-electrolyte interface and defining a systematic approach for evaluating key optimization parameters of electrochemical biosensors.

TABLE OF CONTENTS

ACKNOWLEDGEMENTS	v
ABSTRACT	vi
LIST OF FIGURES	xii
CHAPTER 1 INTRODUCTION	1
1.1 Electrochemical Biosensors	2
1.2 Electrochemical Detection Techniques	6
1.2.1 Faradaic Biosensors	6
1.2.2 Non-Faradaic Biosensors	6
1.2.3 Open Circuit Potential	8
1.2.4 Cyclic Voltammetry	8
1.2.5 DC Bias	12
1.2.6 Capacitive Spectroscopy	13
1.3 Buffer Complexity	16
1.4 Multifunctional Biosensor	17
1.5 References	18
CHAPTER 2 THE ANATOMY OF AN ELECTROCHEMICAL BIOSENSOR	20
2.1 Abstract	20
2.2 Design Challenges for Point-of-Care Biosensor Platforms	20
2.3 Current Affinity Biosensor Design Methodology	21
2.3.1 Biosensor Stability & Longevity	21
2.3.2 Biosensor Sensitivity & Specificity	21
2.4 Assessing Current Biosensor Geometries	23
2.5 Improvements to Affinity Biosensor Design Methodology	24
2.5.1 Sensor Fabrication	25
2.6 Computational Modeling to Investigate Biosensor Stability	26
2.6.1 Finite Element Analysis to Select Optimal Counter Electrode Placement	27
2.7 Electrochemical investigation of biosensor stability	30
2.7.1 Open Circuit Potential Evaluation of Sensor Stability	30

2.7.2 Faradaic Response Characterized by Cyclic Voltammetry	30
2.7.3 Faradaic Electrochemical Impedance Spectroscopy	32
2.7.4 Down-Selection of the Final Biosensor Design	32
2.8 Electrochemical Investigation of Biosensor Sensitivity.....	32
2.9 Effect of Buffer Ionicity and Applied DC Biases	35
2.9.1 Impact of buffer ionicity on non-Faradaic biosensing.....	35
2.9.2 Applied DC Bias effect on SAM penetration.....	37
2.10 Conclusion.....	39
2.11 Author Contributions	40
2.12 Declaration of Conflicting Interests	40
2.13 Funding.....	40
2.14 References	41
CHAPTER 3 GMO BIOSENSOR.....	44
3.1 Abstract	44
3.2 Introduction	44
3.3 Materials & Methods.....	47
3.3.1 Sensor Fabrication Process.....	47
3.3.2 Functionalization of Electrode Surface for the Detection of Bt-Crystal Proteins	47
3.3.3 Preparation of Wheat Leaf Extracts and Corn Flour Samples.....	48
3.3.4 ELISA Analysis of Cry1Ab and Cry1F Proteins in Wheat Leaf Extracts.....	48
3.3.5 Characterization of Electrode Surface Modifications by Fourier-Transform Infrared Spectroscopy (FTIR) Analysis	49
3.3.6 Evaluation of Dose-Dependent Response via Cyclic Voltammetry.....	52
3.3.7 Evaluation of Dose-Dependent Response via Electrochemical Impedance Spectroscopy.....	53
3.4 Results & Conclusions	54
3.4.1 Evaluation of Input Cyclic Voltammetry Parameters.....	54
3.4.2 Analysis of Dose-Dependent Response via Cyclic Voltammetry in 1x PBS.....	55
3.4.3 Analysis of Dose-Dependent Response via Electrochemical Impedance Spectroscopy in 1x PBS.....	57

3.4.4 Analysis of Dose-Dependent Response via Cyclic Voltammetry in Corn Flour and Wheat Leaf Extracts	58
3.4.5 Analysis of Dose-Dependent Response via Electrochemical Impedance Spectroscopy in Corn Flour and Wheat Leaf Extracts	61
3.4.6 Hand-held Electronics Platform for Dose-Dependent Response via Cyclic Voltammetry	62
3.5 Discussion	63
3.5.1 Future Work	64
3.6 Statistical Analysis	65
3.7 References	66
CHAPTER 4 WHEAT VIRUS SENSOR	68
4.1 Abstract	68
4.2 Introduction	68
4.3 Experimental Section	70
4.3.1 Sensor Fabrication Process	70
4.3.2 Electrochemical Evaluation of Biosensor Surface Modification via Electrochemical Impedance Spectroscopy	71
4.4 Results and Discussion	72
4.4.1 Antibody Saturation	72
4.4.2 Calibrated Dose Response	72
4.5 Conclusion	76
4.5.1 Future Work	76
4.6 References	77
CHAPTER 5 ANTIBIOTICS SENSOR	79
5.1 Abstract	79
5.2 Introduction	79
5.3 Experimental Section	83
5.3.1 Sensor Fabrication Process	83
5.3.2 Electrochemical Evaluation of Biosensor Surface Modification via Electrochemical Impedance Spectroscopy	84
5.4 Results and Discussion	84

5.4.1 Characterization of Electrode Surface Modifications by Fourier-Transform Infrared Spectroscopy (FTIR) Analysis	84
5.4.2 Electrochemical Evaluation of Biosensor Surface Modification via Electrochemical Impedance Spectroscopy	86
5.4.3 Analysis of Dose-Dependent Response via Electrochemical Impedance Spectroscopy in 1x PBS	88
5.4.4 Analysis of Dose-Dependent Response via Electrochemical Impedance Spectroscopy in Turkey Meat Samples	90
5.5 Conclusions	91
5.5.1 Future Work	92
5.6 References	93
CHAPTER 6 THC SENSOR	95
6.1 Abstract	95
6.2 Introduction	95
6.3 Materials & Methods	98
6.3.1 Sensor Fabrication Process	98
6.3.2 Zeta Potential Evaluation as a Function of pH for the THC-BSA Hapten	98
6.3.3 Evaluation of Dose-Dependent Response via Electrochemical Impedance Spectroscopy	99
6.3.4 Optimal Operating Frequency Selection for Electrochemical Impedance Spectroscopy Experiments	99
6.3.5 Binary Classification of THC +/- Human Saliva Samples	101
6.4 Results & Discussion	105
6.4.1 Characterization of Electrode Surface Modifications by Fourier-Transform Infrared Spectroscopy (FTIR) Analysis	105
6.4.2 Analysis of Zeta Potential as a Function of pH for the THC-BSA Hapten	106
6.4.3 Analysis of Dose-Dependent Response via Electrochemical Impedance Spectroscopy	107
6.4.4 Human Saliva Data Correlation	109
6.4.5 Optimal Operational Frequency Selection via FCBF	113
6.4.6 Binary Classification of THC +/- via Logistic Regression	115
6.4.6 Binary Classification of THC +/- via Support Vector Machines	118

6.5 Conclusion.....	121
6.5.1 Future Work.....	121
6.6 References	123
CHAPTER 7 CONCLUSION & FUTURE WORK.....	126
BIOGRAPHICAL SKETCH	127
CURRICULUM VITA	

LIST OF FIGURES

Figure 1.1. Simplified schematic of a potentiostat.	5
Figure 1.2. Cartoon schematic representation of the electric double layer on a polarized metal electrode.	7
Figure 1.3. A typical (a) input excitation signal beginning at 0.2 V vs Ref. at a scan rate of 10 mV/s and a switching potential of -0.4 V, and (b) the corresponding output voltammogram in the presence of a redox reagent with extracted peak cathodic, i_{pc} , and anodic, i_{pa} currents.	9
Figure 1.4. Randle’s Equivalent Circuit to describe interfacial and bulk impedance phenomena within an electrochemical cell.	10
Figure 1.5. (a) Nyquist and (b) Bode magnitude and phase plots for both non-faradic and faradaic responses. ¹⁷	12
Figure 1.6. Cartoon demonstrating the dielectric relaxation process of a self-assembled immunoassay in response to an applied AC signal.	14
Figure 1.7. Example Nyquist Capacitance Plot with a description for each term and its representative dominating electrochemical process.	15
Figure 2.1. Schematic showing each iteration with the CE (a) offset at 135°, (b) 180°, and (c) 225° with respect to the positive x-axis (d) A plot of the OCP vs time for the CEX.225 configurations.	25
Figure 2.2. Cartoon schematic of the affinity biosensor. A 25 nm chromium adhesion layer was deposited on to the glass substrate, followed by 125 nm of gold. DSP was used to functionalize the WE surface to capture the BSA proteins diluted in 1x PBS. Insert: Photograph depicting the fabricated CE1.225 sensor iteration with dime for size comparison.	26
Figure 2.3. (a) Schematic of Finite Element Analysis geometry with applied boundary conditions for the CE1.225 configuration (b) Contour Plot demonstrating isopotential surfaces within the electrolyte (c) Potential Distribution at the RE across all configurations (d) Surface plot showing the distribution of current density and arrow plot representing electric field distribution and direction (e) and (f) Line plots demonstrating the current density distribution along the dashed lines shown in (a). The dashed line color in (a) correspond to the graph insert label color in (e) and (f) indicating the direction.	28
Figure 2.4. Cyclic Voltammogram demonstrating electrode stability in the presence of $K_3[Fe(CN)_6]$ for the CE1.235 configuration (a) across 3 cycles for the CE1.225 iteration and (b) across the CEX.225 iterations. (c) Table 2.1 summarizing faradaic response indicating reversibility of the system.	31
Figure 2.5. EIS data presented from the CE1.225 iteration. (a) Bode Plot of BSA dose-response with (b) Zoomed in view of around 100 Hz. Corresponding (c) Nyquist Plot for BSA	

dose-response. (d) Impedance values at 100 Hz for BSA calibrated dose response with DSP functionalization and no DSP surface functionalization.	34
Figure 2.6. (a) Plots of fitted solution resistance and double layer capacitance (CPE) across BSA concentrations (n=3) <i>insert</i> : Modified Randle’s Equivalent circuit used to fit experimental data across BSA doses (c) Plots of fitted solution resistance (Rs) values for each sensor iterations (n=3).	35
Figure 2.7. Bode Modulus and Phase plots for PBS dilutions between 0.1x and 1x for both (a) an unmodified sensor and (b) a DSP functionalized sensor, (c) Z^{*} values at 1 MHz across PBS dilutions for both unmodified and DSP functionalized sensors, (d) change in imaginary impedance at 1 Hz between unmodified and DSP functionalized sensors.	36
Figure 2.8. (a) Cyclic Voltammogram in the presence of 1x PBS. EIS measurements in the presence of 1x PBS at $VDC = 0.2 V$, $VDC = 0 V$, & $VDC = -0.3 V$ for (b) an unmodified sensor (c) a DSP functionalized sensor, and (d) a DSP functionalized sensor after introducing 10 ng/mL BSA.	38
Figure 3.1. FTIR spectra of (a) DSP crosslinker immobilized on Au surface, (b) anti-Cry1Ab immobilized on DSP crosslinker, and (c) anti-Cry1F immobilized on DSP crosslinker.	50
Figure 3.2. Voltammograms recorded in the presence of ferricyanide at varying scan-rates (25 mV/s – 200 mV/s). <i>Insert</i> : Linear correlation between current and the square root of the scan-rate.	55
Figure 3.3. CV and EIS response in 1 mM ferricyanide post incubation of various Bt-Cry protein concentrations diluted in PBS. Peak cathodic current versus concentration of both (a) Cry1Ab and (b) Cry1F with voltammogram inserts demonstrating current response across Bt-Cry protein concentration. Change in R_{ct} versus concentration of (c) Cry1Ab and (d) Cry1F with Nyquist plot insets demonstrating the frequency spectrum across Bt-Cry protein concentration. Arrows on all insets represent increasing Bt-Cry protein concentration.	56
Figure 3.4. Charge transfer resistance plotted against incubation times for non-GMO wheat leaf extract samples on the functionalized sensor (n=3 per time point).	58
Figure 3.5. CV and EIS response in 1 mM ferricyanide post incubation of various Bt-Cry protein concentrations in corn flour dissolved in PBS. Peak cathodic current versus concentration of both (a) Cry1Ab and (b) Cry1F with voltammogram inserts demonstrating current response across Bt-Cry protein concentration. R_{ct} versus concentration of (c) Cry1Ab and (d) Cry1F with Nyquist plot insets demonstrating the frequency spectrum across Bt-Cry protein concentration. Arrows on all insets represent increasing Bt-Cry protein concentration.	59
Figure 3.6. CV and EIS response in 1 mM ferricyanide post incubation of various Bt-Cry protein concentrations in wheat leaf extract diluted in 1x PBS. Peak cathodic current versus concentration of both (a) Cry1Ab and (b) Cry1F with voltammogram inserts demonstrating current response across Bt-Cry protein concentration. R_{ct} versus concentration of (c) Cry1Ab and (d) Cry1F with Nyquist plot insets demonstrating the	

frequency spectrum across Bt-Cry protein concentration. Arrows on all insets represent increasing Bt-Cry protein concentration, (e-f) Absorbance results from commercially available ELISA kits.....	60
Figure 3.7. Circuit breakdown of the custom electronic platform: Triangle-wave generation via a digital-to-analog converter (red), attenuation of the signal (blue), potentiostat circuit for measuring the signal (orange), and level shifting and reporting (orange).....	61
Figure 3.8. (a) Visual comparison between CV outputs measured on custom (black) and Gamry (red) potentiostats, (b) Bland-Altman Plot comparing the difference in extracted peak current vs the average of extracted peak current for both potentiostats.	63
Figure 4.1. Sensor performance in EIS experiments across calibrated doses of WSSMV in 1x PBS. (a) Nyquist Impedance Plot across WSSMV doses, and (d) transformed Nyquist Capacitive Plot across doses. (c) Change in Z^* at 10 Hz with respect to antibody measurement for varying concentrations of WSSMV (blue) and for repeated 0-dose measurements (grey).....	74
Figure 4.2. Sensor performance in EIS experiments across calibrated doses of SBWMV in 1x PBS. (a) Nyquist Impedance Plot across SBWMV doses, and (d) transformed Nyquist Capacitive Plot across doses. (c) Change in Z^* at 10 Hz with respect to antibody measurement for varying concentrations of SBWMV (blue) and for repeated 0-dose measurements (grey).....	75
Figure 5.1. FTIR spectra of (a) DSP crosslinker immobilized on Au surface, (b) anti-ceftiofur antibody conjugated to DSP cross-linker.....	86
Figure 5.2. (a) Nyquist impedance plot (b) Bode Phase plot and (c) extracted Z^* values at 10 Hz for EIS measurements to validate the chemisorption of the immunoassay.	87
Figure 5.3. Calibrated dose response across varying concentrations of ceftiofur represented as (a) Nyquist capacitance plot and (b) percent change in impedance with respect to the antibody measurement at 10 Hz with SST in dark blue (n=4).....	88
Figure 5.4. Calibrated dose response across varying concentrations of ceftiofur in turkey meat samples represented as (a) Nyquist impedance plot and (b) Z'' at 10 Hz (n=3).....	90
Figure 6.1. Cost functions for Logistic Regression (black) and SVM piecewise approximation (red).....	103
Figure 6.2. Linearly separable example of <i>THC</i> +/- binary classification by SVM with the optimal hyperplane defined by the maximum-margin between the red & blue dashed lines.	104
Figure 6.3. FTIR spectra of (a) DSP crosslinker immobilized on Au surface, (b) anti-ceftiofur antibody conjugated to DSP cross-linker.....	106
Figure 6.4. Calibrated dose response represented as Nyquist complex impedance plots with calibrated dose response inset for (a) 1x PBS (b) synthetic saliva at pH of 6 and (c) synthetic saliva at pH of 4. All inserts represent the change in imaginary impedance (with respect to the 0-dose step) extracted at 10 Hz.....	109

Figure 6.5. Correlation heatmap of $Z *$ data between 1 Hz and 505 Hz.....	110
Figure 6.6. Correlation heatmap of Z'' data between 1 Hz and 505 Hz.	111
Figure 6.7. Correlation heatmap of $Z\phi$ data between 1 Hz and 505 Hz.....	112
Figure 6.9. (a) Violin plots displaying normalized distributions and (b) correlation heatmap displaying Pearson's correlation of the 5 features identified as most predictive by the FCBFK algorithm for the normalized to the antibody step.	114
The final three features selected after implementing the FCBF(K) algorithm were $Z *$ at 398.0 Hz, $\%dZ\phi$ (wrt synthetic saliva) at 198.6 Hz, and dZ'' (wrt antibody) at 9.9 Hz. Figure 10a shows that none of these features are correlated to one another while Figure 10b demonstrates the dispersion of the data points in the reduced feature space.....	115
Figure 6.10. (a) Correlation heatmap and (b) 3D scatter-plot of final three selected features after the FCBF & FCBFK algorithms.	115
Figure 6.11. Logistic Regression classification performance metrics. (a) ROC curve with TPR and FPR identified at thresholds 0.303 (dark blue) and 0.769 (light blue). (b-d) 2D cross-sections of the classification probability.....	116
Figure 6.12. Logistic Regression classification performance metrics. (a) ROC curve with TPR and FPR identified at thresholds 0.303 (dark blue) and 0.769 (light blue). (b-d) 2D cross-sections of the classification probability.....	117
Figure 6.13. Linear kernel SVM classification performance metrics. (a) ROC curve with TPR and FPR identified at thresholds 0.214 (dark blue) and 0.829 (light blue). (b-d) 2D cross-sections of the classification probability.....	119
Figure 6.14. Rbf kernel SVM classification performance metrics. (a) ROC curve with TPR and FPR identified at thresholds 0.621 (dark blue) and 0.797 (light blue). (b-d) 2D cross-sections of the classification probability.....	120

CHAPTER 1

INTRODUCTION

The field of biosensing emerged in 1962 when Clark and Lyons¹ demonstrated the first sensor to measure glucose levels in biological samples. Since then, the field has grown exponentially in both technology and biosensing applications.² Within the past 10 years, advances in biological techniques (e.g. antibodies, aptamers or nucleotides, peptide arrays, and molecule imprinted polymers) have enhanced biosensor selectivity and specificity – with sensors able to detect biomarkers down to the ng/mL range.^{2,3} Furthermore, the integration of novel nanomaterials in biosensors have improved on detection sensitivity by enhancing signal transduction through enhanced surface areas and more favorable biochemistries.³ Research facilities across the globe are focusing resources to implement new materials in new, highly sensitive biosensors. These powerful new resources have improved how humans interact with biological samples and drastically improved detection time and sensitivity.⁴

The field of biosensing is poised to change the landscape of diagnostic devices across not just healthcare, but marketplaces in every industry sector. In addition to health and wellness, research into biosensors encompasses agricultural to cosmetic to environmental applications. Biosensor variants – such as enzyme-based, tissue-based, immunosensors, and piezoelectric biosensors have been explored, each aiming to provide operational simplicity, low sensitivity, low-cost instrumentation, and/or miniaturization. While advances have been made in isolating and identifying biomarkers for a range of diagnostic purposes, next generation biosensor developers also seek to reduce complex instrumentation and generate responses within minutes of sample introduction at the point-of-use or point-of-care (POC).

To date, commercially available solutions for POC diagnostics are primarily driven by the detection of biomarkers using a combination of lateral-flow assays and colorimetric tests.⁵ Typically, this is achieved with reporting of the presence or absence of a target biomarker through a color change. In many cases, these dipsticks and lateral-flow assays offer only qualitative or (at

best) semiquantitative results.^{5,6} Over the past four decades, medical diagnostics has undergone a shift toward rapid, quantitative biomarker detection enabling POC-based biosensing.⁵ However these devices face challenges such as small volume samples, complex biological matrices, and very low biomarker concentrations.⁶ POC devices are poised to transform the healthcare landscape as better, novel materials are discovered to isolate the biomarker of interest and as more powerful detection methodologies are developed.

For lateral-flow devices, efforts are focused on developing next generation microfluidics to filter and direct analyte migration through microscopic fluidic channels⁷ while other affinity-based detection biosensors explore novel materials that reduce surface fouling (to increase signal specificity) and enhance the biomarker's affinity toward the recognition element (to increase signal specificity and sensitivity). The choice in biosensor substrate, for example, dictates surface chemical properties and can influence properties such as chemi- and physisorption.⁸ Additionally, strides have been made in developing novel materials to capture the biomarker of interest with high specificity and affinity.⁴

“Big Data” and learning algorithms have only recently started trickling into the diagnostics domain.⁹ As demand for ultra-sensitive, and highly accurate biosensors rises, more sophisticated analysis techniques must be explored, as sensitive electrochemical detection and quantification of biomarkers often involves highly complex, non-linear interactions.¹⁰ Machine learning allows for rapid analysis of these interactions while continually improving on the sensitivity of a platform as more data are gathered. Thus, as these analytical tools mature alongside the novel solutions to biomarker detection, industry providers can develop more powerful diagnostic platforms. This work explores combining data science and various machine learning tools to make predictions on a novel electrochemical biosensing platform.

1.1 Electrochemical Biosensors

The detection process for any biosensor consists of: biomarker recognition, signal transduction, and generation of a user-friendly output. An electrochemical biosensor utilizes an electrode transducer coupled to a biomarker recognition element. When a recognition event occurs, the

biochemical interaction near the electrode interface is transduced into an electrical signal through either amperometric, impedimetric, potentiometric, or coulometric transduction.¹ Electrochemical biosensors offer high sensitivity, low detection limits (often in the nanogram to picogram per mL range),⁵ and a wide dynamic range. Furthermore, their miniaturization, ease of fabrication, and scalability allow for easy use and low-cost production. Additionally, the direct conversion of the biosignal to an electrical output allows the sensor to be integrated with electronics for rapid, portable measurements. These factors have allowed electrochemical biosensors to play an integral part in simplifying diagnostics and POC devices. While electrochemical biosensors can be sensitive to environmental changes such as temperature and humidity, incorporating environmental controls or sensors in parallel can help control for variability in the response.

1.1.1. Two vs. Three Electrode Sensors

POC electrochemical biosensors often employ a coplanar, two-electrode design consisting of a Working Electrode (WE) and a Reference Electrode (RE) deposited onto a planar substrate. The electrodes are then connected to a potentiostat which applies and measures electrical signals across the electrode interfaces. The potentiostat controls the voltage difference between a WE and RE to make inferences about the electrochemical cell. The Gamry Reference 600 Potentiostat is a four-probe instrument, two of these probes (the Working and Counter) carry current while the other two probes (the Working Sense and Reference) measure voltage. These probes are connected in parallel or series across the electrodes to apply and measure signals within an electrochemical cell. The configuration of these four probes vary with the type of electrochemical cell being tested. The roles of the different electrodes and configurations are briefly described below:

Working Electrodes are where the reaction of interest occurs. These electrodes are the focus of an electrochemical experiment, and proper means of isolating and measuring the WE reaction must be taken. The WE typically consists of a current carrying probe (Working) connected in series with the Working Sense probe (where the potential is measured).

Counter Electrodes complete the circuit for current passing in or out of the cell. Typically, the Counter Electrode (CE) is a relatively inert material (e.g. gold, platinum or carbon) to ensure, when passing current, it does not interfere with the cell potential.

Reference Electrodes, as their name implies, serve as a potential reference point within the cell. To ensure sensor reliability, the RE should maintain a constant potential throughout the measurement. This is typically achieved by carefully placing the RE such that little to no current flows through it, and any current flowing through the system does not interfere with the RE's set potential.

Two Electrode Sensors: In the simplest electrochemical measurement, two electrodes are used. Each electrode carries current and measures the potential difference through the electrolyte. When interfacing with the potentiostat for a two-electrode sensor, the Working and Working Sense leads are connected in series to a WE and the Reference and Counter leads are connected to a second pseudo-RE. Two electrode experiments are often employed when the entire voltage is relevant (e.g. batteries, fuel cells) or when little faradaic currents are expected to pass across the electrode interfaces. In a two-electrode biosensor, the potential is measured at the WE against a set RE potential.

Three Electrode Sensors: Three electrode experiments are set up similarly to two electrode set-ups, however the Reference and Counter leads are connected to two different electrodes (the RE and CE respectively). The separation of these electrodes allows for currents to pass through the CE and isolate the RE from any currents flowing through the electrolyte. Three electrode set-ups allow for measurement of the potential changes at the WE (with respect to the RE) independent of any potential changes at the CE. This isolation offers an advantage over two electrode set-ups, in that reactions at the WE can be isolated from reactions occurring at the CE. Furthermore, this separation allows for both non-faradaic and faradaic measurement techniques. In Figure 1.1 a simplified potentiostat is depicted with a three-electrode set-up.

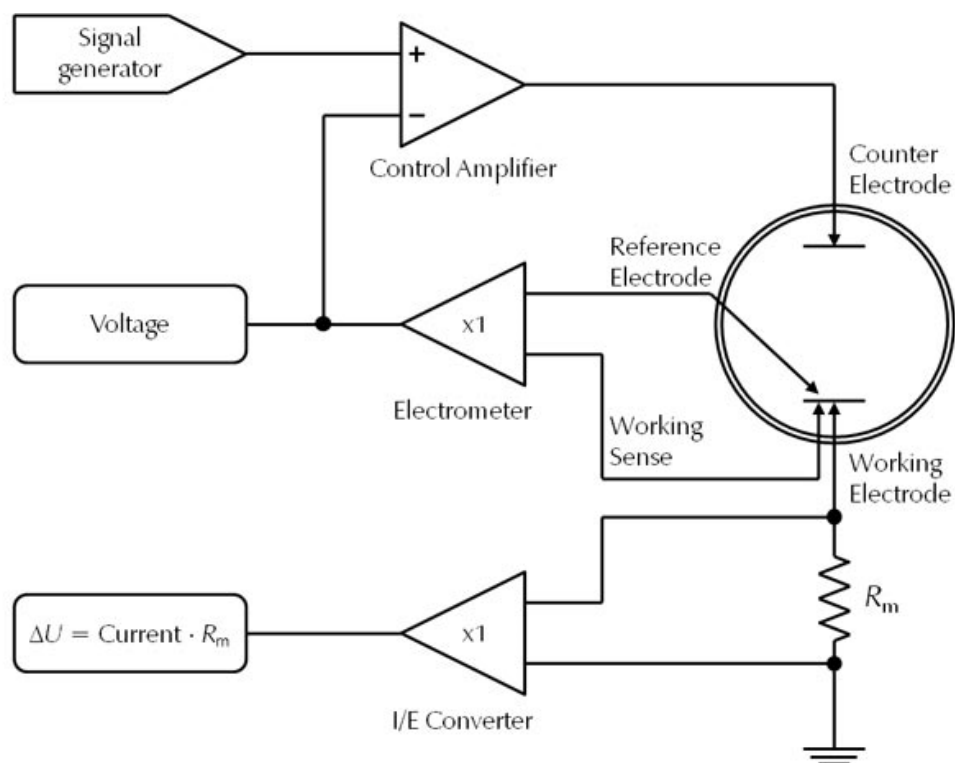


Figure 1.1. Simplified schematic of a potentiostat.

Most electrochemical biosensors utilize coplanar electrodes to limit design complexity, reduce sample volumes, and leverage established thin-film fabrication techniques.¹¹ These simple designs can also be integrated with electronics to perform rapid measurements for a POC system. However, two-electrode biosensors often suffer when sensing in complex matrices like plant extracts, food samples, and biofluids.¹² These complex matrices comprise of various anions and cations as well as an assortment of biological macromolecules and other particulate matter that often change from sample to sample. Varied ionic content will lead to conductivity and pH changes, while macromolecules can interfere with the sensor performance through surface fouling or other intermolecular interactions.^{13,14} Furthermore, complex matrices can carry redox active species, resulting in noisy faradaic charge transfer at the RE, altering its set potential.

1.2 Electrochemical Detection Techniques

1.2.1 Faradaic Biosensors

Faradaic biosensors detect charges transferred across the electrode-electrolyte interface resulting from a redox reaction. This charge transfer generates a measurable current at the Working Electrode that is equal to the sum of charges transferred across its interface. For affinity-based faradaic biosensors, the modification of the electrode surface with the immunoassay and subsequent binding of the targeted biomarker modulates the number of charges transferred across the electrode interface. This modulation depends on the conductivity of the immunoassay/biomarker and whether its presence will enhance or hinder charge transfer kinetics. While faradaic biosensing can be achieved through label-free techniques, it often is an indirect measurement of the biomarker as the additional redox probe is often required to perform the measurement. Nonetheless, faradaic biosensors offer high signal-to-noise outputs and relatively straightforward analysis through Randle's circuit fitting.

1.2.2 Non-Faradaic Biosensors

Non-faradaic biosensors rely on measuring changes in the interfacial capacitance near the electrode's surface. Whenever an electrolyte is in contact with a charged surface, the solvated ions will distribute in a predictable manner to shield the charges presented at the solid-fluid interface. The arrangement of these ions is often referred to as the electrical double layer (EDL) as depicted in Figure 1.2.

There are many models that attempt to describe the distribution of ions at this interface with the three most common being the Helmholtz, Gouy-Chapman and Stern models.¹⁵ The Helmholtz model is the simplest description of an electrode-electrolyte interaction; here the charges in a polarized electrode are balanced by the redistribution of ions in the electrolyte by an equal but oppositely charged ions. The attraction of counter-ions to the surface creates two layers of opposite charges at the interface – hence the name electric double layer. However, this model is an incomplete view of the EDL as it does not consider thermodynamic forces nor the ion's finite size.¹⁵

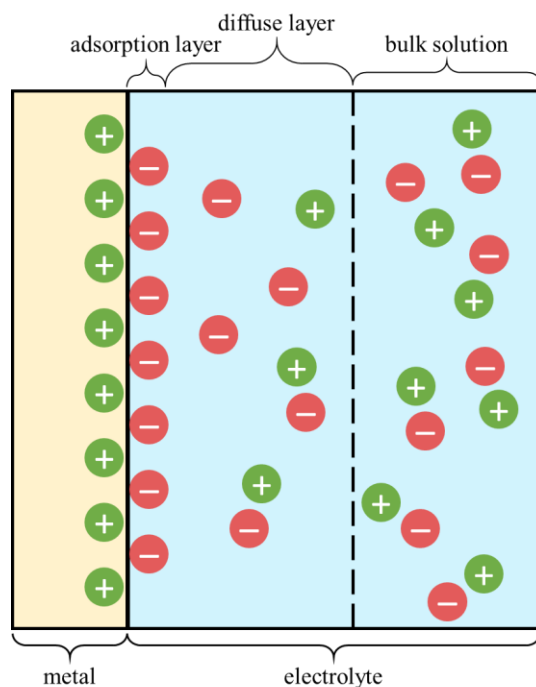


Figure 1.2. Cartoon schematic representation of the electric double layer on a polarized metal electrode.

Gouy-Chapman expand on the Helmholtz model to account for thermal motion of these ions and recognize that the distribution of ions shielding the polarized electrode can be described with a Boltzmann distribution (Equation 1.1):

$$n_i = n_i^0 \exp\left(-\frac{z_i e \phi}{kT}\right) \quad (1.1)$$

Where n_i^0 represents the concentration of the i^{th} ion in the bulk, e is the unit charge, z_i is the charge of the i^{th} ion, k is the Boltzmann constant, and T is the absolute temperature. The Stern model combines the Helmholtz model and the idea of thermal equilibrium as described by Gouy-Chapman by accounting for the ions' finite size. Stern describes the EDL as two regions – the Stern layer (or Helmholtz layer) which consists of compact immobile ions adsorbed to the electrode surface and the diffuse layer which is described by the Gouy-Chapman model.¹⁶ Electrochemical biosensors leverage ionic distributions as described by these three models in affinity-binding at the electrode surface. Binding events at electrode-electrolyte interface modulate

ion and charge distribution at the surface, allowing for sensitive and selective biomarker detection through double-layer capacitive or resistive measurements.^{17–19}

1.2.3 Open Circuit Potential

The Open Circuit Potential (OCP) is a thermodynamic parameter that indicates the tendency of the WE to participate in an electrochemical corrosion reaction with the surrounding medium. To measure the OCP, the potential of the WE is measured against the RE using a high-impedance voltmeter to ensure that no current flows between the electrodes. The OCP was measured to establish sensor stability, taken in the presence of 1× PBS for 1 hour to ensure steady state.

1.2.4 Cyclic Voltammetry

Cyclic Voltammetry (CV) is a common potentiodynamic technique used to study redox active species. More broadly, CV is used to monitor the diffusion of redox active species to the electrode-electrolyte interface as well as the electron charge transfer kinetics across the interface.²⁰ CV can also be used to study the electrochemical window of the system and any non-faradaic charging/discharging of the electric double layer. The excitation signal for CV and its expected faradaic response can be seen in Figure 1.3.

In CV, the potential between the WE and RE is ramped linearly versus time. Once the potential reaches a pre-defined maximum (or minimum) potential, it is ramped in the reverse direction until a set minimum (or maximum) potential is reached. For CV experiments on this platform, the potential was scanned from 0 V to either a 0.2 V or 0.4 V maximum, and then a –0.5 V minimum at a variable scan rate. The window was chosen to limit electrolyte breakdown and destruction of the electrodes.

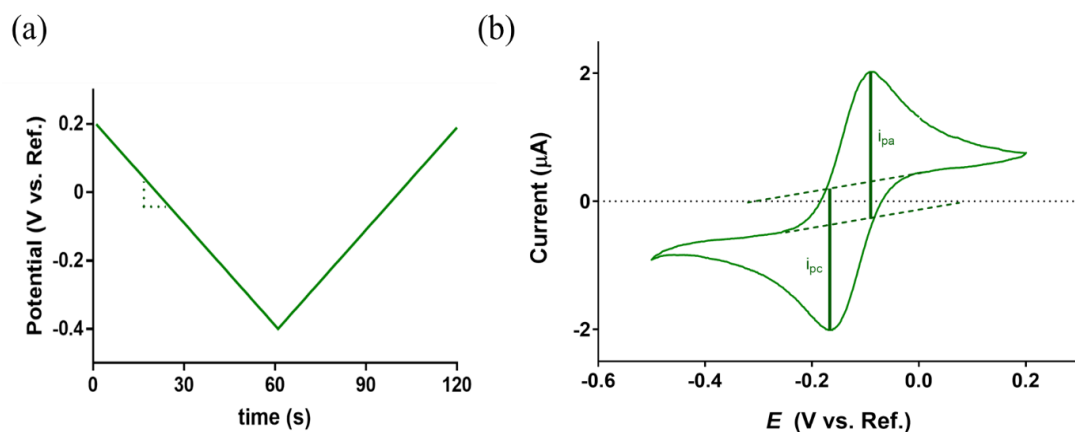


Figure 1.3. A typical (a) input excitation signal beginning at 0.2 V vs Ref. at a scan rate of 10 mV/s and a switching potential of -0.4 V, and (b) the corresponding output voltammogram in the presence of a redox reagent with extracted peak cathodic, i_{pc} , and anodic, i_{pa} currents.

When the potential is scanned, the ferricyanide molecule participates in a reversible, single-electron redox reaction. The kinetics of this reaction are seen in the cyclic voltammograms in Figure 1.3b. During the forward scan, oxidation of the ferricyanide resulted in the formation of a cathodic peak current, while the reverse scan reduced the probe, leading to an anodic peak.

1.2.5. Electrochemical Impedance Spectroscopy

Electrochemical impedance spectroscopy (EIS) is an experimental method of characterizing the electrochemical response to a small AC voltage excitation over a range of frequencies. EIS allows for the decoupling of the various electrochemical reactions taking place in the system through separation of the real and imaginary impedance spectrums.^{17,20} The input excitation signal is a sinusoidal AC voltage signal (often with a set DC bias) that is scanned across a chosen frequency range. The measured signal response is a phase shifted sinusoidal current, and taking the ratio of input to output allows for the calculation of the complex impedance spectrum using Equation 1.2:

$$Z = \frac{V}{I} = \frac{V_o \sin(\omega t) + V_{DC}}{I_o \sin(\omega t + \phi)} \quad (1.2)$$

Here, Z represents the complex impedance calculated from the ratio of V to I which are the excitation potential and measured current response respectively. V_o and I_o correspond to the magnitude of each AC signal, V_{DC} is the applied DC potential bias, ω is the frequency, and ϕ is

the phase shift in the signal. The concept of impedance extends ohmic resistance from DC circuit theory to AC circuits. Impedance is a complex number consisting of both real (ohmic resistance) and imaginary (reactance) parts.

When leveraging EIS for biosensors, at low frequencies interfacial properties dominate the electrochemical response while at high frequencies bulk phenomena tend to dominate. The nature of the low frequencies response is highly dependent on whether faradaic or non-faradaic EIS is being leveraged. Affinity binding in the presence of redox active species is detected through changes in faradaic charge transfer across the electrode-electrolyte interface,¹⁷ whereas non-faradaic EIS leverages changes in interfacial capacitance to determine targeted biomarker binding events.^{17,19}

To aid in the interpretation of the chemical processes an equivalent circuit can be used to fit the impedance spectrum. The most common equivalent circuit, the Randle's cell,¹⁵ consists of a solution resistance (R_s) in series with the parallel combination of a non-faradaic branch and a faradaic branch as seen in Figure 1.4.

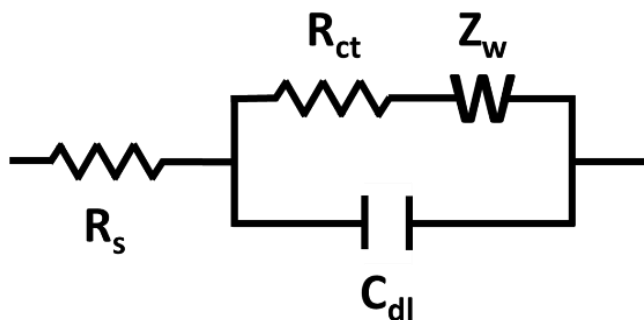


Figure 1.4. Randle's Equivalent Circuit to describe interfacial and bulk impedance phenomena within an electrochemical cell.

The non-faradaic branch consists of a double layer capacitance (C_{dl}) which describes the charging and discharging of the electric double layer at the electrode-electrolyte interface. The faradaic branch arises due to charge transfer across the interface and consists of a charge transfer resistance

(R_{ct}) and occasionally a Warburg impedance element (Z_w) which simply describes the diffusion of the charge carrying molecules from the bulk of the solution to the interface.

In non-faradaic EIS, the applied potential is selected as to not cause any charge transfer across the electrode-electrolyte interface. This results in a near infinite R_{ct} and the circuit can be simplified by removing the faradaic branch in the Randle's cell. This leaves just the solution resistance and double layer capacitance as the key parameters in non-faradaic EIS.

During faradaic EIS, the presence of a redox molecule and careful selection of a DC bias allows for the measurement of a finite R_{ct} . The charge transfer resistance is heavily dictated by the choice of electrode material. This work utilizes gold electrodes as gold is a conductive but relatively unreactive material, making it an excellent choice for the WE when measuring R_{ct} . Chemisorption of the immunoassay and subsequent binding of the relevant biomarker also has a significant role in altering the R_{ct} . As these molecules bind to the gold electrode, the available surface area decreases, and charge transfer is hindered, leading to an increase in R_{ct} . Additionally, the presence of these chemisorbed molecules can affect the diffusional properties of the redox molecule. This can be seen in the changes of Z_w . As more molecules bind to the electrode, the immunoassay increases the diffusion path to the electrode surface. This manifests as a shift to lower frequencies where the Z_w dominates.

A plot displaying the imaginary vs real components of impedance are called Nyquist plots and are often used to determine the nature of physical processes occurring both at the electrode-electrolyte interface as well as out in the bulk of the system. Bode plots are another common representation of the impedance data. As seen in Figure 1.5b both the modulus of the impedance and the phase angle are plotted vs the logarithm of the input frequency. Bode plots help identify at which frequency ranges capacitive or resistive processes dominate. When the phase angle is near -90° and the modulus is frequency dependent, capacitive effects dominate. When the phase angle is near 0° and the modulus is constant, resistive effects dominate the system.

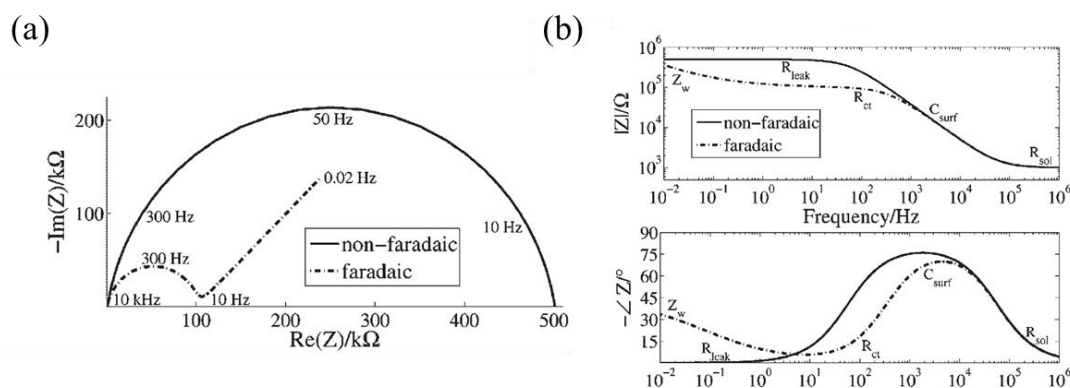


Figure 1.5. (a) Nyquist and (b) Bode magnitude and phase plots for both non-faradic and faradaic responses.¹⁷

1.2.5 DC Bias

In certain EIS experiments a DC bias may be applied in addition to the AC signal. In non-faradaic EIS a DC bias may be chosen to exploit a process where ions penetrate the self-assembled monolayer (SAM),²¹ while in faradaic EIS a DC bias is crucial to ensure regeneration of the redox molecule.¹⁷

SAMs are insulative in nature and can usually be modeled as a traditional Helmholtz capacitor model. However, at DC biases below some critical potential, V_c , SAMs will behave as leaky capacitors where defects (or pin-holes) in SAM spacing allow ions from the electrolyte to penetrate the monolayer, manifesting as a non-ideal behavior of the SAM permittivity.²¹ The flux of ions into or out of the film is highly dependent on SAM spacing on the electrode surface. Ionic ingress can contribute significantly to the overall capacitive response and scales with the magnitude of the DC bias.²¹ This leaky capacitance is exploited to enhance signal changes when detecting binding events of biomarkers to an immunoassay attached to the electrode surface.

In Faradaic EIS, the selection of a DC bias is dependent on the redox probe utilized for the experiment. With reversible reactions, a DC bias should be selected such that the conversion of the probe from reduced to oxidized state is in equilibrium. Applying a small AC signal at the equilibrium potential causes repeated switching between the forward and reverse reaction. This switching ensures regeneration of both reduced and oxidized states of the redox molecule such that neither is depleted throughout the experiment.²²

1.2.6 Capacitive Spectroscopy

This work explores capacitive and resistive contributions at the electrode-electrolyte interface primarily through EIS spectra analysis; however, the resolution between these two contributions can be difficult to distinguish during non-faradaic EIS. Changes in impedance spectra due to biomarker binding are not always intuitively resolvable depending on the nature of the support matrix and the biomarker of interest. To address the poor resolution, Capacitive Spectroscopy (CS) is employed to transform the complex impedance spectrum into a complex capacitance which highlights the storage characteristics occurring at the interface rather than resistive terms which are emphasized in EIS as outlined in the derivation of the CS components by Goes et al.²³ CS is typically used to explore structural characteristics of SAMs (here the immunoassay) and their interaction with the local environment.^{23,24} Like the EIS spectra the CS responses can be represented using complex capacitance. The complex capacitance spectra can be calculated from the impedance spectra with the relationships shown in Equations 1.3 & 1.4:

$$C(\omega) = \frac{1}{j\omega * Z(\omega)} \quad (1.3)$$

$$C(\omega) = \frac{1}{Z''} + j \frac{1}{Z'} = C' + jC'' \quad (1.4)$$

It is important to highlight that the real part of the capacitance spectrum C' is derived from the imaginary impedance Z'' and the imaginary capacitance C'' is derived from the real impedance Z' . C' largely dominates the capacitive response across all frequencies, thus $C(\omega) \approx C'$. While C'' can give insight into the relaxation processes occurring at the electrode-electrolyte interface through measurement of time constants.²³ Often the SAM capacitance at the electrode-electrolyte interface is modeled using a parallel plate capacitor:

$$C_{SAM} = \frac{\epsilon_{SAM}\epsilon_0 A}{d} \quad (1.5)$$

In equation 1.5, ϵ_{SAM} and ϵ_0 correspond to the permittivity of the SAM and of free space respectively, A is the electrode area, and d is the SAM thickness.

However, this work rejects the traditional SAM capacitance model as it does not account for either SAM imperfections or relaxation characteristics in response to an applied electric field as described in detail by Goes (2012).²³ Leveraging CS allows for the monitoring of these two structural characteristics of the SAM and enhances the response due to biomarker binding. As the target biomarkers bind to the immunoassay they mask defects in the SAM due to their physical size and alter dipole relaxation at the interface arising from their inherent charge. These structural changes to both the ion influx and the torque-driven relaxation, contribute to an electrical response resolvable by CS.

When nanoscale SAMs behave as leaky capacitors ions from the electrolyte penetrate the monolayer, manifesting as a non-ideal behavior of the SAM permittivity. The flux of ions into or out of the film is highly dependent on SAM spacing and the applied DC bias. Ionic ingress can contribute significantly to the overall C_{SAM} depending on the applied signal. At certain DC biases below some critical potential, V_C , ionic ingress can contribute significantly to the overall C_{SAM} depending on the applied frequency.

Furthermore, a Debye-type dipolar relaxation is used to describe the construction of the immunoassay and subsequent biomarker detection. SAMs assembled on gold surfaces have inherent dipoles,²⁵ and under an applied field torque-driven orientation changes can be observed as demonstrated in the cartoon below in Figure 1.6:

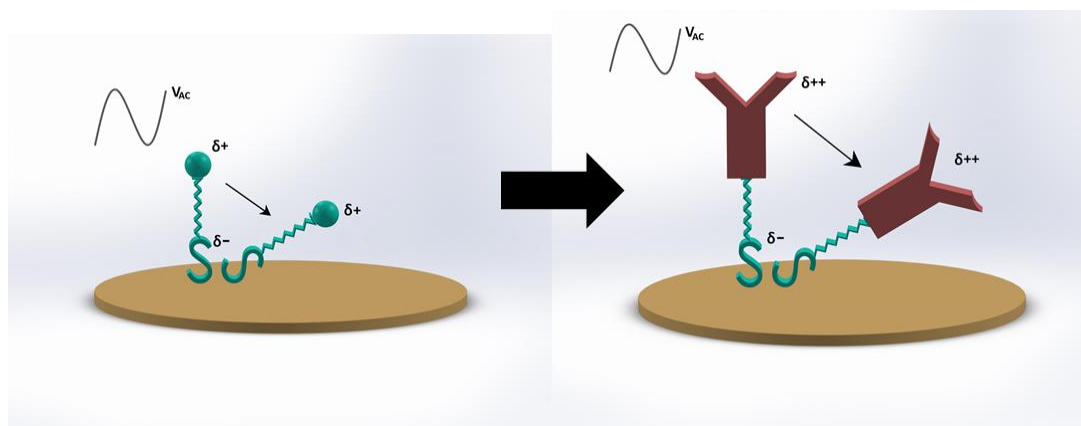
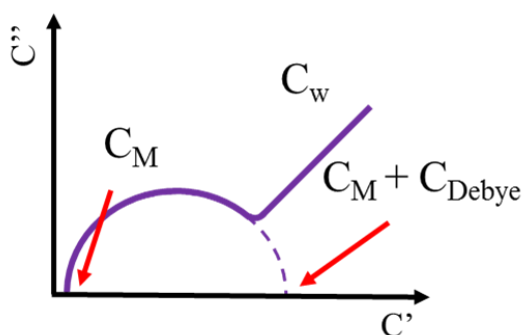


Figure 1.6. Cartoon demonstrating the dielectric relaxation process of a self-assembled immunoassay in response to an applied AC signal.

The dipolar relaxation is dependent on both the polarity and length of the SAM. As the length of the immunoassay is increased (and assuming polarity is held constant), the self-assembled molecules will have a longer lever arm and thus will undergo higher torque-driven orientation changes, decreasing the C' response. However, increasing the length of the dipole will also affect polarity, and in some cases, the SAM may exhibit more than one relaxation as the immunoassay lengthens and more polar molecules are bound to the surface.

The Nyquist capacitive plot measuring the non-faradaic response of a SAM closely resembles the Nyquist impedance plot of a faradaic response in the presence of a redox probe, and the processes here are indicative of analogous phenomena as seen in Figure 1.7. The 45° tail at the low to ultra-low frequency region of the plot (right side) represent the diffusion of ionic species into the SAM. The semicircle diameter points to the capacitance arising from the dipolar relaxation of the monolayer.



Term	Description
C_M	Bulk SAM capacitance
C_{Debye}	Debye dipolar relaxation
C_w	SAM ionic ingress

Figure 1.7. Example Nyquist Capacitance Plot with a description for each term and its representative dominating electrochemical process.

As biomarkers bind to the immunoassay the dipole of the assay changes and thus a change in semicircle diameter is observed as seen in Chapters 4-6. The high frequency region of the plot (left side) measures the bulk capacitance of the monolayer, or the expected capacitance without ionic ingress or dipole relaxation.

1.3 Buffer Complexity

Understanding the buffer's impact on electrochemical measurements is critical when evaluating any biosensor's performance. This is particularly true when evaluating samples of complex matrices. Variations in the bulk of the solution not only impact the solution conductivity but can also have down-stream effects on the electrode-electrolyte interfacial properties. The ionic content of buffer is among the primary factors that influence the biosensor's response. As ionicity decreases the solution resistance increases. Additionally, the ionic content also plays an important role in determining the biosensor's ability in detecting affinity binding events at the electrode surface. With lower ionic content, the Debye length, or the effective length of charge screening effects, increases.⁵ This elongation of the Debye length enhances the signal measured during affinity biosensing as charged molecules bind near the electrode surface. The effects of ionicity will be explored further in Chapter 2.

In addition to ionic content, pH and macromolecule composition also play a crucial role in affinity biosensing. Affinity biosensors commonly rely on biological reagents, such as antibodies or nucleic acid sequences, anchored to the sensor surface to capture their target antigen, and pH can greatly impact the binding interaction between these two.² Sample to sample variations in pH should be considered, and the biosensor's performance should be evaluated across the dynamic range of the pH in a synthetic biofluid before translating to real samples where pH variation may be a concern (See Chapter 6). Furthermore, pH changes can alter the solution resistance, thus electrochemical biosensors should be designed with reducing the overall effect of R_s on the sensor's performance (Chapter 2). Finally, the role of other macromolecules should also be addressed when designing an affinity biosensor. Surface fouling of these macromolecules can increase interfacial capacitive noise while also blocking antibody binding sites.² This work explores buffers ranging from simple human saliva to plant and food extracts to raw meat samples. However, a deep understanding the electrochemical processes was explored in physiological buffers to extract binding characteristics before exploring biosensing in these complex samples.

1.4 Multifunctional Biosensor

This work builds a deeper understanding of the interactions between the buffer, biomarker, and sensor substrate toward electrochemical biosensing. Beginning with optimizing the sensor design toward a more stable and more sensitive biosensor, this platform can detect biomarkers down to the nanogram per milliliter range through either Faradaic or non-Faradaic charge transfer. Leveraging Capacitive Spectroscopy (see section 1.2.6) allows for the isolation of interfacial capacitive phenomena from the bulk beyond traditional impedance-based affinity biosensors. This work demonstrates the detection of very small molecules (ceftiofur and tetrahydrocannabinol) as well as larger macromolecules (Bt-Cry proteins and wheat viruses). The varying size and charges of these molecules directly impact the biosensor's sensitivity,⁵ however by first identifying the key electrochemical drivers this work demonstrates highly sensitive biosensing of each of the targeted biomarkers.

1.5 References

1. Wang, J. Glucose biosensors: 40 Years of advances and challenges. *Electroanalysis* **13**, 983–988 (2001).
2. Frederix, F. *et al.* Enhanced performance of an affinity biosensor interface based on mixed self-assembled monolayers of thiols on gold. *Langmuir* **19**, 4351–4357 (2003).
3. Holzinger, M., Le Goff, A. & Cosnier, S. Nanomaterials for biosensing applications: a review. *Front. Chem.* **2**, 63 (2014).
4. Mehrotra, P. Biosensors and their applications—A review. *J. oral Biol. craniofacial Res.* **6**, 153–159 (2016).
5. Wang, J. Electrochemical biosensors: towards point-of-care cancer diagnostics. *Biosens. Bioelectron.* **21**, 1887–1892 (2006).
6. Gubala, V., Harris, L. F., Ricco, A. J., Tan, M. X. & Williams, D. E. Point of Care Diagnostics: Status and Future. *Anal. Chem.* **84**, 487–515 (2012).
7. Heller, A. & Feldman, B. Electrochemistry in Diabetes Management. *Acc. Chem. Res.* **43**, 963–973 (2010).
8. Jönsson, C. *et al.* Silane-dextran chemistry on lateral flow polymer chips for immunoassays. *Lab Chip* **8**, 1191–1197 (2008).
9. Banaee, H., Ahmed, M. & Loutfi, A. Data mining for wearable sensors in health monitoring systems: a review of recent trends and challenges. *Sensors* **13**, 17472–17500 (2013).
10. McAdams, E. T., Lackermeier, A., McLaughlin, J. A., Macken, D. & Jossinet, J. The linear and non-linear electrical properties of the electrode-electrolyte interface. *Biosens. Bioelectron.* **10**, 67–74 (1995).
11. Zhang, S., Wright, G. & Yang, Y. Materials and techniques for electrochemical biosensor design and construction. *Biosens. Bioelectron.* **15**, 273–282 (2000).
12. Grieshaber, D., MacKenzie, R., Vörös, J. & Reimhult, E. Electrochemical Biosensors - Sensor Principles and Architectures. *Sensors* **8**, (2008).
13. Wilfinger, W. W., Mackey, K. & Chomczynski, P. Effect of pH and Ionic Strength on the Spectrophotometric Assessment of Nucleic Acid Purity. *Biotechniques* **22**, 474–481 (1997).

14. Rocchitta, G. *et al.* Enzyme Biosensors for Biomedical Applications: Strategies for Safeguarding Analytical Performances in Biological Fluids. *Sensors* **16**, (2016).
15. Berggren, C., Bjarnason, B. & Johansson, G. Capacitive Biosensors. *Electroanalysis* **13**, 173–180 (2001).
16. Wang, H. & Pilon, L. Accurate simulations of electric double layer capacitance of ultramicroelectrodes. *J. Phys. Chem. C* **115**, 16711–16719 (2011).
17. Daniels, J. S. & Pourmand, N. Label-free impedance biosensors: Opportunities and challenges. *Electroanalysis* **19**, 1239–1257 (2007).
18. Panneer Selvam, A. & Prasad, S. Companion and Point-of-Care Sensor System for Rapid Multiplexed Detection of a Panel of Infectious Disease Markers. *SLAS Technol. Transl. Life Sci. Innov.* **22**, 338–347 (2017).
19. Lisdat, F. & Schäfer, D. The use of electrochemical impedance spectroscopy for biosensing. *Anal. Bioanal. Chem.* **391**, 1555 (2008).
20. Heinze, J. Cyclic Voltammetry—“Electrochemical Spectroscopy”. New Analytical Methods (25). *Angew. Chemie Int. Ed. English* **23**, 831–847 (2018).
21. Boubour, E. & Lennox, R. B. Stability of ω -functionalized self-assembled monolayers as a function of applied potential. *Langmuir* **16**, 7464–7470 (2000).
22. Park, J.-Y. & Park, S.-M. DNA hybridization sensors based on electrochemical impedance spectroscopy as a detection tool. *Sensors (Basel)*. **9**, 9513–9532 (2009).
23. Góes, M. S., Rahman, H., Ryall, J., Davis, J. J. & Bueno, P. R. A dielectric model of self-assembled monolayer interfaces by capacitive spectroscopy. *Langmuir* **28**, 9689–9699 (2012).
24. Bueno, P. R., Mizzon, G. & Davis, J. J. Capacitance spectroscopy: a versatile approach to resolving the redox density of states and kinetics in redox-active self-assembled monolayers. *J. Phys. Chem. B* **116**, 8822–8829 (2012).
25. Alloway, D. M. *et al.* Interface Dipoles Arising from Self-Assembled Monolayers on Gold: UV–Photoemission Studies of Alkanethiols and Partially Fluorinated Alkanethiols. *J. Phys. Chem. B* **107**, 11690–11699 (2003).

CHAPTER 2

THE ANATOMY OF AN ELECTROCHEMICAL BIOSENSOR*

2.1 Abstract

Point-of-care (POC) testing has revolutionized diagnostic healthcare, bringing medical results directly and immediately to the patient. With faster diagnostics, more immediate clinical management decisions can be made. POC tests most often use a dipstick or swab format to detect the presence of a pathogen, disease, or other relevant biomarker. In these formats, the POC tests eliminate the need for complex lab equipment and trained personnel to collect, process, and analyze sample data for simple diagnostics. However, these tests cannot satisfy all clinical needs because accurate quantitative results are needed. This work templates the process for designing an electrochemical biosensor toward quantitative POC diagnostics focusing on investigating the most important parameters when constructing an electrochemical biosensor through both computational modeling and electrochemical measurements. Furthermore, we demonstrate quantitative affinity biosensing of a model protein toward developing a POC device.

2.2 Design Challenges for Point-of-Care Biosensor Platforms

The key challenge in developing a POC test lies in defining the design parameters of the biosensor toward enabling sensor performance suitable for selectively and specifically quantifying the biomarker of interest. Affinity biosensors function on the principle whereby an immobilized receptor binds a target biomarker, producing a measurable chemical change at a localized surface.¹ This binding event is then transduced to a quantifiable output. For electrochemical biosensors, the measured signal is transduced into either a current or voltage output, which is then amplified and processed using peripheral electronics. The transduction method often influences the biosensor design to enhance performance.¹ This is especially true in the case of electrochemical signal transduction, where the geometry should promote both stability and sensitivity for the biosensor.

* Portions of this chapter have been previously published; see Stevenson, H., Radha Shanmugam, N., Paneer Selvam, A., & Prasad, S. The Anatomy of a Nonfaradaic Electrochemical Biosensor, *SLAS TECHNOLOGY: Translating Life Sciences Innovation* 23(1), pp. 5-15. Copyright © 2017 SAGE Publications.
DOI: 10.1177/2472630317738700

Electrode shape and spacing dictate the distribution of electric charge throughout the electrolyte and at the electrode surface, so a comprehensive understanding of the electrochemical response is vital before selecting the biosensor geometry.²

2.3 Current Affinity Biosensor Design Methodology

Affinity biosensors achieve high selectivity and sensitivity through the immobilization of biological recognition elements on the sensor substrate, usually at the working electrode (WE). Methods for immobilizing recognition elements at the WE include physisorption, cross-linking, covalent bonding, entrapment, and encapsulation. Biomolecules are quick to denature with changes in their surrounding environment,³ thus when designing a biosensor with a long shelf-life it is essential to ensure these biological recognition elements maintain their bioactivity for an extended period.⁴ The orientation of the bio-recognition element at the surface, as well as any conformational changes must be addressed to promote sensor stability & longevity as well as sensitivity & specificity. While this work does not directly address sensor lifetime, future studies to determine optimal storage conditions should be performed.

2.3.1 Biosensor Stability & Longevity

The bio-recognition element immobilization technique can directly impact bioactivity retention.⁴ Direct physisorption is the simplest way of modifying a biosensor's surface, however this often leads to conformational changes and typically results in poor bioactivity longevity.⁴ Chemical adsorption and entrapment, on the other hand, provide an environment favorable for bioactivity retention by stabilizing the bio-recognition element and can reduce applied external forces.^{4,5} This work builds off several previous works⁶⁻⁸ that utilize chemical cross-linking techniques and leverages previously optimized conditions as a starting-point for the immunoassay development.

2.3.2 Biosensor Sensitivity & Specificity

The number of available binding sites for the target biomarker is directly dependent on the surface density of the recognition element and the surface area of the WE. Increasing the number of binding sites increases the likelihood of a target biomarker binding at the WE under optimal conditions, resulting in a lower detection limit. Physisorption often leads to loss of sensitivity due to random orientation of the recognition element and unwanted removal during subsequent washing steps, while chemical cross-linking addresses these concerns by promoting a highly

ordered structure at the interface using self-assembled monolayer architectures.^{4,5} The highly ordered nature of this immobilization technique allows for optimal packing of the recognition element which promotes ultra-sensitive detection.⁴

The immobilization efficiency of the recognition element is heavily dictated by the substrate and electrode material. This work highlights the utilization of gold electrodes to create an amine reactive self-assembled monolayer (SAM) of dithiobis succinimidyl propionate (DSP). The dithiol in the DSP readily chemisorbs to gold surfaces in a highly ordered, dense monolayer. After thiol adsorption, the amine reactive N-hydroxysuccinimide (NHS) esters on the DSP molecule are orthogonal to the electrode surface.^{9,10} The NHS esters are then reacted with a biological recognition molecule to encode selectivity. Various gold-electrochemical biosensors have utilized DSP to cross-link a recognition element to the electrode surface, and detection of bioanalytes leveraging this thiolated cross-linker has been demonstrated in the literature, as summarized in Table 2.1.

Gold is often selected as the WE material, not just to leverage the gold thiol interaction, but also because gold is highly conductive, physically robust, and otherwise chemically inert.¹⁰ Gold possesses an extensive double-layer region that is free of faradaic behavior in most pure electrolytes, making it a highly resistant metal to dissolution and corrosion.¹⁹ Furthermore, gold electrodes can be fabricated using a variety of either thin film or thick-film techniques. Thin-film deposition of gold, for example, physical vapor deposition, is often employed for planar substrates and applications reaching for disposable or reusable biosensors, while thick-film deposition of gold, for example, screen printing, is being explored for continuous monitoring fabric-based or wearable sensors. This work focuses on sensors fabricated using thin-film deposition, namely e-beam deposition, of gold.

Table 2.1. Comparison of Gold-Electrochemical Biosensors Utilizing DSP Cross-Linker.

Target Analyte	Buffer	Redox	Detection Technique	Electrode Type	Detection Limit
Cortisol	saliva		Electrical Resistance	Au thin film on graphene nanoplatelets	2 $\mu\text{g/mL}$ ¹¹
Cortisol	PBS	X	Cyclic voltammetry (CV)	Au PCB	10 pg/mL ¹²
ESAT-6, Mtb CFP	PBS	X	Square Wave Voltammetry (SWV)	Au screen printed on ceramic	7 ng/mL ¹³
Myoglobin	PBS	X	CV, Differential Pulse Voltammetry	Au thin film on glass	9.8 ng/mL ¹⁴
Procalcitonin, Lipoteichoic Acid, Lipopolysaccharide	human whole blood		EIS	Au PCB	0.1 ng/mL , 1 $\mu\text{g/mL}$, 1 $\mu\text{g/mL}$ ¹⁵
Polychlorinated Biphenyls	PBS	X	EIS	Au thin film on glass	0.001 $\mu\text{g/mL}$ ¹⁶
VCAM-1	human urine		EIS	Au PCB	8 fg/mL ⁷
C-reactive Protein, NT-pro-Brain Natriuretic Peptide	PBS		EIS	Au screen printed on silicon wafer	1 ag/mL , 1 fg/mL ⁸
NT-pro-Brain Natriuretic Peptide	PBS & human serum		EIS	Au PCB	10 fg/mL , 500 fg/mL ¹⁷
Ethyl Glucuronide	human sweat	X	SWV, CV, EIS	Au thin film on porous polyimide	1 $\mu\text{g/mL}$ ¹⁸

2.4 Assessing Current Biosensor Geometries

To reduce the noise that is introduced when using a complex matrix, a three-electrode biosensor is often used for independent measurements of the half-cell potential between the WE and reference electrode (RE). Here, a counter electrode (CE) acts as a current source or sink for the faradaic reactions. Introducing the CE encourages a stable RE potential to accurately monitor the WE-RE half-cell for any unexpected changes in the RE surface potential. Previous research has demonstrated the impact of modifying electrode size and positioning for three-electrode systems. Hsieh et al. established the effect of RE geometry and position on the accuracy of impedance measurements.²⁰ They discussed the need to place the RE on a surface such that the electrode does

not significantly perturb the primary currents within the system. Cimenti et al. identify distortions in impedance due to misalignment and relative sizes of the WE and CE in fuel cells.² By controlling the current distribution in the electrolyte, they ensure that the RE effectively separates the overpotential of the WE from the potential drop of the cell. However, little work has been conducted on assessing coplanar electrode geometries.

2.5 Improvements to Affinity Biosensor Design Methodology

Optimization criteria when designing an affinity-based electrochemical biosensor for POC applications has largely been a black box. Biosensor design is often based on rudimentary assumptions about electrode surface area and spacing. Here, a systematic approach to identify relevant design and fabrication parameters for both faradaic and non-faradaic biosensing has been developed. A three-electrode biosensor was chosen to explore both faradaic and non-faradaic charge transfer processes. Optimizing parameters for both faradaic and non-faradaic charge transfer grants more sensor robustness and allows for more customizability in biomarker detection.

This work evaluates the CE positioning with respect to a fixed WE and RE to develop a biosensor platform with coplanar electrodes, and how that positioning impacts the resulting electrochemical response toward the selection of an optimal design of a POC affinity biosensor suitable for detection of biomarkers in complex matrices. The sensor platform consisted of three coplanar electrodes: a WE, RE, and CE deposited onto a flexible PET substrate. The CE positioning was varied with respect to a fixed WE and RE at three distinct distances and three distinct angles, for a total of nine iterations, as shown in Figure 2.1a–c. To identify the final CE placement for optimal POC biosensing, we also considered form factor constraints to reduce the sensing region, and thus the necessary volume of fluid to saturate the sensor. The absolute distances from WE to CE were varied by a fixed amount across the three angles and were numbered from closest CE1 to farthest CE3. Furthermore, the CE positioning angles varied at 135°, 180°, and 225° with respect to the positive x-axis and were denoted CEX.135, CEX.180, and CEX.225, respectively, where ‘X’ here represents the absolute distance from WE to CE. Across these iterations, the stability and sensitivity of the sensor were evaluated through numerical modeling and electrochemical baseline measurements.

2.5.1 Sensor Fabrication

The sensors were fabricated on glass substrates using the e-beam physical vapor deposition. To remove any oils and organic residues, the substrates were rinsed with 70% v/v isopropanol followed by deionized water. The substrates were then dried with pressurized nitrogen air and stored in a nitrogen desiccator until deposition.

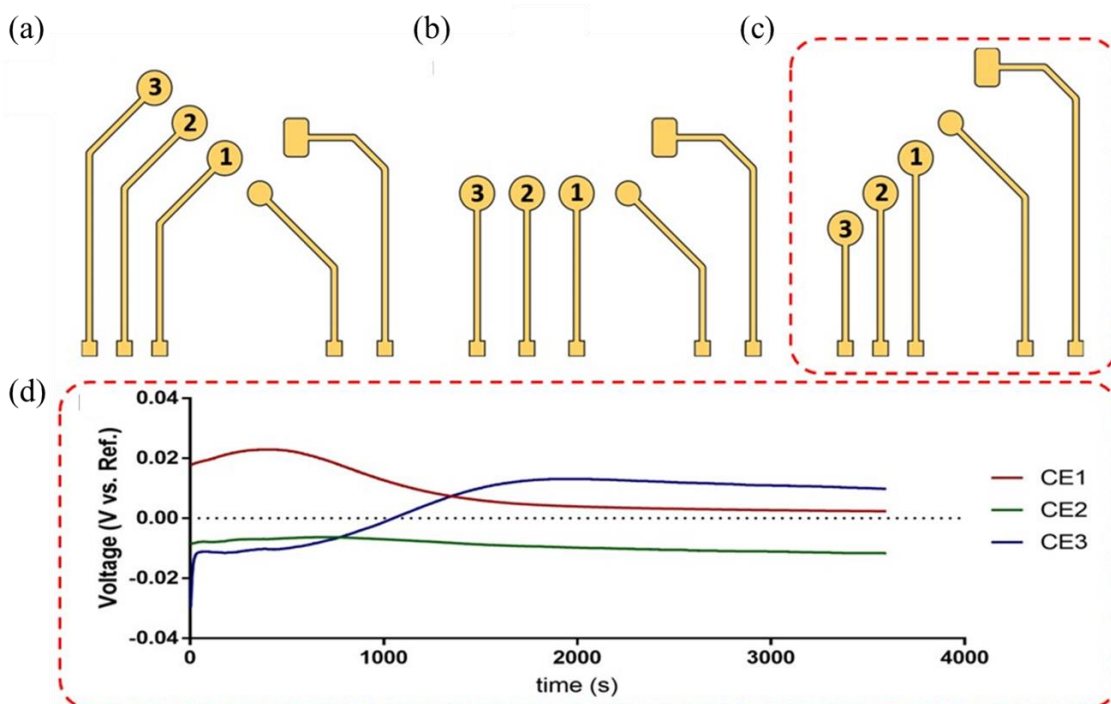


Figure 2.1. Schematic showing each iteration with the CE (a) offset at 135°, (b) 180°, and (c) 225° with respect to the positive x-axis (d) A plot of the OCP vs time for the CEX.225 configurations.

The sensor pattern was achieved using a shadow mask cut using a Spectra-Physics Spirit Laser. The masks were placed flush against the glass substrate, exposing only desired sites for electrode deposition. The electrodes were deposited using electron beam physical vapor deposition at a pressure of $5 * 10^{-6}$ torr. The electrode patterns were deposited with 125 nm Au onto the pre-cleaned glass substrate. The Figure 2.2 insert shows a photograph of the CE1.225 iteration post-fabrication with a dime for scale. A polydimethyl-siloxane (PDMS) confinement well was prepared to restrict the sample fluid in a controlled volume around the site of the three electrodes.

The PDMS wells were cut using a hole-punch to ensure consistent dimensions from sensor to sensor. Furthermore, alignment marks were printed on the reverse side of the sensor to ensure repeatable placement of the confinement wells. Each well allowed a 2 mm tolerance beyond the outermost electrode per each design. Wires were epoxied to the sensor leads using a conductive silver epoxy (volume resistivity $<0.001 \Omega\text{-cm}$) and then interfaced with the potentiostat.

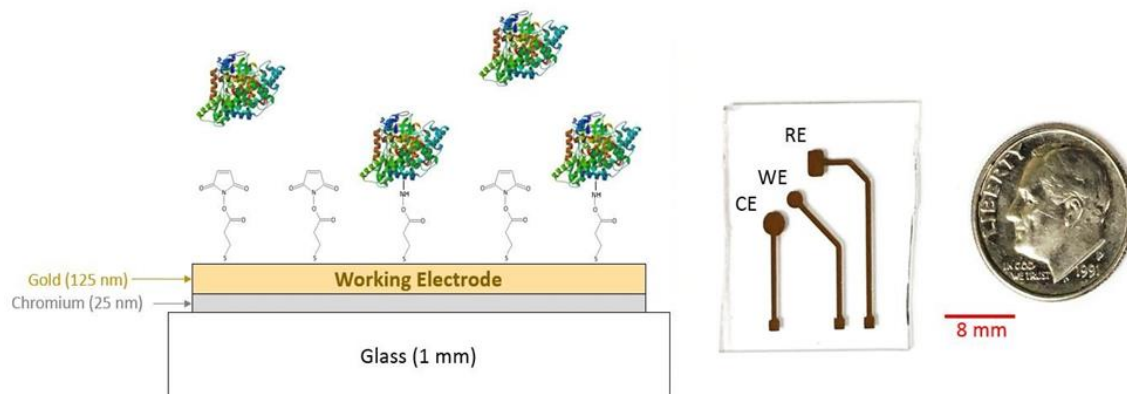


Figure 2.2. Cartoon schematic of the affinity biosensor. A 25 nm chromium adhesion layer was deposited on to the glass substrate, followed by 125 nm of gold. DSP was used to functionalize the WE surface to capture the BSA proteins diluted in 1x PBS. Insert: Photograph depicting the fabricated CE1.225 sensor iteration with dime for size comparison.

2.6 Computational Modeling to Investigate Biosensor Stability

Finite element analysis was employed using COMSOL Multiphysics software to investigate both potential distribution and current density responses across various biosensor iterations to down select the optimal placements of the CE for the coplanar three-electrode biosensor. These computational models provided preliminary data from simulations to evaluate sensor performance across every CE placement iteration. These data were used to aid in the down-selection of the optimal sensor iteration. The simulation was conducted using the primary current distribution module to visualize both the electrolyte potential and the current distributions within the electrolyte.

To construct the geometric model, the biosensor was reduced to a two-dimensional (2D) cross section at the domains of interest: the three electrodes and the surrounding electrolyte. Electrical properties of gold were assigned to each of the three electrodes, while the conductivity of 1x

phosphate buffered saline (1x PBS), $1.8 * 10^{-3} \frac{S}{m}$, was assigned to the electrolyte domain. To visualize the physics of interest, a 10 mV potential was applied to the WE to model the input during EIS experiments. Furthermore, the CE was grounded to act as the current carrying electrode. Electrical insulation was assigned to the RE via a von Neumann boundary condition ($n \cdot J = 0$) to mimic the high-impedance input given by the potentiostat. The electrolyte boundaries were also assigned a von Neumann boundary to confine the electric field within the bounds of the constructed geometric model.

2.6.1 Finite Element Analysis to Select Optimal Counter Electrode Placement

For each iteration of CE placement, both the electrolyte potential and electrolyte current density were analyzed using the primary current distribution module within COMSOL Multiphysics. The electrolyte potential visualizes how the RE surface potential distribution changes when varying the CE positioning, while the current density is used to investigate the variation in charge distribution at the WE. Positioning of the CE should ensure that the applied potential promotes a stable RE potential and uniform current density at the WE.² When modeling primary currents, losses due to solution resistance are considered, while both electrode kinetics and concentration-dependent effects are neglected. Therefore, all charge transfer within the electrolyte is assumed to obey Ohm's law. This model makes the following assumptions: 1) convection within the electrolyte does not significantly affect current density, 2) the electrolyte is homogeneous, and 3) the potential of the electrolyte–electrode interface does not deviate from its equilibrium value. Based on these assumptions, the following equations govern within the system:

$$\text{Electrode: } J_s = -\sigma_s \nabla \phi_s \text{ with } \nabla \cdot J_s = Q_s \quad (2.1)$$

$$\text{Electrolyte: } J_l = -\sigma_l \nabla \phi_l \text{ with } \nabla \cdot J_l = Q_l \quad (2.2)$$

$$\text{Electrode-Electrolyte Interface: } \phi_s - \phi_l = E_{eq} \quad (2.3)$$

In the above equations, J represents the current density vector $\left(\frac{A}{m^2}\right)$ which is dependent on σ , the conductivity $\left(\frac{S}{m}\right)$, and ϕ , the electric potential (V). In these equations, the index s denotes the electrode domains while the l subscript denotes the electrolyte domain. E_{eq} represents the potential

difference at the electrode-electrolyte interface. Figure 2.3a shows a 2D schematic of the geometric model simulated in COMSOL with each domain's applied boundary conditions.

The electrolyte potential is determined through evaluating Equation 2.2 and plotting ϕ_l at each point within the electrolyte. A contour plot of the electrolyte potential can be visualized in Figure 2.3b for the iteration CE1.225. To properly measure half-cell impedance changes between the WE and RE, the RE should lie on a surface with minimal variation in the electrolyte potential.¹⁴ To find the potential distribution at the RE surface, the minimum RE surface potential was subtracted from the maximum RE surface potential. Figure 2.3c demonstrates that by offsetting the CE by 225° with respect to the WE, the potential distribution at the RE surface is reduced. This reduction in potential distribution is likely attributed to isolating the distribution of currents from the RE.

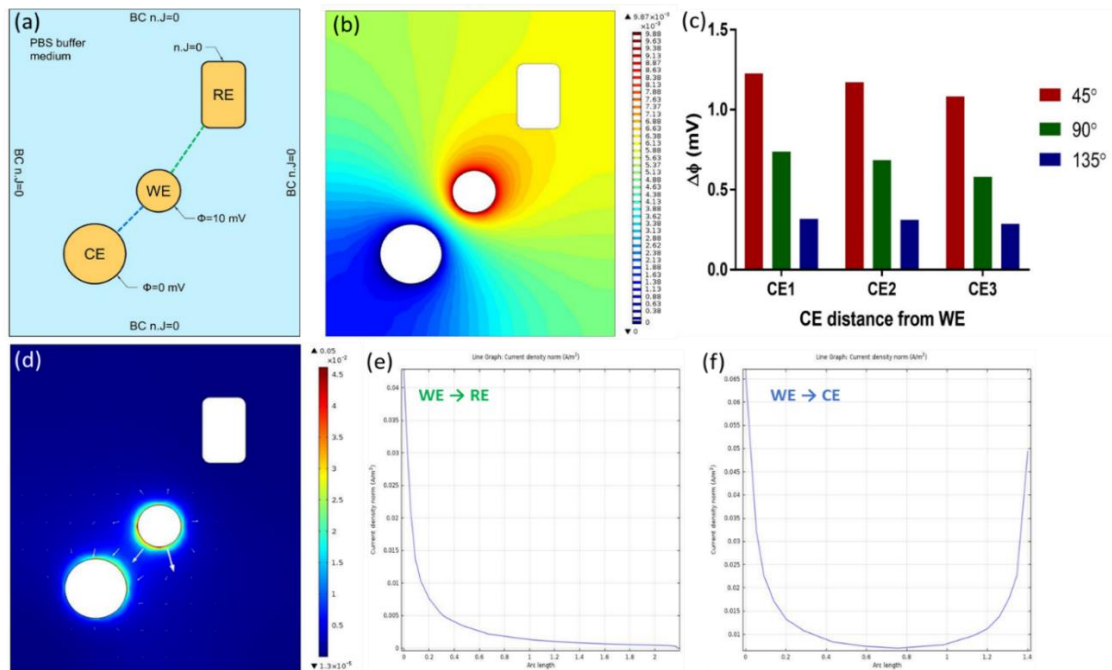


Figure 2.3. (a) Schematic of Finite Element Analysis geometry with applied boundary conditions for the CE1.225 configuration (b) Contour Plot demonstrating isopotential surfaces within the electrolyte (c) Potential Distribution at the RE across all configurations (d) Surface plot showing the distribution of current density and arrow plot representing electric field distribution and direction (e) and (f) Line plots demonstrating the current density distribution along the dashed lines shown in (a). The dashed line color in (a) correspond to the graph insert label color in (e) and (f) indicating the direction.

The simulated current density within the electrolyte, J_l , is also evaluated using Equation 2.2 and is shown in Figure 2.3d. The surface plot indicates the maximal current density is observed at the WE surface implying that the output current response measured in both EIS and CV are from phenomena observed at the WE. The arrow plot in Figure 2.3d indicates the direction of current flow through the electric displacement field. Negligible current flows at the RE, ensuring it maintains a constant potential throughout the experiment. Line plots in Figure 2.3e-f further indicate the current density is concentrated near the WE and CE. Additionally, the current density surface plot shows a maximum, uniform current density at the WE and a near-zero current density at the RE, ensuring the RE is effective at separating the cell potential.

The COMSOL simulations were used to down select which sensor iteration(s) placed the RE on an isopotential surface and produced a large, uniform current density at the WE. Placing the RE in an area with a uniform potential distribution reduces error when reporting the half-cell potential.^{2,13,21} For the CEX.225 iterations, the equipotential surfaces are widely spaced resulting in a smaller distribution of potentials sampled at the RE. The widely spaced equipotential surfaces also indicate a uniform current density at the RE. The small, uniform current density prevents currents from entering the RE and causing a potential drift.

The current density at the WE shows a uniform distribution for every CEX.225 iteration, ensuring the electrode polarization is consistent across the entire electrode surface. Furthermore, the maximum current density occurs at the WE surface. The large WE current density indicates that the output current response measured in EIS are a result of reactions occurring at the WE, and that the measurement of the half-cell potential is between the WE and RE with little to no interference from the CE. These results suggest that placing the CE at 225° with respect to the WE, when compared to the other investigated iterations, will exhibit the best electrochemical properties during biosensing applications. Placing the CE at this angle demonstrate a uniform current density at the WE and RE surfaces. Furthermore, both the potential distribution and current density observed at the RE are minimum, and the current density at the WE is maximum at 225°. Thus, it is expected that placing the CE at 225° with respect to the WE will reduce distortions in measured impedance spectra.

2.7 Electrochemical investigation of biosensor stability

To validate the computational modelling, electrochemical measurements were performed across the nine sensor iterations in Figure 2.1a-c. Sensor stability was explored through both non-faradaic and faradaic characterization.

2.7.1 Open Circuit Potential Evaluation of Sensor Stability

After ~2000 seconds, the OCP values reached a steady-state potential for all sensor iterations Figure 2.1d. Only small variations among the steady-state OCP values existed because the electrodes were neither corroding nor oxidizing throughout the measurement. The corrosion potential of an electrode is dependent on both the metal and the electrolyte.¹⁹ Because both the WE and RE are composed of gold, the corrosion performances of these two electrodes are identical. This results in very small deviations in steady-state values, within 15 mV. The steady-state OCP values were estimated at 2.35 mV for CE1.225, -11.7 mV for CE2.225, and 9.83 mV for CE3.225, as shown in Figure 2.1d. These measurements signify that the electrodes for each iteration are stable in the presence of the PBS buffer.

2.7.2 Faradaic Response Characterized by Cyclic Voltammetry

Cyclic Voltammetry was used to study both sensor stability and faradaic charge transfer kinetics using a ferricyanide redox probe. Cyclic voltammograms were recorded in the presence of 1 mM ferricyanide with a 1x PBS supporting electrolyte. The measurement was repeated for a total of three cycles, to examine the hysteresis of the voltammogram and identify the steady state kinetics of the system. The current response was plotted as a function of applied potential to inform the reversibility of the redox active species at the WE.

Steady-state voltammograms for the 225° configurations are presented in Figure 2.4b. Across sensor iterations, the peak current ratios of cathodic to anodic peak current were consistent, as shown in Table 2.1. A peak current ratio of 1 demonstrates identical diffusion coefficients for the reduced and oxidized forms of the redox probe, and that the charge transfer kinetics are reversible. The CEX.225 iterations all showed peak current ratios very close to 1, implying that the kinetics observed were nearly ideal. Furthermore, a peak separation of 59 mV for a one-electron reaction indicates ideal heterogeneity in charge transfer. Values larger than 59 mV suggest slower charge transfer kinetics, where values less than 59 mV may result from redox molecules bound to the

electrode surface.²² None of the biosensor iterations showed ideal heterogeneity; however, CE1.225 showed the least deviation, with a peak separation value of 75.84 mV. The CE2.225 and CE3.225 iterations had a peak current separation of 89.83 and 81.9 mV, respectively. When translating from buffer solution to biofluids, the faradaic response should be well characterized to prevent nonspecific charge transfer from interfering with the biosensor's performance. The CV results indicated near-ideal reversibility for the CEX.225 sensors while demonstrating sensor stability over the duration of the experiment. Little differences in the faradaic response were observed across the CEX.225 sensors.

It can be seen in Figure 2.4a that the cathodic peak is absent in the first cycle because the ferricyanide molecule must first be reduced to ferrocyanide. In the subsequent two cycles, only minimal differences in the response can be observed, indicating that the system has reached steady state. In CV, the reaction rate, and by extension the current output, is proportional to the WE surface area.¹⁷ Meanwhile, reactions at the CE are less important in determining the current response if the CE conducts current well throughout the experiment.

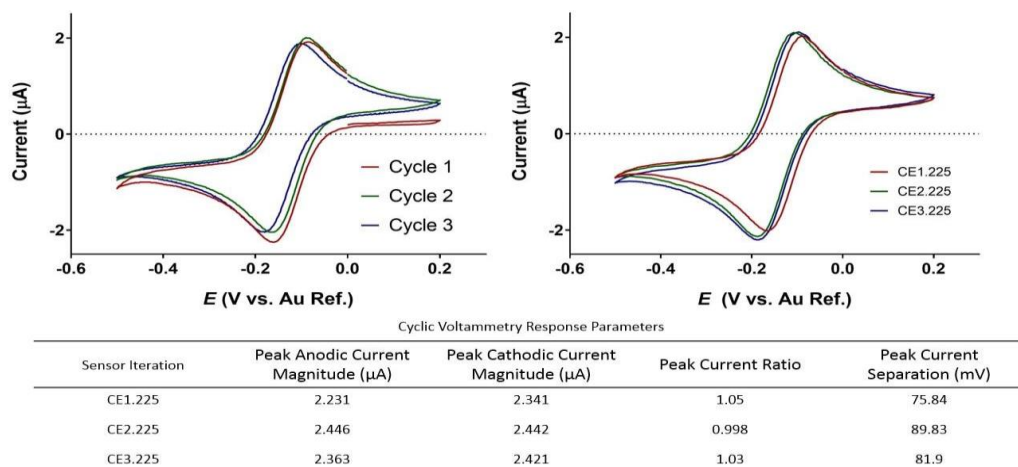


Figure 2.4. Cyclic Voltammogram demonstrating electrode stability in the presence of $K_3[Fe(CN)_6]$ for the CE1.235 configuration (a) across 3 cycles for the CE1.225 iteration and (b) across the CEX.225 iterations. (c) Table 2.1 summarizing faradaic response indicating reversibility of the system.

2.7.3 Faradaic Electrochemical Impedance Spectroscopy

Whether leveraging faradaic or non-faradaic charge transfer, the biosensor design should promote a uniform current distribution to prevent distortions in the impedance spectra.^{2,23} Thus, positioning of the CE should be carefully chosen to maintain a stable potential at both the WE and RE throughout the experiment. Faradaic EIS was employed across the sensor iterations in the presence of a ferricyanide redox probe.

The data here were fitted to a Randle's cell to correlate changes in circuit parameters across sensor iterations. As the angle between the WE and CE increases, the solution resistance (R_s) within the system decreases, with the lowest values at the CEX.225 iterations (Figure 2.6b). The solution resistance should be low enough that it does not contribute significantly to the overall impedance; therefore, the CEX.225 show the most favorable R_s values. No observable changes in either double-layer capacitive or charge transfer resistance were noted across sensor iterations.

2.7.4 Down-Selection of the Final Biosensor Design

To make a down-selection of the optimal design for the biosensor, the form factor of the biosensor analogue must also be taken into consideration. By placing the CE closer to the WE and RE, the sensing region is also reduced. This shrinking of the sensing region allows for a smaller fluid volume necessary to saturate the sensor. Because the CEX.225 iterations showed no significant differences in their electrical performance, CE1.225 was chosen as the optimal design tested based on both electrical performance and form factor.

2.8 Electrochemical Investigation of Biosensor Sensitivity

To determine the biosensor sensitivity, a sinusoidal voltage of 10 mV root mean square was applied across a frequency range of 1 Hz to 1 MHz. The resulting current response of the system was measured, and the complex impedance was calculated by taking the ratio of input voltage to measured current. EIS was used to study baseline characteristics across sensor iterations in a blank PBS buffer.

Bovine serum albumin (BSA), a protein with a molecular weight of 66.5 kDa and well understood electrochemical properties,²⁴ was selected as a model protein to determine the non-faradaic response due to affinity binding. Non-faradaic EIS was carried out on the down-selected sensor

iteration CE1.225. The binding of BSA to a DSP monolayer was used to monitor capacitive changes and extrapolate about subsequent affinity binding sensor performance. These experiments served to deconstruct the role of each of the components (electrode, cross-linker, and biomarker) of the affinity biosensor. The BSA was diluted in 1x PBS, a commonly used isotonic buffer. PBS is devoid of any redox active species; thus, detection is achieved through measuring interfacial capacitive changes due to binding.

Before biosensing in complex biofluids, detecting a model protein first in PBS gave a neater picture of the response mechanism before introducing output variability arising from the complex matrix. At select input frequencies, the system's capacitance dominates over the resistive effects, which indicate non-faradaic processes.²¹ The non-faradaic response was leveraged for capacitive effects due to BSA binding at the electrode surface to glean insight on the biosensor's ability to distinguish low concentrations of a model protein in a highly controlled, well understood matrix.

The sensor leveraged changes in non-faradaic charging of the double layer because BSA binding events do not produce a measurable change in charge transfer resistance in this setup. The impedance response is represented as Bode and Nyquist plots in Figure 2.5a and 2.5c, respectively. The Nyquist plot displays an incomplete semicircle and the absence of a charge transfer resistance, which both indicate a non-faradaic response. The frequency 100 Hz was chosen to identify changes in impedance for the calibrated dose–response plot in Figure 2.5a at 100 Hz; the phase angle is between -84.87° and -83.31° , indicating that the response is driven by the capacitance at the interface. Therefore, the changes in impedance can be attributed to capacitive binding within the EDL. Increasing concentrations of BSA show a decreasing trend in impedance at 100 Hz. As more BSA binds at the surface, charge is stored within the double layer, altering the system's capacitance. This increase in double-layer capacitance yields a decrease in overall impedance over a wide range of BSA concentrations. The impedance continues to decrease with increased BSA concentrations until saturation at 100 ng/mL. This saturation point corresponds to the maximal concentration of BSA to bind to DSP and produce a quantifiable change in impedance.

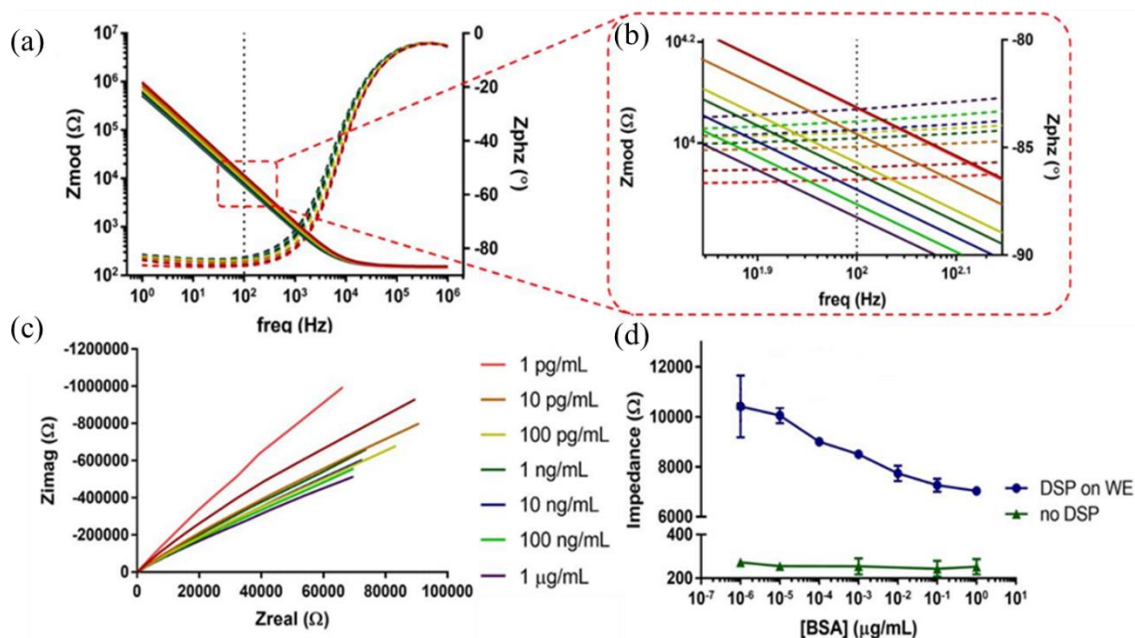


Figure 2.5. EIS data presented from the CE1.225 iteration. (a) Bode Plot of BSA dose-response with (b) Zoomed in view of around 100 Hz. Corresponding (c) Nyquist Plot for BSA dose-response. (d) Impedance values at 100 Hz for BSA calibrated dose response with DSP functionalization and no DSP surface functionalization.

In the Bode plot from Figure 2.5a, at frequencies of 1,000 Hz and below, the impedance response is driven by the capacitive reactance, indicating non-faradaic charging of the double layer. With increasing concentrations of BSA, increases in constant phase element values were observed (Figure 2.6a). This correlates to larger capacitance values, and thus a decrease in impedance at frequencies where capacitive effects are dominant. Furthermore, the solution resistance does not change across BSA concentrations, supporting the conclusion that changes in the impedance are due to binding events at the electrode surface. The BSA dose-response was repeated without functionalizing any electrodes to validate that capacitive changes were due to surface binding rather than from physisorption of BSA onto the electrode surfaces. A one-way ANOVA determined that no variation in impedance exists across BSA concentrations ($p = 0.8096$) at 100 Hz for the bare electrodes. This demonstrates that physisorption can be neglected at the selected concentrations, as it does not significantly contribute to the signal response.

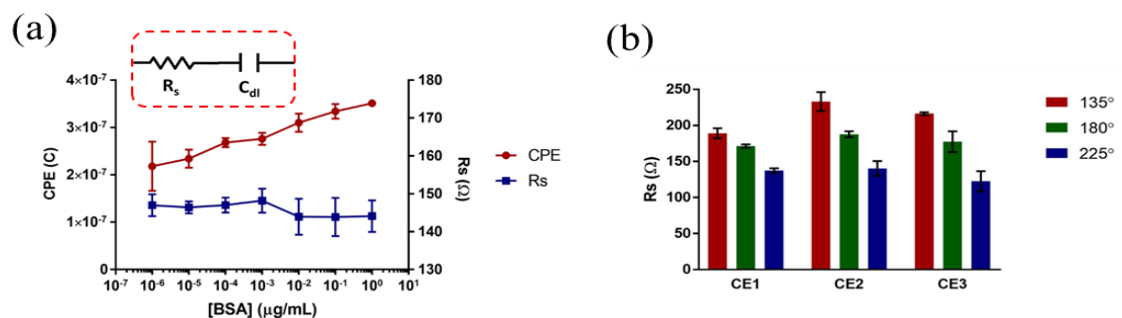


Figure 2.6. (a) Plots of fitted solution resistance and double layer capacitance (CPE) across BSA concentrations ($n=3$) *insert*: Modified Randle's Equivalent circuit used to fit experimental data across BSA doses (c) Plots of fitted solution resistance (R_s) values for each sensor iterations ($n=3$).

When fitting the BSA dose-response data to Randle's circuit, the charge transfer resistance is omitted (Figure 2.6a insert) because no faradaic charge transfer is observed without the ferricyanide redox probe. Additionally, Figure 2.6b indicates that the solution resistance decreases as the angle is varied between the WE and CE. When fixing the angle and looking across distances, no trend in solution resistance is apparent. This indicates that the solution resistance is primarily driven by the angular displacement and not absolute distance.

2.9 Effect of Buffer Ionicity and Applied DC Biases

2.9.1 Impact of buffer ionicity on non-Faradaic biosensing

To explore the how buffer conductivity impacts the bulk resistive and capacitive responses, EIS measurements with no DC bias ($n=2$) were taken for a series of PBS dilutions on both bare gold electrodes and DSP modified electrodes. A baseline measurement for each PBS dilution (0.1x, 0.25x, 0.5x, & 1x) was taken on each sensor, then the sensor was washed with DI water and dried with N_2 before incubating a 10 mM DSP in dimethyl sulfoxide (DMSO) solution for 60 minutes (DSP incubation conditions were previously optimized).⁷ After incubation, 2x DMSO washes and 1x DI water wash was performed to prepare the sensor for subsequent measurements in each of the PBS dilutions.

Bode Plots for each dilution were plotted in Figure 2.7a and 2.7b for the bare gold sensor and the DSP modified sensor respectively. The high frequency region of the graph, 10,000 Hz and greater, exhibits a phase angle (Z_ϕ) approaching zero. This indicates that the response driven by resistive

components of the system. Additionally, a relatively flat impedance modulus (Z^*) is observed which corresponds to the bulk solution resistance. As the PBS concentration increased from 0.1x to 1x, this solution resistance (R_s) decreased as shown in Figure 2.7c. A high R_s value can lead to resistive effects dominating the sensor response, masking the interfacial capacitive properties. As the ionic content of the buffer increases the Z_ϕ is shifted right as resistive effects dominate the response across the input frequency range. The change in R_s on the bare electrodes is much more pronounced than the DSP modified sensor because the DSP monolayer acts as an ultra-thin coating reducing the bulk-effects on the sensor performance.²⁵ Extrapolating to immune-sensing, this coating helps prevent dramatic R_s shifts across samples, and helps stabilize the low-frequency capacitive response.

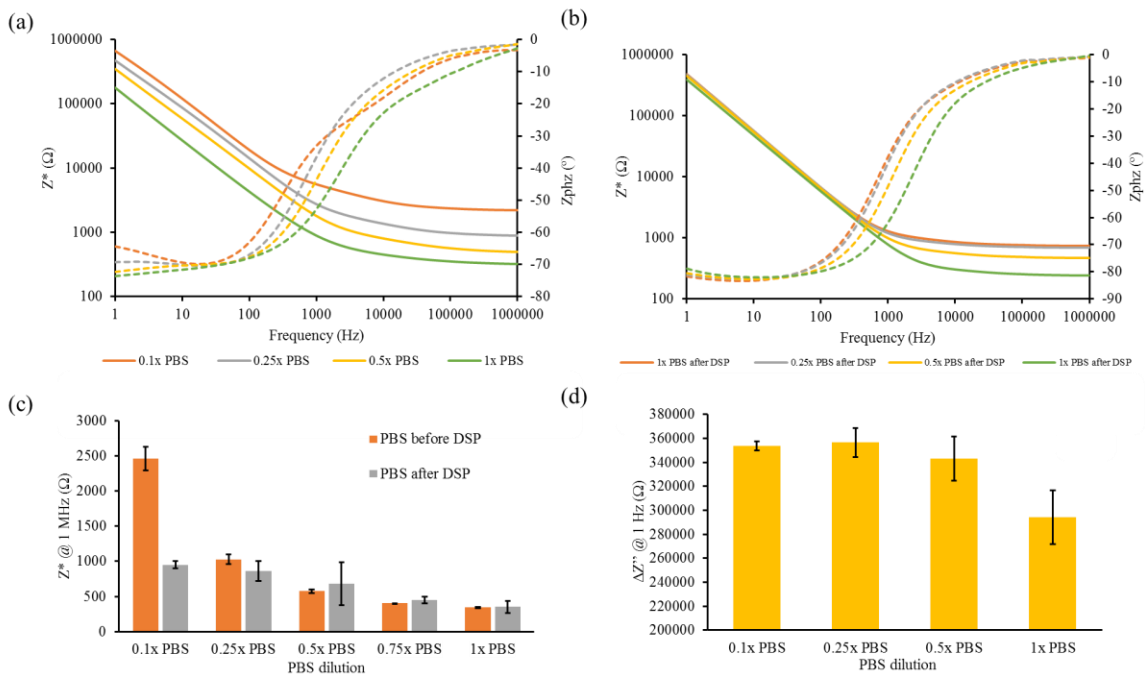


Figure 2.7. Bode Modulus and Phase plots for PBS dilutions between 0.1x and 1x for both (a) an unmodified sensor and (b) a DSP functionalized sensor, (c) Z^* values at 1 MHz across PBS dilutions for both unmodified and DSP functionalized sensors, (d) change in imaginary impedance at 1 Hz between unmodified and DSP functionalized sensors.

Additionally, the ultra-low frequency (1 Hz to ~5 Hz) Z_ϕ response was more resistive for low ionicity (-63° for 0.1x PBS) then shifts down for the bare sensor with increasing PBS concentration (-74° for 1x PBS). The resistivity in the lower ionic solutions is due to hydrolysis and current

leakage across the electrode-electrolyte interface to maintain a constant potential between the WE and RE,²⁶ suggesting that a higher ionicity is desirable for biosensing. However, the Z_{ϕ} response ~ 30 Hz and below for the DSP modified sensor showed no significant deviations across PBS concentration. This is due to the insulative nature of the tightly packed DSP monolayer which prevents charges from leaking across the interface.

To compare how well the DSP monolayer prevented current leakage across PBS dilutions, the imaginary impedance (Z'') of the bare electrode was subtracted from the Z'' of the DSP measurement at 1 Hz (Figure 2.7d). Similar responses were reported for low concentrations of PBS. However, as the ionicity increases, charge screening effects dominate the capacitive response. While this seems to indicate that affinity biosensors should always operate under lower ionic conditions to reduce charge screening effects and increase the Debye length, it is not always possible to control the ionicity of the buffer (as is the case in biosensing in human biofluids).²⁷ Charge screening, due to higher ionic content in the buffer, must be accounted for when developing an electrochemical biosensor. And understanding the buffer's effects on the biosensor's response is crucial when developing a proof-of-concept biosensor when the sample-to-sample variability cannot be fully controlled. This sensor has been designed in a way where small deviations (>10 -fold change) in ionic content will not significantly impact the sensor response. However, when a biofluid can vary significantly across samples, the ionicity must also be addressed.

2.9.2 Applied DC Bias effect on SAM penetration

To leverage the ionic ingress/egress into SAMs for future biosensing applications, the effect of an altering the DC bias was also explored. SAMs behave like ideal capacitors above some critical potential V_c . However, when the V_c threshold is surpassed, the ion penetration into the SAM is activated.²⁸ The operational range of the sensor for non-faradaic biosensing should lie within the electrochemical window. To determine the electrochemical window for the sensor-electrolyte (1x PBS) combination, first a CV scan at 100 mV/s between -0.5 V and 0.5 vs Ref. was performed. The voltammogram in Figure 2.8a demonstrates a relatively stable response for input voltages at -0.3 V and above. Below -0.3 V oxidation of the gold and/or hydrolysis begins taking place, increasing the current exponentially.²⁹ EIS measurements were then taken in a 1x PBS electrolyte with DC biases sequentially applied from $V_{DC} = 0.2$ V to -0.3 V in 0.1 V intervals to determine

the phase response was on a bare sensor and a sensor modified with DSP. Bode Phase plots for both before and after monolayer adsorption are shown in Figure 2.8b for $V_{DC} = 0.2 V$, $V_{DC} = 0 V$, & $V_{DC} = -0.3 V$.

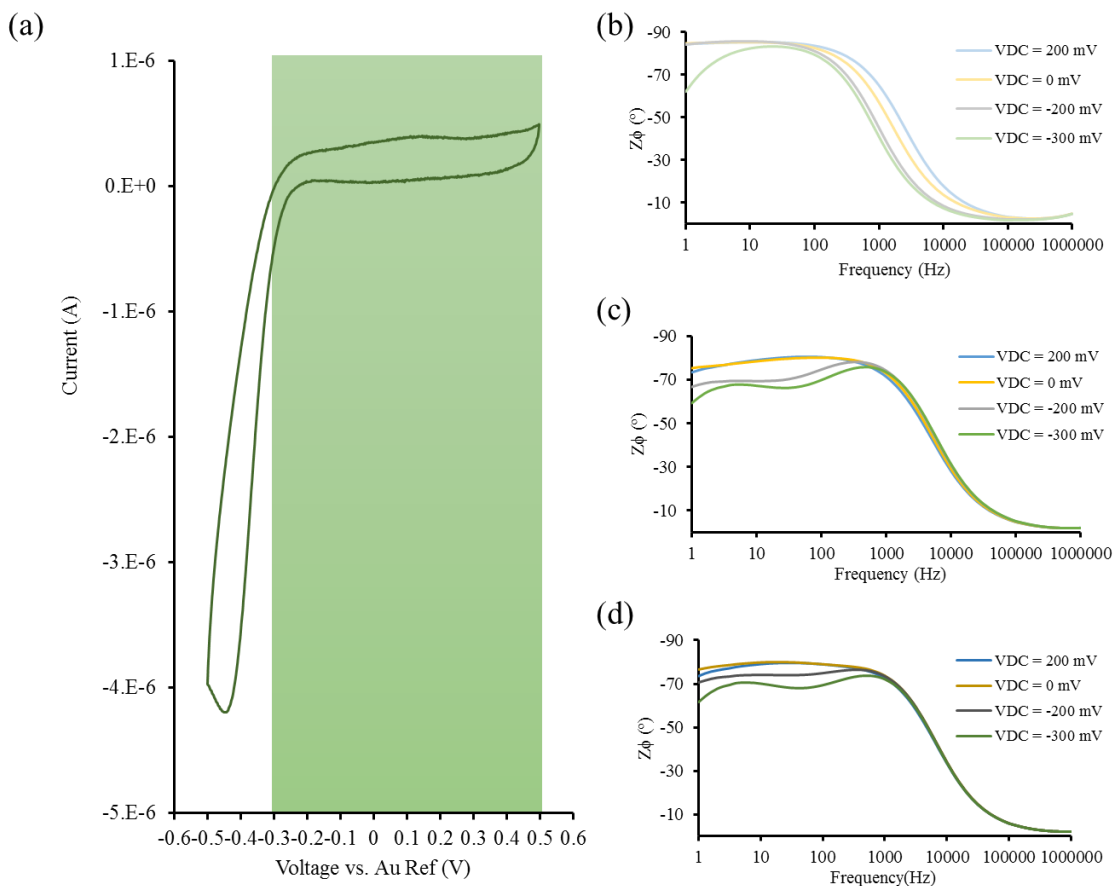


Figure 2.8. (a) Cyclic Voltammogram in the presence of 1x PBS. EIS measurements in the presence of 1x PBS at $V_{DC} = 0.2 V$, $V_{DC} = 0 V$, & $V_{DC} = -0.3 V$ for (b) an unmodified sensor (c) a DSP functionalized sensor, and (d) a DSP functionalized sensor after introducing 10 ng/mL BSA.

For a $V_{DC} = -0.3 V$ the low frequency response for an unmodified sensor suggests that hydrolysis is occurring as the $Z_{\phi} \approx -60$ at 1 Hz. As DSP and the BSA bind to the surface this ultra-low frequency behavior is still observed, however another phase shift across between 10 & 1000 Hz is observed across the various input DC potentials. This phase shift occurs for $V_{DC} < -0.2 V$ due to the ionic ingress and enhanced Debye relaxation. These effects are more pronounced for the measurements after DSP functionalization than after BSA incubation. When BSA binds to the DSP

monolayer, it reduces the SAM permittivity to ions due to the protein's sheer size relative to the DSP spacing.^{9,30}

2.10 Conclusion

In this work, criteria for optimizing the design of a coplanar, three-electrode biosensor are summarized. These results identified the impact of altering CE positioning on sensor performance for an affinity biosensor analogue. The biosensor was optimized through simulated models followed by subsequent experimental validation. First, COMSOL analysis identified the sensor design from the perspective of placement of the RE. Based on the COMSOL analysis it can be concluded that the RE needs to be placed on an isopotential surface and the maximum current density should be obtained at the WE. OCP measurements demonstrate the thermodynamic stability of the system, while CV was used to determine stability in the presence of faradaic charge transfer. The sensitivity was evaluated by measuring impedance changes with EIS. This biosensor analogue will serve as a model for further development as a POC affinity biosensor in subsequent sections of this work.

Sensor performance in complex matrices often suffers due to sample to sample variability; unwanted faradaic currents commonly arise due to dissolved redox active species. These currents can pose a challenge when decoupling the non-faradaic response if the passage of interfacial currents influences the sensor stability. The biosensor platform developed in this work demonstrated a stable electrode-electrolyte interaction in both the presence and absence of faradaic currents. Furthermore, the biosensor was highly sensitive to non-faradaic capacitive binding events against a model protein, making this an attractive solution for a rapid POC platform.

Optimizing the design first ensures a more stable and sensitive sensor output. The sensor leveraged the gold-thiol interaction to functionalize the biosensor through self-assembly of a DSP monolayer. The DSP then served as a non-specific capture probe to detect the model protein BSA. While DSP will react with primary amines on nearly all proteins, the selectivity of an affinity biosensor can be tuned to detect other analytes of interest by first reacting DSP with a selective capture probe as seen in each of the later chapters. The optimized biosensor design has potential for detecting biomarkers in complex matrices like saliva and plant or food extracts. The design of the biosensor

is the first aspect toward rapid detection, so understanding the recipe for designing a coplanar three-electrode biosensor will help drive the development of next generation POC diagnostics.

2.11 Author Contributions

H.S., N.R.S., A.P.S., and S.P. conceived the project framework. H.S. performed the modeling and experiments. H.S., N.R.S., A.P.S., and S.P. analyzed and interpreted the data. H.S., N.R.S., and S.P. wrote the paper.

2.12 Declaration of Conflicting Interests

The authors declared no potential conflicts of interest with respect to the research, authorship, and/or publication of this article.

2.13 Funding

The authors received no financial support for the research, authorship, and/or publication of this article.

2.14 References

1. Wang, J. Electrochemical biosensors: towards point-of-care cancer diagnostics. *Biosens. Bioelectron.* **21**, 1887–1892 (2006).
2. Cimenti, M., Birss, V. I. & Hill, J. M. Distortions in Electrochemical Impedance Spectroscopy Measurements Using 3-Electrode Methods in SOFC. II. Effect of Electrode Activity and Relaxation Times. *Fuel Cells* **7**, 377–391 (2007).
3. Cosnier, S. Biomolecule immobilization on electrode surfaces by entrapment or attachment to electrochemically polymerized films. A review. *Biosens. Bioelectron.* **14**, 443–456 (1999).
4. Matharu, Z., Bandodkar, A. J., Gupta, V. & Malhotra, B. D. Fundamentals and application of ordered molecular assemblies to affinity biosensing. *Chem. Soc. Rev.* **41**, 1363–1402 (2012).
5. Pei, R., Cheng, Z., Wang, E. & Yang, X. Amplification of antigen–antibody interactions based on biotin labeled protein–streptavidin network complex using impedance spectroscopy. *Biosens. Bioelectron.* **16**, 355–361 (2001).
6. Munje, R. D., Muthukumar, S., Jagannath, B. & Prasad, S. A new paradigm in sweat based wearable diagnostics biosensors using Room Temperature Ionic Liquids (RTILs). *Sci. Rep.* **7**, 1950 (2017).
7. Selvam, A. P. *et al.* Development and validation of an impedance biosensor for point-of-care detection of vascular cell adhesion molecule-1 toward lupus diagnostics. *Futur. Sci. OA* **3**, FSO224 (2017).
8. Prasad, S., Selvam, A. P., Reddy, R. K. & Love, A. Silicon nanosensor for diagnosis of cardiovascular proteomic markers. *J. Lab. Autom.* **18**, 143–151 (2013).
9. Rudzinski, W. E. & Francis, K. Evaluating the surface density and heterogeneity of a dithiobis (succinimidylpropionate) self-assembled monolayer on gold and its coupling with DNA embedded within a matrix. *Appl. Surf. Sci.* **256**, 5399–5405 (2010).
10. Bendavid, A., Martin, P. J. & Wieczorek, L. Morphology and optical properties of gold thin films prepared by filtered arc deposition. *Thin Solid Films* **354**, 169–175 (1999).
11. Khan, M. S. *et al.* Based Analytical Biosensor Chip Designed from Graphene-Nanoplatelet-Amphiphilic-diblock-co-Polymer Composite for Cortisol Detection in Human Saliva. *Anal. Chem.* **89**, 2107–2115 (2017).
12. Kaushik, A. *et al.* Electrochemical sensing method for point-of-care cortisol detection in human immunodeficiency virus-infected patients. *Int. J. Nanomedicine* **10**, 677 (2015).
13. Diouani, M. F. *et al.* Detection of ESAT-6 by a label free miniature immuno-electrochemical biosensor as a diagnostic tool for tuberculosis. *Mater. Sci. Eng. C* **74**, 465–470 (2017).

14. Lee, H. Y., Choi, J. S., Guruprasath, P., Lee, B.-H. & Cho, Y. W. An electrochemical biosensor based on a myoglobin-specific binding peptide for early diagnosis of acute myocardial infarction. *Anal. Sci.* **31**, 699–704 (2015).
15. Panneer Selvam, A. & Prasad, S. Companion and Point-of-Care Sensor System for Rapid Multiplexed Detection of a Panel of Infectious Disease Markers. *SLAS Technol. Transl. Life Sci. Innov.* **22**, 338–347 (2017).
16. Date, Y. *et al.* Label-free impedimetric immunoassay for trace levels of polychlorinated biphenyls in insulating oil. *Anal. Chem.* **86**, 2989–2996 (2014).
17. Panneer Selvam, A. & Prasad, S. Nanosensor electrical immunoassay for quantitative detection of NT-pro brain natriuretic peptide. *Future Cardiol.* **9**, 137–147 (2013).
18. Kinnamon, D., Selvam, A. P., Prasad, S. & Muthukumar, S. Electronic bracelet for monitoring of alcohol lifestyle. in *SENSORS, 2016 IEEE* 1–3 (IEEE, 2016).
19. Burke, L. D. & Nugent, P. F. The electrochemistry of gold: I the redox behaviour of the metal in aqueous media. *Gold Bull.* **30**, 43–53 (1997).
20. Hsieh, G., Mason, T. O., Garboczi, E. J. & Pederson, L. R. Experimental limitations in impedance spectroscopy: Part III. Effect of reference electrode geometry/position. *Solid State Ionics* **96**, 153–172 (1997).
21. Daniels, J. S. & Pourmand, N. Label-free impedance biosensors: Opportunities and challenges. *Electroanalysis* **19**, 1239–1257 (2007).
22. Nicholson, R. S. Theory and application of cyclic voltammetry for measurement of electrode reaction kinetics. *Anal. Chem.* **37**, 1351–1355 (1965).
23. Winkler, J. *et al.* Measurement of single electrode potentials and impedances in hydrogen and direct methanol PEM fuel cells. *Electrochim. Acta* **391**, 1931–1939 (2016).
24. Salgin, S., Salgin, U. & Bahadir, S. Zeta potentials and isoelectric points of biomolecules: the effects of ion types and ionic strengths. *Int. J. Electrochem. Sci* **7**, 12404–12414 (2012).
25. Góes, M. S., Rahman, H., Ryall, J., Davis, J. J. & Bueno, P. R. A dielectric model of self-assembled monolayer interfaces by capacitive spectroscopy. *Langmuir* **28**, 9689–9699 (2012).
26. Kelly, R. G., Scully, J. R., Shoesmith, D. & Buchheit, R. G. in *Electrochemical techniques in corrosion science and engineering* 266–370 (CRC Press, 2002).
27. Lee, J. A. *et al.* An electrochemical impedance biosensor with aptamer-modified pyrolyzed carbon electrode for label-free protein detection. *Sensors Actuators B Chem.* **129**, 372–379 (2008).
28. Boubour, E. & Lennox, R. B. Stability of ω -functionalized self-assembled monolayers as a function of applied potential. *Langmuir* **16**, 7464–7470 (2000).

29. Ogura, K., Haruyama, S. & Nagasaki, K. The electrochemical oxidation and reduction of gold. *J. Electrochem. Soc.* **118**, 531–535 (1971).
30. Vericat, C., Vela, M. E., Benitez, G., Carro, P. & Salvarezza, R. C. Self-assembled monolayers of thiols and dithiols on gold: new challenges for a well-known system. *Chem. Soc. Rev.* **39**, 1805–1834 (2010).

CHAPTER 3

GMO BIOSENSOR

3.1 Abstract

Since their introduction in 1994, genetically modified organisms (GMOs) have remained a hot topic in American and international politics for their use in food products. Despite the scientific consensus that GMO foods pose no greater risk to human health over conventional food, public concerns continue to rise regarding the safety, regulation, labelling, and environmental impact of GMO foods. Here we have developed a handheld biosensor capable of detecting the presence of two commonly found GMO proteins, Bt-Cry1Ab and Bt-Cry1F, in both corn flour and wheat leaf extract. The sensor relies on measuring faradaic charge transfer to determine the concentration of GMOs present in the food sample and can detect proteins down to the nanogram per mL range. Accompanying the sensor are portable electronics that allow for easy handheld detection serving as a prototype toward a consumer-end product that could reliably detect proteins in raw and processed foods for customers wanting more control over the foods they consume.

3.2 Introduction

The advent of plant genetic engineering technology has ushered in the promise of the next agricultural green revolution with significant impacts on human nutrition, animal feed, biofuels and various plant derived products. Genetically modified (GM) crops express novel traits such as herbicide tolerance, disease/pest resistance, ability to cope with abiotic stress, enhanced shelf life etc.¹ Using *Agrobacterium tumefaciens*-mediated or other plant transformation methods, these novel traits are engineered through the insertion of new genes into the plant genome or the altered expression of existing plant genes. The plant transformation process often involves introduction of genes for antibiotic resistance, in parallel, for the selection of transgenic plants.² GM crop products may contain novel carbohydrates, lipids, primary/secondary metabolites or a range of other substances, in addition to the recombinant DNA, RNA and proteins.^{2,3}

The commercial cultivation of GM plants is on the rise since the 1990s and recent ISAAA (International Service for the Acquisition of Agri-biotech Applications) reports estimate value of

global GM crops to be more than US \$18 billion.^{3,4} GM crops are cultivated in about 25 countries in an area covering over more than 189 million hectares.⁴ The US leads the way in commercial GM crop cultivation with soybeans, maize, cotton, canola, papaya, alfalfa, apples, potatoes, squash and sugar beets being the major crops planted.^{1,4} In US and many other countries, laws have been passed that require regulatory approval before commercial cultivation as well as mandating labeling GM food and GM-derived products. These laws have been put in place to address potential questions related to safety to human health, animals and the environment from of engineered molecules found in GM products. Analytical laboratory tools currently used to identify GM plant material detect and quantify transgene DNA, the recombinant proteins they encode or the novel engineered metabolites. Such tools can also serve as a valuable resource for plant genetic engineering scientists engaged in plant transformation, selection of transgenic plants and quality control of commercially cultivated GM crops. An easy-to-use device can also benefit consumers to make informed choices regarding the consumption of GM products.

The most widely used tool for the identification of GM plant material involves identification of transgene DNA sequences by polymerase chain reaction (PCR).⁵ Specific DNA regions of the transgene such as the gene promoter, coding sequences, terminator or T-DNA regions are amplified and detected by either end-point PCR or quantitative real-time PCR. Although technically demanding, PCR is a highly sensitive laboratory tool frequently employed in the various stages of the plant genetic engineering process for selecting transformed plants for large-scale propagation. The ability to isolate adequate amounts of DNA with sufficient integrity & quality is crucial for successful analysis of GM plant material by PCR. While freshly harvested plant tissue is an ideal starting material for PCR-based detection methods, processed samples that have been subjected to heating, chemical/mechanical treatments or ageing may yield inconsistent results due to low recovery of amplifiable DNA.

Recombinant proteins produced by transgenic plant material such as the *Bacillus thuringiensis* crystal proteins can be more stable as compared to DNA in their ability to survive chemical, mechanical and thermal treatments during food processing.⁶ Hence, proteins can potentially serve as more reliable molecules to identify GMO samples than transgene nucleotide sequences. While several commercial enzyme-linked immunoassay (ELISA) kits are available for GMO protein

detection, this laboratory technique requires technical expertise, time and resources.⁷ The sensitivity of ELISA may become a limiting factor when analyzing samples with low amounts of GM content. Advanced analytical tools such as HPLC, gas chromatography, mass spectrometry or NMR can detect and quantify engineered metabolites from GM products, but these are beyond the reach of consumers and several laboratories.

Biosensor technology that is currently widely used in the health-care sector offers an attractive alternative that can potentially be used by scientists, regulatory bodies and consumers for the detection of GM plant material. Biosensors incorporate specific biological recognition elements that target an analyte directly as a ligand or chemically modify the analyte leading to the transmission of an optical, electrochemical, piezoelectric, calorimetric or another kind of signal the intensity of which is proportional to the concentration of analyte present in the sample being analyzed.⁸ Various types of biosensors have been reported that detect GM plant material-specific transgene DNA sequences utilizing complementary nucleic acid sequences as biorecognition elements.^{7,9} For example, optical sensors that detect DNA from GM plant material based on surface plasmon resonance (SPR) have been reported widely in literature. Similarly, transgene DNA sequences for the *Bacillus thuringiensis* crystal protein gene, T-Nos sequences, 35S promoter or the NOS gene terminator have been successfully targeted using electrochemical sensors, microarrays, lab-on-a-chip microfluidic capillary electrophoresis systems and quartz crystal microbalance (QCM) sensors. However, in most cases, biosensor-based detection of target transgene sequences has been possible only with PCR-amplified DNA that was isolated from freshly harvested GM samples

We have previously developed biosensor devices based on electrochemical impedance spectroscopy (EIS) for the reliable point-of-care detection of proteins as biomarkers for variety of human disorders.^{10,11} In the current study we set out to explore the application of EIS technology along with Cyclic Voltammetry (CV) for the detection of proteins expressed by GM plant material. Using specific antibodies as bio-recognition elements on the EIS sensor surface, we successfully detected Bt-Cry1Ab and Bt-Cry1F crystal proteins in wheat leaf extracts as well as maize flour with high specificity and sensitivity that is orders-of-magnitude greater than ELISA in wheat extract samples. The proof-of-concept sensor technology developed in this study was further used

to design a functional portable handheld device to serve as a rapid, reliable, easy-to-use, economical tool for the detection of GMO proteins in the field by plant-genetic engineering scientists, representatives of governmental agencies that regulate GM products as well as farmers and consumers.

3.3 Materials & Methods

3.3.1 Sensor Fabrication Process

The electrochemical sensor for the detection of Bt-Crystal proteins in GMO foods were based on our previous experience optimizing electrode configurations that provide the greatest sensitivity and stability for non-faradaic and faradaic measurements in quantitative point-of-care diagnostic devices.¹² The sensor was fabricated on commercially available 0.14 mm thick polyethylene terephthalate (PET) substrates (Dupont). The PET that was first rinsed with 70% v/v isopropanol followed by deionized water to remove any oils and organic residues and stored in a nitrogen desiccator. Gold electrodes of 125nm was deposited on the PET substrate via e-beam vapor deposition.

3.3.2 Functionalization of Electrode Surface for the Detection of Bt-Crystal Proteins

Gold-deposited PET electrodes were functionalized with 10 µg/mL anti-Bt-Cry1Ab or anti-Bt-Cry1F antibodies for the capture and detection of Bt-Cry1Ab and Bt-Cry1F proteins in plant samples (antibody concentration optimization outlined in Chapter 4.4.1). The gold surface was first covalently modified by conjugation al cross-linker DSP [dithiobis(succinimidyl propionate)]. DSP contains an amine-reactive N-hydroxysuccinimide ester at each end of two eight-carbon spacer arms that are linked together with a disulfide bond. The disulphide linkage of DSP chemisorbs rapidly to the gold surface forming monolayers of the DSP molecules on the gold surfaces while the N-hydroxysuccinimide groups are available for binding to the primary amine groups of proteins.^{13,14} After incubation of the gold electrode surface with freshly constituted DSP in DMSO (4 mg/mL) for 30 min at room temperature, excess unreacted crosslinker was washed off twice with 1x phosphate-buffered saline (PBS). Next, either anti-Bt-Cry1Ab or anti-Bt-Cry1F antibodies (1 mg/mL) was added to the DSP-conjugated electrode surface and incubated for 30 minutes. The primary amine groups on the antibodies form covalent bonds with the N-

hydroxysuccinimide esters on the gold-bound DSP to chemically link the antibodies to the gold sensor surface

3.3.3 Preparation of Wheat Leaf Extracts and Corn Flour Samples

Organic non-genetically engineered organic wheat seeds (Amazon) were soaked overnight and planted in commercial potting soil. Two-week-old leaves from the sprouted wheat seeds were harvested. 1 g of leaves were ground with 20mL of 1xPBS buffer using a pestle and mortar. The lysate was centrifuged at 13,200rpm for 5min to remove insoluble material. The supernatant was collected used for all experiments with the GMO sensor and ELISA experiments. Wheat leaf extracts spiked with either 0.01 ng/mL, 1 ng/mL or 100 ng/mL of the Cry1Ab and Cry1F proteins served as experimental samples for the analysis of GM samples while un-spiked extracts were used as non-GM samples.

Finely ground organic whole grain yellow corn flour (1g) was mixed well by vortexing with 20 ml 1xPBS. The mixture was centrifuged at 13,200rpm for 5min to remove insoluble material. The supernatant was used for GMO sensor experiments. Corn flour extracts spiked with either 0.01 ng/mL, 1 ng/mL or 100 ng/mL of the Cry1Ab and Cry1F proteins served as GM samples for the experiment while non-spiked extracts were used as control (non-GM) food samples.

3.3.4 ELISA Analysis of Cry1Ab and Cry1F Proteins in Wheat Leaf Extracts

Conventional immunoassay analysis of wheat leaf extracts was first performed using the Abraxis LLC (Warminster, PA, USA) sandwich ELISA kits for the detection of Bt-Cry1Ab/Ac and Bt-Cry1F proteins as per manufacturer's instructions. Briefly, wheat leaf controls and samples containing Bt-Cry1Ab/Ac OR anti-Bt-Cry1F proteins were added to ELISA plates pre-coated with anti-Bt-Cry1Ab/Ac OR anti-Bt-Cry1F polyclonal antibodies. After incubation to allow antigen binding to their respective antibodies, unbound material was washed off. Enzyme labeled anti-Bt-Cry1Ab/Ac OR anti-Bt-Cry1F polyclonal antibodies was added next to create an antibody-antigen-antibody sandwich on the surface of the ELISA plate. After incubation unbound material was washed off and the extent of antigen-antibody binding is detected by a color reaction as measured by absorbance values using a spectrophotometer. Absorbance data was analyzed and graphed using GraphPad prism to determine the limits of detection of Bt-Cry1Ab and Bt-Cry1F proteins.

3.3.5 Characterization of Electrode Surface Modifications by Fourier-Transform Infrared Spectroscopy (FTIR) Analysis

Gold electrode surface modifications by conjugation of DSP linker molecules followed by anti-Bt-Cry1Ab/anti-Bt-Cry1F antibodies was validated using FTIR analysis. Gold thin films deposited on PET substrates using e-beam vapor deposition at parameters mimicking those used for sensor fabrication was used for the FTIR validation studies. Functionalization of electrode surface was carried out as described in the previous section. Prior to FTIR measurements, each sample was rinsed thoroughly with DI water then dried with N₂ air to rid the surface of any unbound material that may interfere with the analysis. The infrared spectra of surface modified samples were recorded with a Nicolet iS50 FTIR spectrometer. Absorbance spectral measurements were obtained with a scan resolution of 4 cm⁻¹ for 64 scans in the spectral range of 4000 cm⁻¹ to 600 cm⁻¹. Absorption spectra was recorded for the unmodified PET-gold surface, PET-gold surface conjugated to DSP molecules, and the gold surface with antibodies (either anti-Cry1Ab or anti-Cry1F) linked via the DSP linker molecules.

The peaks observed in the DSP spectrum of Figure 3.1 at 1792 cm⁻¹ and 1751 cm⁻¹ indicate the symmetric and asymmetric carbonyl stretches (respectively) of the NHS ester. Furthermore, the peak at 1208 cm⁻¹ confirm the presence of the asymmetric CNC stretch of the NHS ester while the peak at 1069 cm⁻¹ can be identified as the succinimide NCO stretch. Finally, the peak at 1817 cm⁻¹ indicates the ester carbonyl stretch. The presence of these peaks are characteristic of a self-assembled monolayer of DSP¹⁵, confirming the chemisorption of DSP to the gold surface.

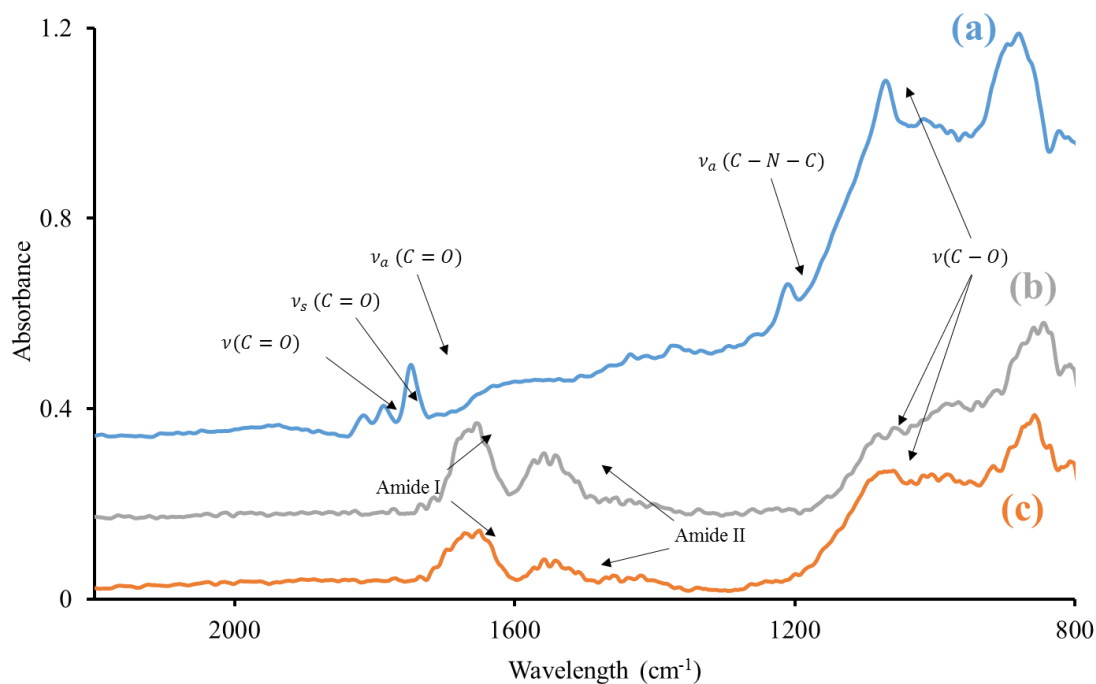


Figure 3.1. FTIR spectra of (a) DSP crosslinker immobilized on Au surface, (b) anti-Cry1Ab immobilized on DSP crosslinker, and (c) anti-Cry1F immobilized on DSP crosslinker.

The reaction between the NHS group with the antibody's primary amine group can be noted in both the anti-Cry1Ab and anti-Cry1F spectrum. The C-O bonds of the NHS ester are broken and react with primary amines of the antibody, resulting in a stable amide bond.¹⁶ A suppression of peaks associated with the NHS ester (1792 cm^{-1} , 1751 cm^{-1} , 1208 cm^{-1}) is observed, while peaks at $\sim 1650\text{ cm}^{-1}$ and $\sim 1550\text{ cm}^{-1}$ are indicative of amide I and amide II peaks. These results show a stable formation of the immunoassay through the binding of either anti-Cry1Ab or anti-Cry1F antibodies to the DSP functionalized surface.

3.3.6 Electrochemical Characterization of Bt-Cry1Ab and Bt-Cry1F Protein Capture on the Sensor Surface

The binding of Bt-Cry1Ab and Bt-Cry1F proteins to their respective antibodies at the sensor surface was analyzed by cyclic voltammetry (CV) and electrochemical Impedance Spectroscopy (EIS) using a redox probe. Both CV & EIS rely on monitoring changes in the electron transfer from the working electrode to the electrolyte containing ferricyanide. The electron transfer kinetics

can be monitored through analysis of the peak faradaic current during CV experiments and charge transfer resistance during EIS experiments. The chemisorption of the immunoassay and subsequent GMO proteins creates a physical barrier between the two phases; this barrier retards electron kinetics and increases the resistance to charge transfer. However, the ferricyanide still needs a pathway from the solution to the electrode surface. This pathway through the SAM is dependent on the structure of the chemisorbed molecules and is ultimately dictated by the adsorption of the DSP to gold surface. As the DSP binds to the gold surface, van der Waals forces influence the packing structure of the monolayer, leaving pin-holes within the SAM and allowing the ferricyanide to transfer electrons to the surface^{2,3,6}. Binding of the antibody, and subsequently the Bt-Cry protein, reduces the size of these pin-holes and inhibits electron transfer kinetics.

A Gamry Reference 600 potentiostat as well as a custom, point-of-use electronic platform were used to conduct the electrochemical experiments. Cyclic voltammetry (CV) and Electrochemical Impedance Spectroscopy (EIS) were employed as rapid, label-free approaches to study the affinity-based detection of both Bt-Cry1Ab and Bt-Cry1F. In CV and EIS, we detect dose dependent changes by leveraging the faradaic charge transfer using a ferricyanide redox probe. Faradaic electrochemical experiments were all carried out in 1x PBS solution containing 1 mM ferricyanide after incubating the Bt-Cry protein on the immunoassay modified gold electrode for 20 minutes. Bt-Cry proteins were first prepared and incubated in PBS to characterize the electrochemical response. After the dose-dependent response was determined in physiological buffer, the Bt-Cry proteins were prepared in 5 g/L of corn flour diluted in 1x PBS, and 5 g/L of wheat leaf extract in 1x PBS, to determine the efficacy of the sensor against GMO food and plant samples.

CV and EIS were selected as complementary techniques to qualitatively and quantitatively study changes at the electrode-electrolyte interface. In CV the electrochemical processes proceed ‘solution-down.’ The ramped potential drives diffusion of the redox probe to/from the electrode surface where it then participates in charge transfer. Immunoassay assembly and subsequent binding with the Bt-Cry proteins retard the diffusion and impede the charge transfer across the electrode. Whereas in EIS, faradaic processes are monitored from ‘electrode-up.’ Immunoassay binding events of the Bt-Cry protein modulate the resistance to charge transfer across the interface.

These resistive changes are observed at low frequencies when a DC bias is applied at the working electrode equal to the equilibrium potential (where no faradaic reactions occur) of the redox probe.

Both CV & EIS rely on monitoring changes in the electron transfer from the working electrode to the electrolyte containing ferricyanide. The electron transfer kinetics can be monitored through analysis of the peak faradaic current during CV experiments and charge transfer resistance during EIS experiments. As the immunoassay is constructed and the Bt-Cry protein binds, the chemisorbed proteins create a physical barrier between the two phases; this barrier retards electron kinetics and increases the resistance to charge transfer. However, the ferricyanide still needs a pathway from the solution to the electrode surface. This pathway through the SAM is dependent on the structure of the chemisorbed molecules and is ultimately dictated by the adsorption of the DSP to gold surface. As the DSP binds to the gold surface, van der Waals forces influence the packing structure of the monolayer, leaving pin-holes within the SAM and allowing the ferricyanide to transfer electrons to the surface.^{13,14,17} Binding of the antibody, and subsequently the Bt-Cry protein, reduces the size of these pin-holes and inhibits electron transfer kinetics.

3.3.6 Evaluation of Dose-Dependent Response via Cyclic Voltammetry

Cyclic voltammograms were recorded in the presence of the ferricyanide redox probe post Bt-Cry protein incubation. The potential was ramped linearly from 0 V to a 0.3 V maximum, and then to a -0.6 V minimum at a scan rate of 50 mV/s. All CV measurements were repeated twice for a total of three cycles to extract data at steady state. The potential window was chosen to capture the redox process of the ferricyanide while excluding any unwanted electrolysis of the PBS buffer. The scan rate was fixed at 50 mV/s, within the linear region of the Randles-Sevcik equation¹⁸ (Equation 3.1) to ensure reversibility of the ferricyanide probe.

In CV, the ferricyanide molecule participates in a single-electron redox reaction when the potential is scanned. At voltages sufficiently below the ferricyanide equilibrium potential, the ferricyanide will accept an electron from the electrode, resulting in cathodic currents. When at values sufficiently above the equilibrium potential, the ferrocyanide donates an electron across the electrode interface, arising in anodic currents.

Peak current values were extracted using the Gamry EChem Analyst™ software. To extract the peak faradaic current values, a baseline was extrapolated from the EDL charging currents. The baselines are constructed by drawing a tangent at the switching potentials of the voltammogram, then calculating the vertical displacement between the peak current and its respective baseline. This extraction removes any capacitive charge transfer from the current response, leaving only current arising from charge transfer across the electrode-electrolyte interface.

The observed peak faradaic current is given by the Randles-Sevcik equation (at 25^o C):

$$i_p = (2.69 * 10^5) n^{3/2} A D^{1/2} C v^{1/2} \quad (3.1)$$

where i_p is the peak cathodic or anodic current, n is the number of electrons transferred per molecule, A is the working electrode surface area (cm²), C is the bulk concentration of the redox probe (mol*cm⁻³), D is the diffusion coefficient (cm²*s⁻¹), and v is the scan rate (mV*s⁻¹). In these experiments, the number of electrons transferred, the bulk ferricyanide concentration, and scan rate were held constant, thus the peak current was dependent only on effective electrode surface area and diffusion to the electrode surface. As Bt-Cry proteins bind to the immunoassay the effective surface area is reduced by proteins bound to the electrode, reducing the peak current response. The physical barrier from the bound proteins also obstruct the diffusion pathway to the electrode, decreasing the mean free path and thus the rates at which the electrons can diffuse to the electrode surface.

3.3.7 Evaluation of Dose-Dependent Response via Electrochemical Impedance Spectroscopy

Faradaic EIS was employed to study changes in the complex impedance spectrum. Measurements were conducted across a frequency range of 1 Hz to 1 MHz. For faradaic EIS measurements, a 10 mV sinusoidal voltage was applied at a DC bias of -0.15 V (the E_0 of the ferricyanide vs Au Ref. as determined by CV measurements). The electrodes are biased such that the redox molecule participates in both oxidation and reduction without being depleted throughout the experiment. The current response was measured, and the complex impedance was calculated by taking the ratio of input voltage to measured current. The impedance spectra were represented as Bode Magnitude and Phase plots (SI) and complex plane plots (Nyquist plots).

For biological systems EIS is commonly leveraged to decouple bulk electrolyte properties from surface phenomena.^{8,19} These chemical processes can be observed through scanning the frequency of the input signal. Here we are leveraging faradaic EIS to observe the oxidation and reduction of a ferricyanide redox probe at the electrode-electrolyte interface. The faradaic reactions occurring across this interface are impacted by the selective binding of Bt-Cry proteins. The bound protein layer influences the dielectric of the interface and modulate the interfacial charge transfer resistance.

3.4 Results & Conclusions

Electrochemical measurements were taken in the presence of a ferricyanide redox probe after Bt-Cry protein incubation. Both Cyclic Voltammetry and Electrochemical Impedance Spectroscopy were employed to study the interfacial changes due to Bt-Cry protein binding events. Samples of either Bt-Cry protein were prepared first in 1x PBS and subsequently in corn flour and wheat leaf extract at concentrations between 0.01 ng/mL and 100 ng/mL.

3.4.1 Evaluation of Input Cyclic Voltammetry Parameters

To determine the optimal scan-rate for subsequent CV experiments, first CV measurements were taken in the presence of the ferricyanide redox probe at varying scan-rates on bare gold sensor (Figure 3.2). Per the Randles-Sevcik equation (Equation 3.1), increasing scan rate corresponds to a proportional increase in the current response. A linear relationship between the current response and square root of the scan rate is plotted in the inset of Figure 3.2. 50 mV/s lies well within the linear region of this range for the bare gold sensor, so it was chosen as the input for subsequent experiments.

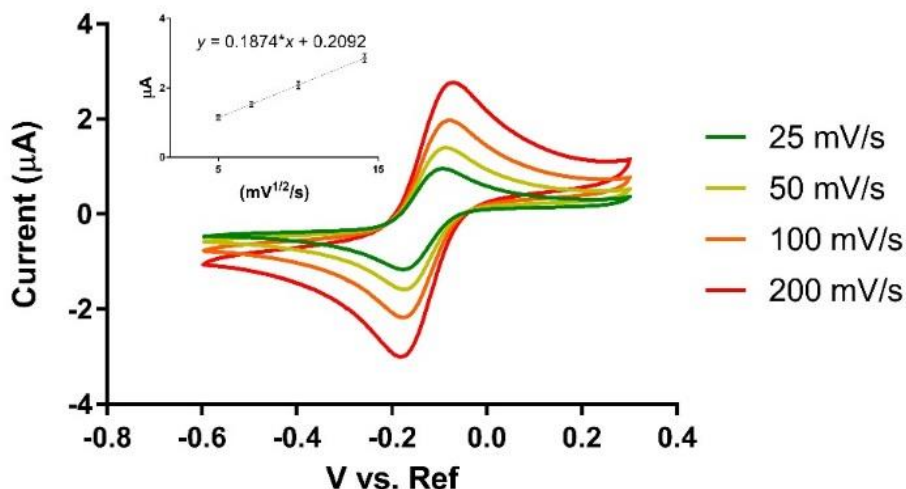


Figure 3.2. Voltammograms recorded in the presence of ferricyanide at varying scan-rates (25 mV/s – 200 mV/s). Insert: Linear correlation between current and the square root of the scan-rate.

3.4.2 Analysis of Dose-Dependent Response via Cyclic Voltammetry in 1x PBS

After determining the operating scan-rate, CV measurements were taken in the presence of the ferricyanide probe after Bt-Cry protein incubation. Cyclic voltammograms were plotted for a non-GMO sample (1x PBS) and increasing concentrations of the Bt-Cry protein (Figure 3.3a-b). A single-electron quasi-reversible reaction is observed in all cases. As the Bt-Cry proteins bind to the immunoassay the peak faradaic current is reduced and an increase in the separation between peak faradaic currents (peak-to-peak separation) is observed. The magnitude of change in peak faradaic current and peak-to-peak separation are dependent on the concentration of Bt-Cry proteins tested. As the concentration of Bt-Cry proteins increases, the observed peak faradaic current decreases and peak-to-peak separation increases.

The peak cathodic current values were found for both Cry1Ab and Cry1F proteins and plotted against concentration as seen in Figure 3.3a-b. A specific signal threshold (SST), the highest apparent concentration when no analytes are present, was estimated from the mean and standard deviation of the non-GMO replicates using Equation 3.2.

$$SST = \mu_{non-GMO} - 3 * SD_{non-GMO} \quad (3.2)$$

The SST was then used to determine the sensor's limits of detection (LOD):

$$LOD = [GMO]_{low} \quad \text{when} \quad (\mu_{[GMO]} + SEM_{[GMO]}) < SST \quad (3.3)$$

The LOD is the lowest distinguishable concentration of the Bt-Cry protein from a non-GMO sample (no Bt-Cry proteins present).^{20,21} The LOD was calculated by adding the mean peak cathodic current to the standard error of the mean (SEM) for each concentration. The lowest concentration distinguishable from the SST was then determined as the LOD for each Bt-Cry protein. The LoDs of Cry1Ab and Cry1F in PBS were 0.01 ng/mL and 0.1 ng/mL, respectively as reported in Table 2.1. Concentrations at and above these LoDs produced peak faradaic current values significantly less than the peak current of the non-GMO sample.

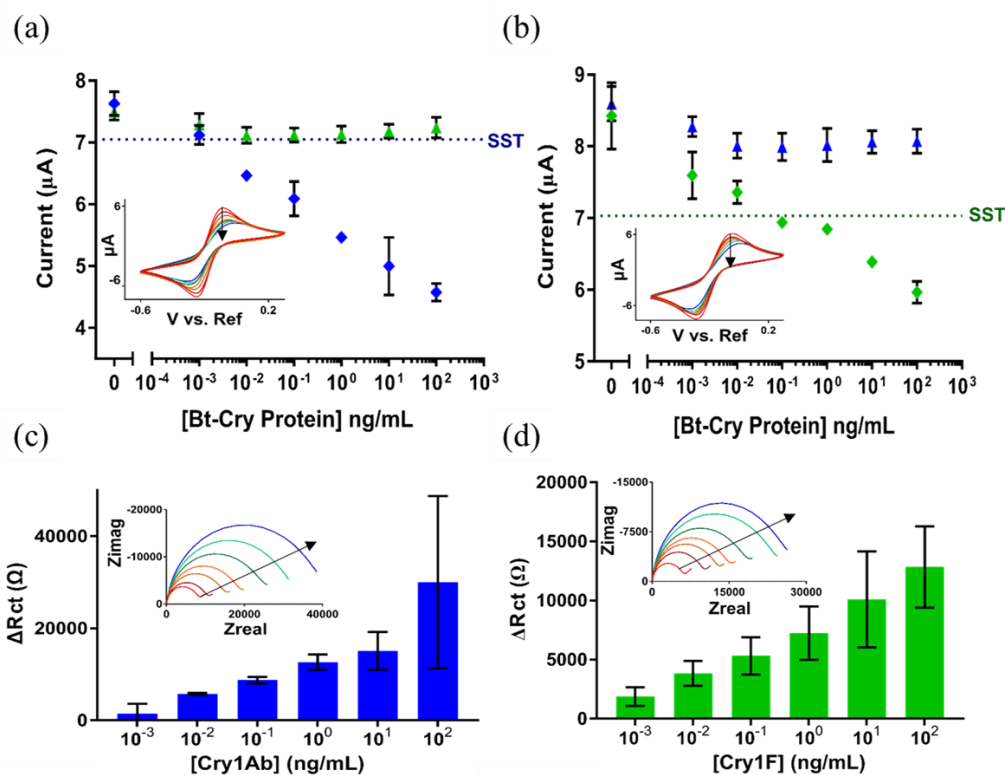


Figure 3.3. CV and EIS response in 1 mM ferricyanide post incubation of various Bt-Cry protein concentrations diluted in PBS. Peak cathodic current versus concentration of both (a) Cry1Ab and (b) Cry1F with voltammogram inserts demonstrating current response across Bt-Cry protein concentration. Change in Rct versus concentration of (c) Cry1Ab and (d) Cry1F with Nyquist plot insets demonstrating the frequency spectrum across Bt-Cry protein concentration. Arrows on all insets represent increasing Bt-Cry protein concentration.

Reducing the effective surface area and limiting the rate of diffusion to the electrode surface not only decrease the peak faradaic current, but also have implications on the reaction rate. Because access to the electrode surface is obstructed, the rate of faradaic charge transfer decreases. This obstruction impacts the time to establish Nernstian equilibrium at the electrode's surface and can be observed in Figure 3.3a-b insets as an increase in the separation between peak faradaic currents as Bt-Cry proteins bind to the immunoassay. This effect was observed for both Bt-Cry proteins and was concentration dependent. With higher Bt-Cry protein concentration, the electron kinetics were slowed, yielding larger peak-to-peak separations.²²

3.4.3 Analysis of Dose-Dependent Response via Electrochemical Impedance Spectroscopy in 1x PBS

The EIS data was fitted to the Randle's circuit^{8,19} to assign values to these chemical processes. The Randle's circuit is the simplest equivalent circuit to describe an electrochemical cell where a single-step Faradaic process occurs. Here, we use this circuit to model the three primary electrochemical processes of the system: the high frequency bulk solution resistance (R_s) between the working and reference electrodes, the mid to low frequency capacitive charging of the electric double layer (C_{dl}), and the low frequency faradaic impedance (Z_f) occurring at the working electrode-electrolyte interface. Z_f can be further divided into a charge transfer resistance (R_{ct}) and a constant phase Warburg impedance (Z_w) which represents the impedance due to mass transport of the redox active species.

As Bt-Cry protein concentration increases, the R_{ct} trends upward. This trend in R_{ct} can be observed in Figure 3.3c-d insets which displays Nyquist plots of the faradaic EIS response at various controlled dose responses. Curves indicate the response after incubating a non-GMO sample (1x PBS) and various concentrations of the Bt-Cry protein. Upon increasing the Bt-Cry protein concentration, the semicircle diameter increases, indicating an increase in the charge transfer resistance across the electrode-electrolyte interface. A similar trend is observed for both Cry1Ab and Cry1F proteins. R_{ct} increases as either Cry1Ab or Cry1F proteins bind to the immunoassay and block the surface from participating in electron transfer with the ferricyanide redox probe.

3.4.4 Analysis of Dose-Dependent Response via Cyclic Voltammetry in Corn Flour and Wheat Leaf Extracts

The additional polysaccharides and proteins found in both corn flour and wheat leaf extract interfere non-specifically with the signal response due to physisorption on the surface of the electrode and substrate, altering the electron's pathway to the electrode. To determine how non-specific physisorption affects sensor performance a time-based study was conducted, incubating non-GMO wheat leaf extract samples on the sensors for 5-minute intervals up to 25 minutes. Here, the charge transfer resistance was monitored to identify the maximum response due to non-specific adsorption, and it was observed (Figure 3.4) that after 20 minutes the charge transfer resistance does not continue to increase. As time of incubation increases, the charge transfer resistance increases until plateauing at around 20 minutes. It was concluded that this increase is driven by physisorption of non-specific molecules within the wheat leaf extract.

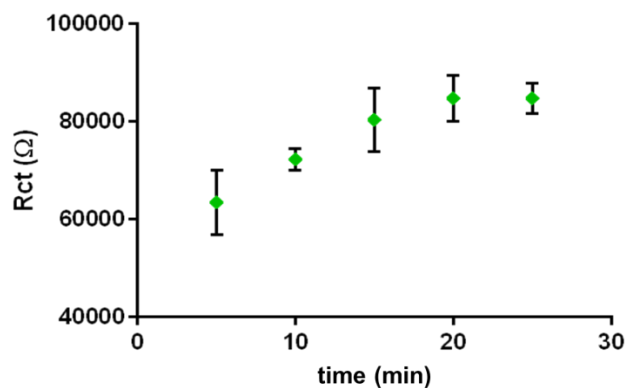


Figure 3.4. Charge transfer resistance plotted against incubation times for non-GMO wheat leaf extract samples on the functionalized sensor (n=3 per time point).

CV plots for Cry1Ab and Cry1F in food sample extracts are shown in Figure 3.5a-b insets (corn flour) and Figure 3.6a-b insets (wheat leaf). During CV experiments, the alteration in electron pathway again manifests as a reduction in the peak faradaic current and widening of the peak-to-peak separation. When compared to the 1x PBS results, the peak faradaic current of the non-GMO samples (extract sample without Bt-Cry proteins) was suppressed by non-specific physisorption of extract constituents. This is a result of additional components within the buffer physisorbing at the electrode's surface, altering the ferricyanide's pathway to participate in the redox reaction.

Non-specific physisorption suppresses the faradaic current response and increases the peak-to-peak separation.

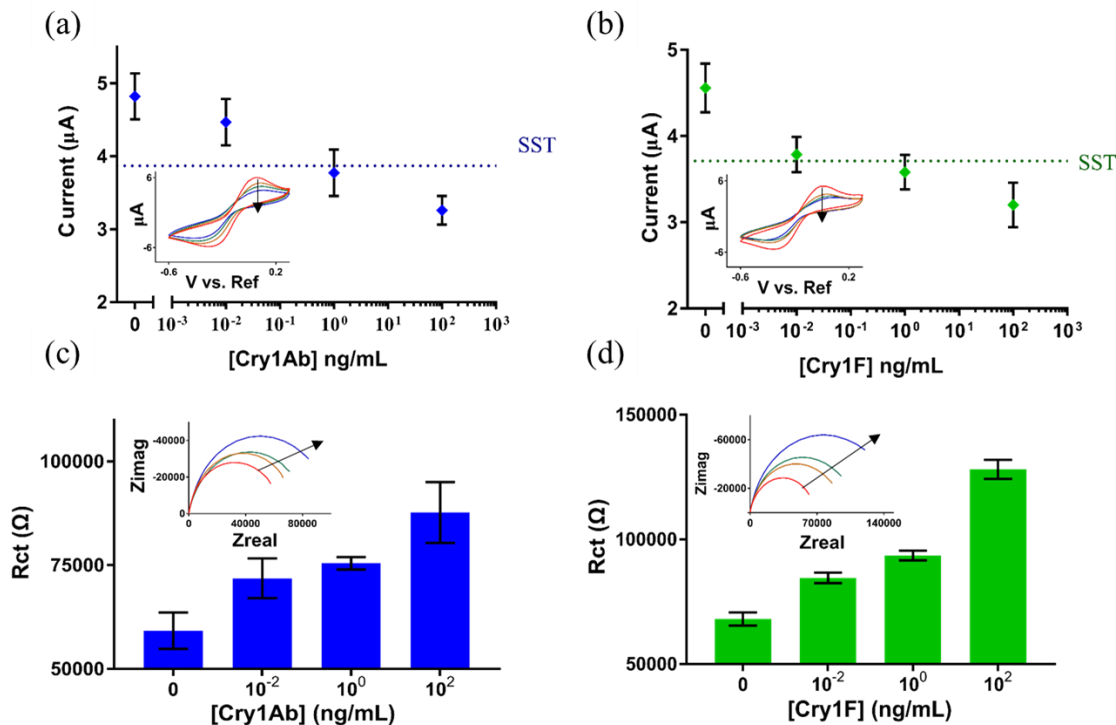


Figure 3.5. CV and EIS response in 1 mM ferricyanide post incubation of various Bt-Cry protein concentrations in corn flour dissolved in PBS. Peak cathodic current versus concentration of both (a) Cry1Ab and (b) Cry1F with voltammogram inserts demonstrating current response across Bt-Cry protein concentration. Rct versus concentration of (c) Cry1Ab and (d) Cry1F with Nyquist plot insets demonstrating the frequency spectrum across Bt-Cry protein concentration. Arrows on all insets represent increasing Bt-Cry protein concentration.

However, it is apparent that the addition of the Cry1Ab or Cry1F results in a further reduction in peak current due to binding to the immunoassay. That is, while physisorbed interferents impact the sensor's faradaic current response, the dose dependent response due to chemisorption was still observed when extracting the peak faradaic currents. Physisorption at the electrode is limited due to the physical and electrochemical barriers. The self-assembled modifications of the electrode results in a tightly packed immunoassay, which limits physisorption at the electrode interface due to both physical and steric hinderances. The LoDs for both Cry1Ab and Cry1F were again

determined using the SST equation for doses spiked in corn flour. The LOD was 100 ng/mL for both Cry1Ab and Cry1F proteins.

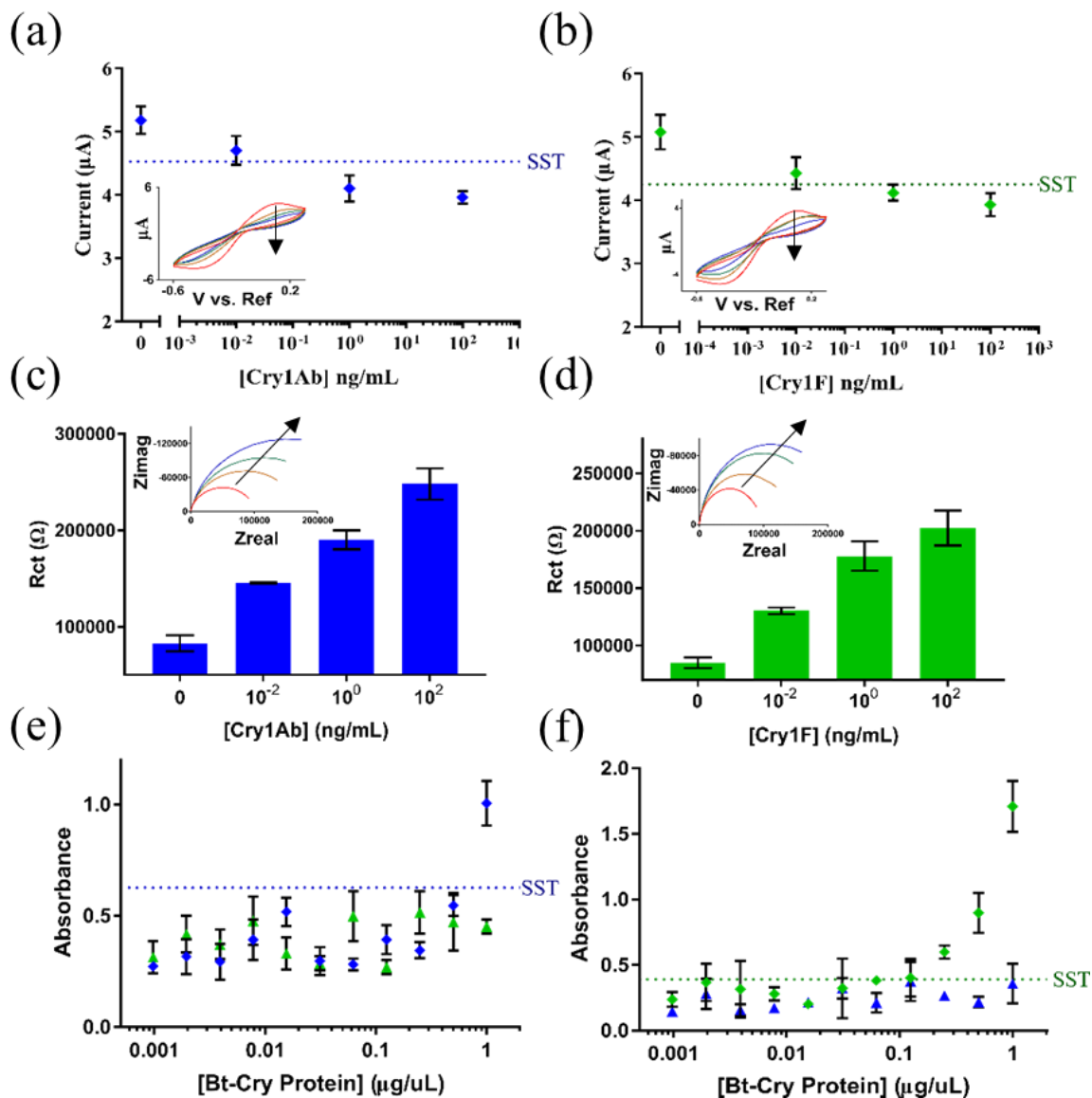


Figure 3.6. CV and EIS response in 1 mM ferricyanide post incubation of various Bt-Cry protein concentrations in wheat leaf extract diluted in 1x PBS. Peak cathodic current versus concentration of both (a) Cry1Ab and (b) Cry1F with voltammogram insets demonstrating current response across Bt-Cry protein concentration. Rct versus concentration of (c) Cry1Ab and (d) Cry1F with Nyquist plot insets demonstrating the frequency spectrum across Bt-Cry protein concentration. Arrows on all insets represent increasing Bt-Cry protein concentration, (e-f) Absorbance results from commercially available ELISA kits.

The faradaic response for Bt-Cry proteins diluted in wheat leaf extract is affected considerably more than the corn flour extracts, as seen in when comparing Figure 3.5 to Figure 3.6, due to the additional interferences present in the wheat leaf extract. Increasing the Bt-Cry protein concentration still resulted in a decreasing current trend, however peak faradaic current values were not extracted, because the faradaic currents could not be reliably distinguished from the capacitive charging currents. Rather, the minimum current was plotted to represent the largest faradaic response and plotted in Figure 3.6a-b.

3.4.5 Analysis of Dose-Dependent Response via Electrochemical Impedance Spectroscopy in Corn Flour and Wheat Leaf Extracts

During EIS measurements, it was noted that the presence of the corn extract altered the charge transfer resistance baselines (R_{ct} values after incubating a non-GMO sample) due to non-specific physisorption of the polysaccharides and proteins. However, it is still noted that increasing the Bt-Cry protein concentration results in a R_{ct} increase as seen in the Nyquist plots of Figure 3.5c-d and Figure 3.6c-d. Here, the semicircles are incomplete within the frequency range, however charge transfer resistance can be extrapolated from the measured data by fitting to the Randle's Circuit.

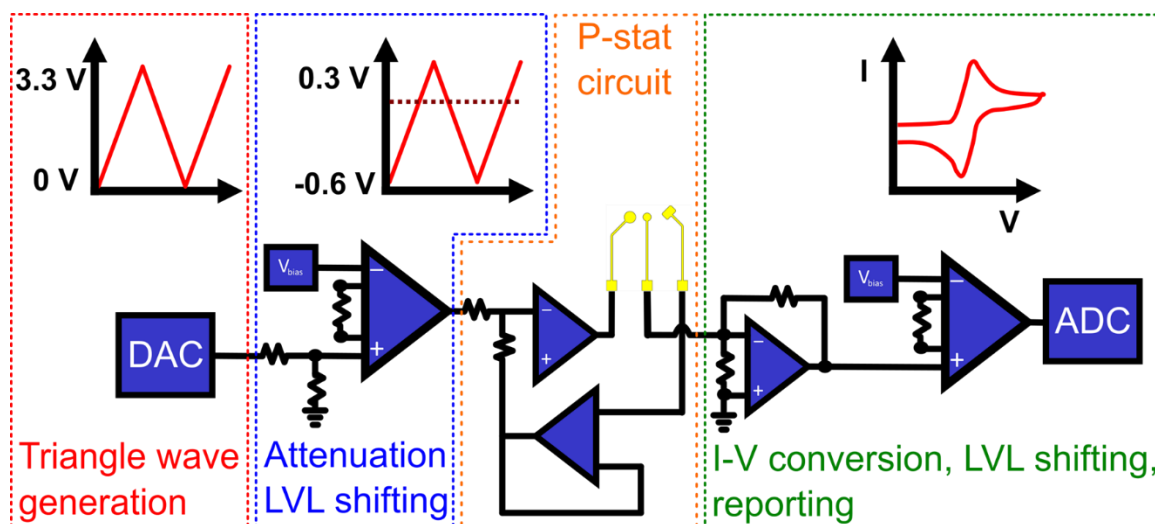


Figure 3.7. Circuit breakdown of the custom electronic platform: Triangle-wave generation via a digital-to-analog converter (red), attenuation of the signal (blue), potentiostat circuit for measuring the signal (orange), and level shifting and reporting (orange).

3.4.6 Hand-held Electronics Platform for Dose-Dependent Response via Cyclic Voltammetry

The custom electronic platform for portable point-of-use cyclic voltammetry measurements was constructed utilizing conventional off-shelf components. A schematic of the circuit used for signal generation and reporting can be seen in Figure 3.7. For this research prototype Adafruit Feather M0 microcontrollers were used for their convenient architecture and miniature form-factor. The microcontroller was used to control all peripheral integrated circuits as well as store and report resulting device output. It is imperative in cyclic voltammetry for negative voltages and currents to be generated and recorded respectively. However, the microcontroller cannot inherently generate negative excitation voltages. To address this, a charge pump voltage inverter (TPS60403DBVR) was used to generate a negative rail for the excitation signal and sensing circuit. An MCP4725 digital-to-analog converter was used to generate a triangle wave of 3.3 V in amplitude at the desired frequency. The signal was then attenuated to 900 mV using a voltage divider and summed (AD8605) with a -600 mV DC signal to produce the desired -600 to 300 mV cyclic voltammetry sweep. The generated potential was used as the excitation potential in a standard potentiostatic circuit, which was constructed from a series of AD8605's. The current at the working electrode was fed into a I-V converter (INA121) before being level shifted into a purely positive voltage regime for analog-to-digital conversion using an ADS1115. The excitation voltage was fed into the analog-to-digital converter to ensure accurate plotting of current with respect to voltage during post-processing. For simplification, the data was manually captured by the user for analysis, however the system boasts a data storage module as well as a Bluetooth communication module for wireless reporting to the user.

CV measurements on the custom electronic platform were taken side-by-side with the Gamry potentiostat when measuring either non-GMO or Cry1Ab spiked corn flour samples. After extracting peak current values, a Bland-Altman Plot²³ (Figure 3.8b) was constructed to determine the statistical agreement between the two measurement techniques. The Bland-Altman Plot graphs the difference between the Gamry and custom platform along the y-axis and the mean result between these two methods on the x-axis. While the custom platform measures -0.097 μA less than the Gamry, this bias is insignificant because the line of equality (bias = 0) falls within the 95% confidence intervals of the mean difference (not plotted). This result shows that the response

on the custom platform matches the expected response on the Gamry, and is not constantly over- or underestimating the current.^{23,24}

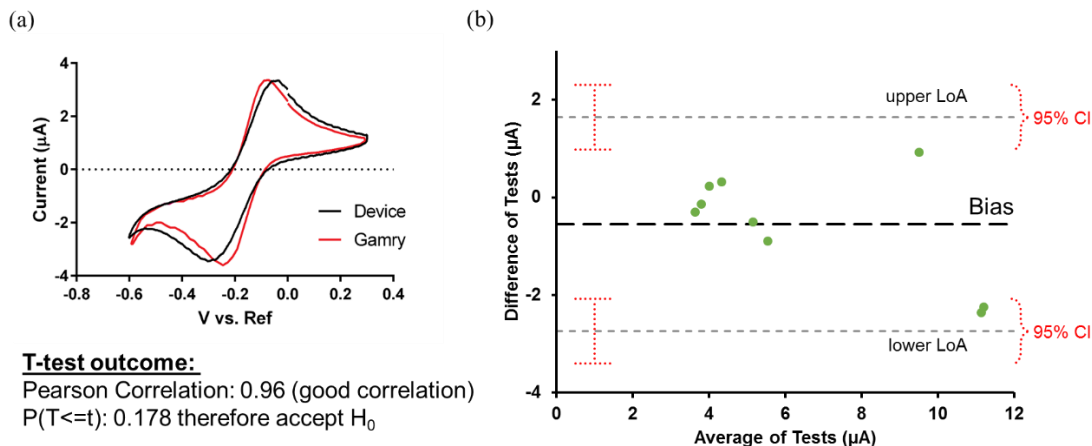


Figure 3.8. (a) Visual comparison between CV outputs measured on custom (black) and Gamry (red) potentiostats, (b) Bland-Altman Plot comparing the difference in extracted peak current vs the average of extracted peak current for both potentiostats.

Upper and lower limits of agreement (LoA) were constructed to determine if the two tests are in agreement. These limits ($-0.8336 \mu\text{A}$, $0.6521 \mu\text{A}$) are established to determine the range in the data over which 95% of the differences between the two measurements will lie between. A maximum allowable current difference was set at $1.56 \mu\text{A}$, corresponding to the current difference between non-GMO and the LOD for Cry1Ab spiked in corn flour. Because neither LoA exceeds this maximum allowable difference, even when accounting for 95% confidence intervals, the Gamry and the custom electronics platform are in agreement, and can be used interchangeably for GMO protein detection. A paired student's t-test was also performed to determine statistical correlation of the data. The Pearson's correlation coefficient of 0.96 indicates good correlation between the two measurements, and the t-test showed no statistical difference between Gamry or custom platform measurements.

3.5 Discussion

This work is the first, based on our review of literature in the published domain, to report a handheld device capable of detecting GMO proteins down to the 10 pg/mL range. Furthermore, this work demonstrates a sensor platform easily convertible between detecting two different GMO

protein variants within multiple food sample extracts. The sensor outperforms commercially available ELISA kits in wheat leaf extracts (Figure 3.6), making it a potentially viable alternative for GMO protein detection in plant extract samples.

This technology we have developed could feasibly fill the demand vacuum for a rapid point-of-use GMO screening device. With its sensitive limit of detection for recombinant proteins, this sensor could benefit genetic engineering scientists by reducing detection times and increasing confidence in GMO protein screening tests. Faster screening of crops for expression of post-translational genetic modifications would streamline the process of validating recombinant protein heritability and or stability. Further, this ultra-sensitive platform allows for detection of much smaller quantities of GMO proteins, reducing the possibilities for a false negative (type II error). We have also demonstrated in cross-reactivity studies that similar proteins do not elicit a response, therefore minimizing the false positive (type I error) rate. Reducing these error rates in an easy to use platform would instill more trust in the product quality for regulators, the agricultural and biotech industries, and the consumer marketplace.

3.5.1 Future Work

We have demonstrated a strong proof of feasibility toward a rapid, handheld device toward GMO protein detection. Because the sensor tests directly for GMO proteins, it can be leveraged in cases where the genetic information is irrelevant or too difficult to detect. Recombinant proteins are often more stable than DNA so direct detection of these proteins, coupled with the low sample volume, make this portable GMO an attractive prototype for direct detection in plant samples and processed foods.

Antibodies can be created for nearly any target antigen, and we have demonstrated that by simply swapping out the antibody robust control over the platform's specificity can be achieved. Thus, it is feasible that this platform can translate to detect other GMO proteins either individually or in a multiplexed fashion. Furthermore, we have demonstrated analogous results using our custom-built platform to the desktop potentiostat. Our platform has low input power requirements and a much smaller form factor demonstrating its feasibility as a rapid point-of-use GMO test.

3.6 Statistical Analysis

All data was analyzed using Prism Graphpad. Data is presented as mean \pm std.deviation, with all error bars representing n=3 replicates.

3.7 References

1. James, C. Global review of commercialized transgenic crops. *Curr. Sci.* **84**, 303–309 (2003).
2. Flachowsky, H., Hanke, M., Peil, A., Strauss, S. H. & Fladung, M. A review on transgenic approaches to accelerate breeding of woody plants. *Plant Breed.* **128**, 217–226 (2009).
3. Brookes, G. & Barfoot, P. GM crops: The global economic and environmental impact—The first nine years 1996-2004. (2005).
4. James, C. Global status of commercialized biotech/GM crops: 2014. *ISAAA Br.* **49**, (2015).
5. MATSUOKA, T. *et al.* A Multiplex PCR Method of Detecting Recombinant DNAs from Five Lines of Genetically Modified Maize. *J. Food Hyg. Soc. Japan (Shokuhin Eiseigaku Zasshi)* **42**, 24–32 (2001).
6. Benbrook, C. M. Impacts of genetically engineered crops on pesticide use in the US--the first sixteen years. *Environ. Sci. Eur.* **24**, 24 (2012).
7. Ahmed, F. E. Detection of genetically modified organisms in foods. *TRENDS Biotechnol.* **20**, 215–223 (2002).
8. Daniels, J. S. & Pourmand, N. Label-free impedance biosensors: Opportunities and challenges. *Electroanalysis* **19**, 1239–1257 (2007).
9. Ermolli, M. *et al.* Food safety: screening tests used to detect and quantify GMO proteins. *Accredit. Qual. Assur.* **11**, 55–57 (2006).
10. Panneer Selvam, A. & Prasad, S. Companion and Point-of-Care Sensor System for Rapid Multiplexed Detection of a Panel of Infectious Disease Markers. *SLAS Technol. Transl. Life Sci. Innov.* **22**, 338–347 (2017).
11. Munje, R. D., Muthukumar, S. & Prasad, S. Lancet-free and label-free diagnostics of glucose in sweat using Zinc Oxide based flexible bioelectronics. *Sensors Actuators B Chem.* **238**, 482–490 (2017).
12. Stevenson, H., Radha Shanmugam, N., Paneer Selvam, A. & Prasad, S. The Anatomy of a Nonfaradaic Electrochemical Biosensor. *SLAS Technol. Transl. Life Sci. Innov.* **23**, 5–15 (2017).
13. Vericat, C., Vela, M. E., Benitez, G., Carro, P. & Salvarezza, R. C. Self-assembled monolayers of thiols and dithiols on gold: new challenges for a well-known system. *Chem. Soc. Rev.* **39**, 1805–1834 (2010).
14. Häkkinen, H. The gold–sulfur interface at the nanoscale. *Nat. Chem.* **4**, 443 (2012).
15. Lim, C. Y. *et al.* Succinimidyl Ester Surface Chemistry: Implications of the Competition between Aminolysis and Hydrolysis on Covalent Protein Immobilization. *Langmuir* **30**, 12868–12878 (2014).

16. Munje, R. D., Muthukumar, S., Jagannath, B. & Prasad, S. A new paradigm in sweat based wearable diagnostics biosensors using Room Temperature Ionic Liquids (RTILs). *Sci. Rep.* **7**, 1950 (2017).
17. Porter, M. D., Bright, T. B., Allara, D. L. & Chidsey, C. E. D. Spontaneously organized molecular assemblies. 4. Structural characterization of n-alkyl thiol monolayers on gold by optical ellipsometry, infrared spectroscopy, and electrochemistry. *J. Am. Chem. Soc.* **109**, 3559–3568 (1987).
18. Zanello, P. *Inorganic electrochemistry: theory, practice and application*. (Royal Society of Chemistry, 2007).
19. Nicholson, R. S. Theory and application of cyclic voltammetry for measurement of electrode reaction kinetics. *Anal. Chem.* **37**, 1351–1355 (1965).
20. MacDougall, D. & Crummett, W. B. Guidelines for data acquisition and data quality evaluation in environmental chemistry. *Anal. Chem.* **52**, 2242–2249 (1980).
21. McNaught, A. D. & McNaught, A. D. *Compendium of chemical terminology*. **1669**, (Blackwell Science Oxford, 1997).
22. Pei, R., Cheng, Z., Wang, E. & Yang, X. Amplification of antigen–antibody interactions based on biotin labeled protein–streptavidin network complex using impedance spectroscopy. *Biosens. Bioelectron.* **16**, 355–361 (2001).
23. M., B. J. & G., A. D. Applying the right statistics: analyses of measurement studies. *Ultrasound Obstet. Gynecol.* **22**, 85–93 (2003).
24. Giavarina, D. Understanding Bland Altman analysis. *Biochem. Medica* **25**, 141–151 (2015).

CHAPTER 4

WHEAT VIRUS SENSOR

4.1 Abstract

Wheat is an important global commodity in terms of acreage grown and trade value as it is a staple in household diets. Its appeal for foodstuffs lies in its properties as a non-perishable, nutritious and lasting source of carbohydrates. Crop loss can have devastating effects on not just local economies but global food supplies as many third-world countries rely on just a few key sources that produce the crop. Invasive parasites such as the wheat spindle streak mosaic virus (WSSMV) and the soil borne wheat mosaic virus (SBWMV) can lead to significant crop losses as these viruses show few symptoms before spreading. Preemptive methods to control infection include burning - to raze volunteer wheat - and regular applications of the herbicide glyphosate to deter mite migration. Conventional pathogen detection methods are a slow response tactic requiring highly specialized laboratories and personnel. We present an alternative to slow-response methods with portable, rapid-response, affinity based electrochemical biosensors that possess a high degree of sensitivity and selectivity towards both the WSSMV in infected sap.

4.2 Introduction

Grains are currently the largest component of human food consumption with wheat making approximately 21% of the world's food.¹ Wheat is a value-added commodity, its modification into livestock feed, medications, beauty products, and alcohol production make it a more valuable crop than the grain alone.^{2,3} Approximately 750 million metric tons of wheat are produced annually, requiring 240 million hectares of farmland to support this growing demand.⁴ Wheat is cultivated on more land area than any other food crop, and world trade in wheat is greater than all other crops combined.⁵ Despite a small decline in wheat consumption due to fad diets, wheat continues to remain a cornerstone for a great many products and industries. In the United States alone, approximately 1700 million bushels of wheat were produced in 2017 at \$4.72 per bushel, with the total production value at 8.212 billion USD. While the US is ranked third in terms of production volume the US exports nearly 50% of its total wheat production – a \$5.13 billion value – making it the leading exporter of wheat. In its domestic uses, wheat is prominent in the pharmaceutical

industry as gluten is used to manufacture edible capsules, the paper industry uses it to coat paper products and the health and beauty industry uses wheat germ in soaps, creams, etc. Wheat also plays a small role in bioethanol production.⁶

Cumulative losses each year in wheat crops are in small part to drastic climate changes that bring rain, blights (fungal diseases), rust pathogens and in large part to pests and insects that transmit deadly viruses. Two viruses in particular – the wheat spindle streak mosaic virus (WSSMV) and the soil borne wheat mosaic virus (SBWMV) – inflict significant damage and crop loss.⁷

WSSMV infection typically occurs in the seedling or preliminary growing phases through vector transmission via the curl mite (*Aceria tosichella*).^{8,9} Symptoms of this viral infection are characterized by growth stunting, chlorosis or the breakdown and leakage of chlorophyll within the plant leaves, necrosis and eventually plant death.¹⁰ The WSSMV virus survives in non-wheat crops and grasses as alternative hosts during off-season, forming a “green bridge” from the alternative to the primary host for infestation and infection by the mite and virus.⁸ Mites are carried from these alternative hosts to crops closest to the edge of the field then move inward depending on wind propagation. Farmers typically resort to excessive herbicide use to deter mite migration inward from the volunteer wheat and most often raze the areas of the fields with volunteer wheat and crops with suspected infection to destroy the green bridges and prevent infection from occurring in the first place. There is no documented natural resistance to infection in wheat crops and even the genetically modified strains exhibit temperature dependent resistance.^{11,12}

Infection by the SBWMV is contingent on several environmental conditions being optimal for the slime mold vector to become active.¹³ The mold spores containing the viruses can remain dormant for up to 30 years for the conditions to be conducive to growth. For instance, the soil pores must be filled with water for significant viral transmission to occur to seedlings and plants in the preliminary growth phase and the soil temperature must range in between 15° C to 30° C depending on the location suggesting that the virus is best transmitted in the temperate autumn or spring months. The symptoms expressed with SBWMV include irregular chlorotic patches on the field, mottling or streaking and short bunched growth. Infection prevention methods typically include soil fumigants, but it is not an economically viable process as it damages the soil for future crop growth.

The financial losses born out of herbicide purchase and application, equipment sanitization, crop destruction, damage and repair costs of irrigation systems are all absorbed by farmers because of the promise of marginal profits. Preemptive methods to control infection include burning – to raze volunteer wheat – and regular applications of the herbicide glyphosate to deter mite migration.¹⁴ The unfortunate side effect of herbicide application is the spread of resistant weeds despite increased and more frequent applications. Growing exposure to glyphosate in air, food and ground water raises concerns about the probable carcinogenic effects and risks to human health. In the long term, these deterrents are neither ecologically nor economically feasible.¹⁴

The alternative to preemptive destruction is early detection and selective destruction of infected wheat crops. Some solutions offered include serological testing such as multiplex real time polymerase chain reaction (RT-PCR) or ELISA testing to selectively identify infected crops.^{15,16,17} Both these methods are time and resource consuming as they are slow-response tactics requiring highly specialized laboratories and personnel to perform and interpret the test results.

Our lab has developed biosensor technologies utilizing various electrochemical measurement techniques for the reliable point-of-use detection of proteins and other biomarkers for a variety of applications within the human health and wellness industry as well as various agricultural applications. This paper presents an alternative to the current methods of wheat pathogen detection through the application of Electrochemical Impedance Spectroscopy (EIS). Specific antibodies were used as bio-recognition elements on the sensor surface to detect both WSSMV and SBWMV viruses in infected sap. The prototype pathogen sensor serves as a rapid, reliable, easy-to-use, economical tool that could benefit Agriculturalists and representatives of governmental agencies like the FDA and USDA that regulate food products.

4.3 Experimental Section

4.3.1 Sensor Fabrication Process

The biosensor was fabricated on PET substrates using the e-beam deposition technique. Electrodes were deposited using electron beam physical vapor deposition at a pressure of $5 * 10^{-6}$ torr. The electrode patterns were deposited with 125 nm Au onto the precleaned PET substrate. After fabrication, the surface of the gold electrodes and the PET substrate were rinsed with 70%

Isopropyl Alcohol (IPA), and distilled water (DI water) to remove organic residues. The electrodes were then dried with inert N₂ gas to prepare the surface for self-assembly of the immunoassay.

Gold-deposited PET electrodes were functionalized with anti-WSSMV and anti-SBWMV antibodies for the capture and detection of WSSMV and SBWMV wheat pathogens. The disulfide within DSP readily chemisorbs to the gold electrodes resulting in the N-hydroxysuccinimide ester (NHS ester) groups pointing orthogonally to the sensor surface. After incubation of the gold electrode surface with freshly constituted DSP in DMSO (4 mg/ml) for 60 min at room temperature, excess unreacted crosslinker was washed off twice with 1x phosphate-buffered saline (PBS). Next, either anti-WSSMV or anti-SBWMV antibodies (5 mg/mL) were added to the DSP-modified electrode surface and incubated for 60 minutes. The primary amine groups on the antibodies form covalent bonds with the N-hydroxysuccinimide esters on the gold-bound DSP to chemically link the antibodies to the gold sensor surface. These antibodies possess high affinity toward the pathogens allowing for rapid binding interactions.

4.3.2 Electrochemical Evaluation of Biosensor Surface Modification via Electrochemical Impedance Spectroscopy

Interfacial changes in response to chemisorption of the immunoassay or subsequent dosing of the WSSMV or SBWMV pathogens were monitored through electrochemical experiments using a Gamry Reference 600 potentiostat. Non-faradaic electrical impedance spectroscopy (EIS) was used as a label-free approach to decouple bulk electrolyte properties from surface phenomena and to quantify impedance changes due to binding events. An input 10 mV sinusoidal voltage with a DC bias of -0.3 V vs. Au Ref. was applied at the working electrode and scanned across a frequency range of 1 Hz – 1 MHz. The resultant current response was measured, and the complex impedance was calculated as the ratio of the input voltage to the output current.

As molecules chemisorb on the sensor surface, the double-layer capacitance, SAM permittivity, and interfacial relaxation processes are all modulated. As immunoassay binds to the gold surface, van der Waals forces influence the packing structure of the monolayer, leaving pin-holes within the SAM, allowing ionic ingress at sufficient applied DC biases.

4.4 Results and Discussion

4.4.1 Antibody Saturation

WSSMV and SBWMV antibodies belong to a general class of immunoglobulin G antibodies. An optimal antibody concentration range was determined theoretically using the planar density of the DSP SAM layers and ratio of atomic diameters of an IgG antibody to that of DSP:

$$\rho_{DSP} * A_{electrodes} * \frac{d_{atom_{DSP}}}{d_{hydrodynamic_{IgG}}} * M_{IgG} * 10^6 * \frac{1}{V_{fluid}} = [antibody] \quad (4.1)$$

Equation 4.1 models the relationship between the planar density of DSP and the concentration of the antibody: ρ_{DSP} is the density of the DSP SAM layer on a planar gold, $6.67 * 10^{-10}$ mol cm⁻¹ [6]. $A_{electrodes}$ is the total surface area of the gold electrodes and leads within the sensing region; it was approximated using AutoCAD as 0.041710 cm². The ratio of atomic and molecular diameters of the DSP to a general class of IgG antibodies, $d_{atom_{DSP}}$ and $d_{hydrodynamic_{IgG}}$ respectively, was calculated to be 1:37 [6,7]. These constants multiplied with the molar mass of the antibody (M_{IgG}) as 1.5×10^{11} μg mol⁻¹ [7] and divided by the volume of the fluid (V_{fluid}), in the sensing region, here 60 μL. This equation then allowed for the approximation of the optimal antibody concentration as 1.88 μg/ml. This value holds true if the antibodies bind in an upright, uniform layer with only the Fc portion of the antibody binding to the DSP monolayer. However, accounting for improperly oriented or “hooked” antibodies (antibodies wedged in between others that do not dislodge during wash steps), a concentration of 5 μg/ml was used for biosensing application. The same optimization protocol was used to select the operating concentration of antibody for each of the sensors in Chapter 3, 5, & 6 (data not shown).

4.4.2 Calibrated Dose Response

After antibody incubation, a measurement was performed in 1x PBS with no antigens present to serve as a ‘blank’ comparison test for the subsequent WSSMV or SWBMV doses. Lyophilized wheat pathogen antigens were reconstituted and diluted in 1x PBS to form concentrations from 0.01 ng/mL to 10 ng/mL. The limits of the concentration range were selected based on ELISA kits developed for each of the pathogens.¹⁸ As the pathogen binds to the immunoassay, the capacitive response within the EDL is modulated.

The resulting complex impedance and complex capacitance Nyquist plots are shown in figure 4.1a-b (WSSMV) and 4.2a-b (SBWMV). The Nyquist impedance plot in 4.1a carry information about the bulk interfacial capacitance changes as the WSSMV pathogen binds to the electrode surface, however these changes are not entirely resolvable, thus the data are represented using a Nyquist capacitance plot (Figure 4.2b) to resolve SAM dipolar characteristics and ionic permittivity.

For each of the dose steps, the Nyquist capacitance plot exhibits a large higher frequency semicircle with a less pronounced, mid- to low-frequency semicircle and a 45° diffusion tail at ultra-low frequencies. Each of the semicircles corresponds to a time constant indicating that the immunoassay experiences two relaxation events. As additional wheat pathogens are introduced onto the sensor, a consequent decrease in the large semicircle diameter is observed. The decrease in semicircle diameter corresponds to a lengthening of the immunoassay and hindrance of ionic ingress toward the electrode surface. As antigen concentration increases rotational hinderance increases, reducing the size and number of pin holes in the immunoassay.

The changes in bulk interfacial capacitance for the SBWMV also exhibited poor resolution in the Nyquist plot of Figure 4.2a, but a similar complex capacitance response was observed in the SBWMV Nyquist capacitance plot as shown in Figure 4.2b. With higher concentrations of the SBWMV introduced onto the sensor surface, the higher-frequency semicircle also exhibits a decrease in diameter, indicating alteration in the dielectric relaxation of the immunoassay and hindrance of ionic ingress toward the electrode surface.

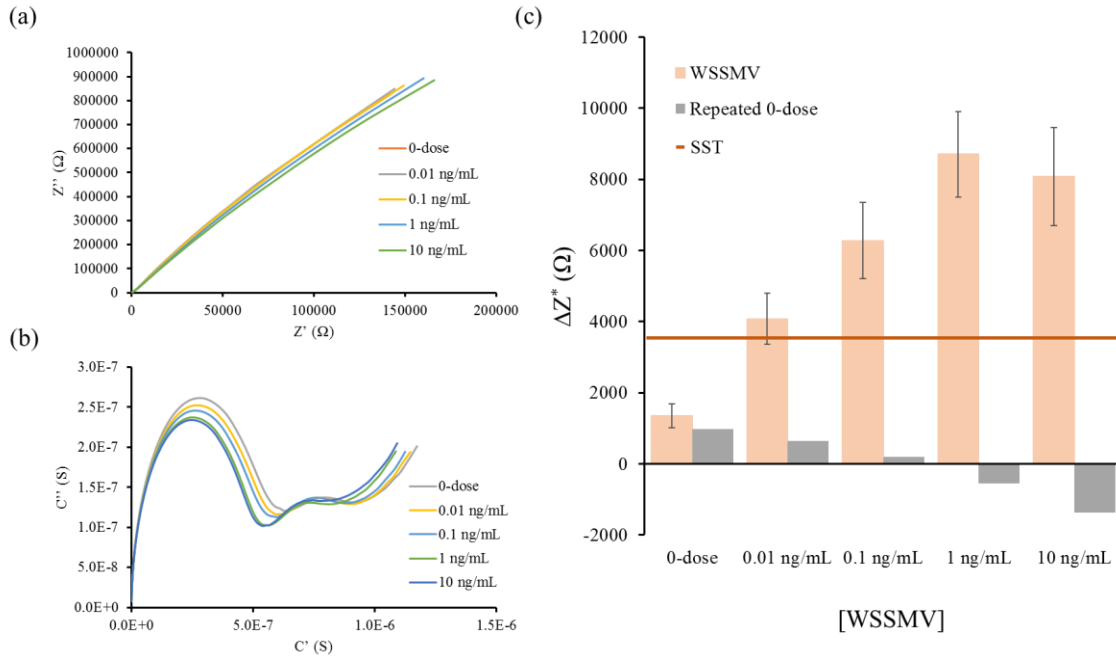


Figure 4.1. Sensor performance in EIS experiments across calibrated doses of WSSMV in 1x PBS. (a) Nyquist Impedance Plot across WSSMV doses, and (d) transformed Nyquist Capacitive Plot across doses. (c) Change in Z^* at 10 Hz with respect to antibody measurement for varying concentrations of WSSMV (blue) and for repeated 0-dose measurements (grey).

To explore dose-dependent changes for each of the wheat pathogens, the impedance at 10 Hz was plotted as a function of the antigen dose. To account for sensor-to-sensor variability each measurement was normalized to a measurement taken after antibody incubation by subtracting the Z^* values at 10 Hz. The change in impedance per each concentration of the WSSMV and SBWMV pathogens was plotted in Figure 4.1c and in Figure 4.2c respectively. The dynamic range of the sensor response ranged from 4074 Ω (0.01 ng/mL) to 8083 Ω (10 ng/mL) for the WSSMV pathogen while the dynamic range for the SBWMV pathogen ranged from 3244 Ω (0.01 ng/mL) and 12.18 k Ω (10 ng/mL).

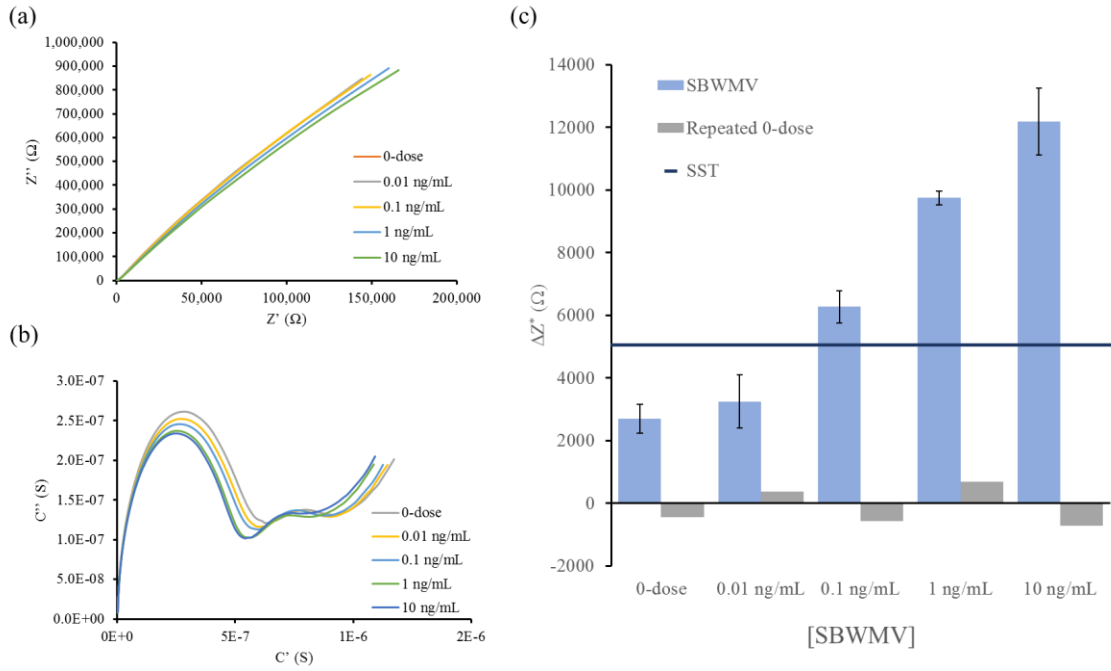


Figure 4.2. Sensor performance in EIS experiments across calibrated doses of SBWMV in 1x PBS. (a) Nyquist Impedance Plot across SBWMV doses, and (d) transformed Nyquist Capacitive Plot across doses. (c) Change in Z^* at 10 Hz with respect to antibody measurement for varying concentrations of SBWMV (blue) and for repeated 0-dose measurements (grey).

A specific signal threshold (SST) was calculated based on the signal to noise ratio of 3 as indicated in Equation 4.2 below:

$$SST = \mu_{0-dose} - 3 * \sigma_{0-dose} \quad (4.2)$$

where μ_{0-dose} and σ_{0-dose} represents the mean and standard deviation of the 0-dose measurement. The limit of detection (LOD) is defined as the lowest concentration of WSSMV and SBWMV pathogen that can be detected reliably from a blank solution. Equation 4.3 was then used to determine that the LOD for WSSMV antigens:

$$LOD = [pathogen]_{low} \quad when \quad (\mu_{[pathogen]} - SEM_{[pathogen]}) > SST \quad (4.3)$$

The LOD was found by subtracting the SEM for each concentration of the pathogen ($SEM_{[pathogen]}$) from the mean $\mu_{[pathogen]}$. This value was then compared to the SST for each concentration of the pathogens, and the lowest concentration that exhibited a value larger than the

SST was determined as the LOD. Concentrations at and above the LOD show significant impedance responses indicating the pathogens are reliably detected. Using Equation 4.3, the LOD for WSSMV was 0.01 ng/mL and the LOD for SBWMV antigens was 0.1 ng/mL

4.5 Conclusion

Wheat is among the most important crops in terms of production and human caloric intake. Maintaining and increasing global wheat production hinges on ensuring high yields per area of farmland. Crop loss due to viral infection is a major concern, and current methods of restricting the spread of these infections rely on burning and sacrificing much of the surrounding crops. This cost either must be absorbed by either the farmer or the end consumer, leading to increased wheat prices. Here, a biosensor has been proposed to detect the presence of two common wheat pathogens: the wheat spindle streak mosaic virus and the soil borne wheat mosaic virus. The sensor utilizes electrochemical impedance spectroscopy to monitor interfacial capacitive changes as the virus binds to an immunoassay at the sensor surface. Using highly specific antibodies, the sensor has very low detection limits: 0.01 ng/mL for the WSSMV and 0.1 ng/mL for the SBWMV when detecting reconstituted samples.

4.5.1 Future Work

The pathogen sensor presented here demonstrates feasibility to detect a range of antigens through simply swapping out the antibody in the immunoassay. Thus, other common wheat pathogens, or other crop pathogens, should be explored to build a multiplexed biosensor capable of quickly diagnosing the overall health of the crop. Next, we hope to test the biosensor developed here on live plant extracts collected from live samples infected with either the wheat spindle streak mosaic virus or the soil borne wheat mosaic virus to ensure that the product translates from the lab to a point-of-use application. Additionally, we hope to create a hand-held electronic platform capable of generating the input signal and extract the impedance response.

4.6 References

1. Enghiad, A., Ufer, D., Countryman, A. M. & Thilmany, D. D. An Overview of Global Wheat Market Fundamentals in an Era of Climate Concerns. *Int. J. Agron.* 2017, 1–15 (2017).
2. Wheat | Agricultural Marketing Resource Center. *Agricultural Marketing Resource Center* (2018). Available at: <https://www.agmrc.org/commodities-products/grains-oilseeds/wheat>. (Accessed: 22nd October 2018)
3. Day, L., Augustin, M. A., Batey, I. L. & Wrigley, C. W. Wheat-gluten uses and industry needs. *Trends Food Sci. Technol.* 17, 82–90 (2006).
4. Curtis, B. C., Rajaram, S. (Sanjaya) & Gómez Macpherson, H. *Bread: wheat : improvement and production: Wheat in the World*. (Food and Agriculture Organization of the United Nations, 2002).
5. Aldaya, M. M., Allan, J. A. & Hoekstra, A. Y. Strategic importance of green water in international crop trade. *Ecol. Econ.* 69, 887–894 (2010).
6. Pines, L. Wheat: Learn How To Trade It at Commodity.com. *Commodity.com* (2018). Available at: <https://commodity.com/soft-agricultural/wheat/>. (Accessed: 23rd October 2018)
7. Chalupníková, J., Kundu, J. K., Singh, K., Bartaková, P. & Beoni, E. Wheat streak mosaic virus: incidence in field crops, potential reservoir within grass species and uptake in winter wheat cultivars. *J. Integr. Agric.* 16, 523–531 (2017).
8. Thomas, J. . & Hein, G. . Influence of volunteer wheat plant condition on movement of the wheat curl mite, *Aceria tosichella*, in winter wheat. *Exp. Appl. Acarol.* 31, 253–268 (2003).
9. Hunger, R. M., Sherwood, J. L., Evans, C. K. & Montana, J. R. Plant disease : an international journal of applied plant pathology. *Plant Dis.* 76, 1056–1060 (1992).
10. Wiese, M. Wheat streak mosaic. *Compend. Wheat Dis.* 2, 80–81 (1987).
11. Erath, W. *et al.* Oligogenic control of resistance to soil-borne viruses SBCMV and WSSMV in rye (*Secale cereale* L.). *Plant Breed.* 135, 552–559 (2016).
12. Seifers, D. L., Martin, T. J., Harvey, T. L., Haber, S. & Haley, S. D. Temperature Sensitivity and Efficacy of *Wheat streak mosaic virus* Resistance Derived from CO960293 Wheat. *Plant Dis.* 90, 623–628 (2006).
13. Cadle-Davidson, L. & Gray, S. M. Soil-borne wheat mosaic virus. *Plant Heal. Instr.* (2006). doi:10.1094/PHI-I-2006-0424-01
14. Benbrook, C. M. Trends in glyphosate herbicide use in the United States and globally. *Environ. Sci. Eur.* 28, 3 (2016).
15. Price, J. A., Smith, J., Simmons, A., Fellers, J. & Rush, C. M. Multiplex real-time RT-PCR for detection of Wheat streak mosaic virus and Triticum mosaic virus. *J. Virol.*

- methods*. 165, 198–201 (2010).
16. Barfoot, P. & Brookes, G. GM Crops: The Global Economic and Environmental Impact - The First Nine Years 1996-2004. *J. Agrobiotechnology Manag. Econ.* 8, 187–196 (2005).
 17. Flachowsky, H., Hanke, M.-V., Peil, A., Strauss, S. H. & Fladung, M. A review on transgenic approaches to accelerate breeding of woody plants. *Plant Breed.* 128, 217–226 (2009).
 18. Jones, R. A. C., Coutts, B. A., Mackie, A. E. & Dwyer, G. I. Seed Transmission of *Wheat streak mosaic virus* Shown Unequivocally in Wheat. *Plant Dis.* 89, 1048–1050 (2005).

CHAPTER 5

ANTIBIOTICS SENSOR

5.1 Abstract

Antimicrobial use in livestock has emerged as pressing global issue due to the rise of antimicrobial-resistant bacteria. Regulatory authorities across the globe have taken steps to discourage the misuse of these antibiotics by banning or limiting the use of medically important antibiotics in food animals. However, to ensure food animals are not being administered antibiotics inappropriately there is a need for a reliable, rapid-response biosensor that can detect the presence of these antibiotic residuals in meat products. We have developed an affinity-based electrochemical biosensor for the label-free detection of ceftiofur residues in meat samples. The sensor uses a self-assembled immunoassay to target the ceftiofur biomarker employs electrochemical impedance spectroscopy to probe the interfacial capacitive changes as the ceftiofur binds to the sensor surface. We have demonstrated a platform that can detect ceftiofur at concentrations down to 0.01 ng/mL in 1x PBS and 10 ng/mL within ground turkey meat samples.

5.2 Introduction

Antimicrobials have played an essential role in the maintenance and care for livestock since the mid-twentieth century.^{1,2} Today, antimicrobials are used in animal husbandry for a range of applications from therapeutic use to promoting feed efficiency. When administered at appropriate levels these drugs exhibit bactericidal or antimicrobial effects by inhibiting the activity or growth of bacteria. However, when given at incorrect doses bacterial drug resistance may arise through either selection through random genetic mutation or by horizontal plasmid exchange across individual bacterium.^{2,3} Evidence suggests that misusing antimicrobials has contributed to the rise of antimicrobial-resistant bacteria (ARBs).⁴ Concern regarding the rise of ARBs has triggered an international response; the World Health Organization has made tackling ARBs a priority on their public health agenda and has released guidelines on the use of medically important antimicrobials in the food production industry.²

Certain antimicrobials, when administered at sub-therapeutic doses, improve feed conversion efficiency (i.e. produce more eggs, milk, or meat for a given amount of feed) through alterations in the gut flora.^{1,4} Growth promoting antimicrobials are administered through animal feed or water. This repeated, widespread use of antimicrobial growth promoters (AGPs) in poultry, swine, and beef cattle has been linked to the rise in local antimicrobial resistant bacterial populations.^{3,5} General dosing in the animal's food leads to only partial metabolism of the antimicrobials and is passed into the manure.¹ The manure then harbors an environment for ARBs proliferation and subsequent spread via run-off or percolation into rivers or water supplies.^{2,3}

The growing demand for animal protein in the developing world has led to farming facilities to vertically integrate their livestock production – where many animals are raised in close proximity and in poor sanitary conditions.⁶ Animals in these confined spaces are at high risk of catching and spreading illnesses, so antimicrobials are often used to curb the spread of disease. Many largescale animal feeding operations have turned to a 'shotgun' approach, administering a general antibiotic dosage to every animal within the population. Multi-drug resistant ARBs have emerged in these developing countries, posing a potential worldwide risk to human health.^{7,8} Furthermore, because the antimicrobials are not properly tuned to treat specific illnesses, a pool of resistance genes are readily available for ARB proliferation. In these developing countries, ARBs have been found not only in the treated animals, but also in their manure, local river water and crops, as well as the gut flora of farm employees and family members.^{1,9}

The key challenge is whether the use of antibiotics result in the development of hard to treat antibiotic resistant 'super bugs' that have significantly adverse impact on human health. The Consumer Union recently concluded that the threat to human health is real and potentially imminent, Humans are at a risk due to the potential presence of superbugs in meat and poultry. Hence there is a clear need for technological interventions that could enhance human awareness of the food products consumed. Human health can be affected by antibiotics directly through residuals found in meat or indirectly through the selection of antibiotic resistant strains of bacteria.^{5,10} Gassner & Wuethrich (1994) demonstrated that residuals of chloramphenicol (a drug developed to treat typhoid) metabolites in meat products were linked to aplastic anemia in

humans.¹¹ Perhaps more significantly, it was also believed that the over-use of chloramphenicol in animal feed may have led to drug resistance of the *Salmonella typhi*, the bacterium responsible for typhoid.¹¹

Selection of resistant strains may occur in pathogens that can directly infect humans. Resistance may also be selected for in bacteria that reside in animals which may be easily transmitted to humans (e.g. rabies, lymes disease, or salmonella). Consequences of infection from antibiotic resistant bacteria range from prolonged illness to death depending on severity of infection and treatment success rate.¹² Modern medicine has provided numerous antibiotic variants, but some bacterial strains like the multidrug-resistant *Staphylococcus aureus* or MDRSA are not easily treatable by any antibiotic developed since the 1940's.¹³

These multi-drug resistant bacteria have called for tighter regulations in the animal husbandry industry across the globe. The U.S. Food and Drug Administration, the European Union, and other regulatory bodies have taken strides to ensure the judicious use of medically important antimicrobial drugs in food-producing animals.¹⁴ These efforts are defined as maximizing therapeutic efficiency and minimizing selection of resistant microorganisms. China, which produces over half of the world's pork, is among a short list of countries that places no restrictions on AGP use.^{8,15} This high-volume use of antibiotics in these developing countries is believed to be one of the largest contributors to the increased environmental burden of ARGs.^{8,15}

Among the many different classes of antibiotics, ceftiofur is a third-generation cephalosporin labelled for veterinary use.^{12,15,16} Ceftiofur is often used to treat respiratory disease in swine, cattle, sheep and goats as well as early mortality infections in chickens and turkeys.¹⁷

Ceftriaxone – another third-generation cephalosporin – is critically important to human medicine as it is commonly used to treat bacterial infections in children. Cephalosporins all share the same mechanism of action,¹⁷ thus resistance of bacteria toward these antibiotics is a major concern among medical and veterinary experts.¹⁴ Studies have supported the notion that the use of ceftiofur in animal food products are a potential source of ceftriaxone-resistant salmonella infections in humans.^{16,18,19}

As more countries are pressured to adopt regulations limiting the use of antibiotics, the regulatory burden has grown when ensuring the judicious use of antibiotics. A low-cost, reliable, and easy-to-use biosensor that can detect antibiotics in animal food products would not only reduce this regulatory burden but could also appeal to consumers who wish to verify that their food is antibiotic free.

Current state of the art antibiotic detection is achieved through the principle of microbial inhibition. The Charm KIS™ test for example utilizes bacteria in agar with a pH indicator media.²⁰ When activated the bacteria generate acid and the pH indicator changes colors. In the presence of an antibiotic, the bacterial growth is inhibited, and the test does not change colors. While relatively easy to use, these tests are time consuming and do not provide quantitative results for regulatory enforcement purposes. Enzyme linked immunosorbent assay (ELISA) and high-performance liquid chromatography (HPLC) have shown promise as potential analytical methods for identifying antibiotic residues in food. These tools have demonstrated isolation and identification of various antibiotics in animal tissue samples. However large-scale and low-cost implementation of these systems remains a problem to be solved. ELISA often demonstrates good sensitivity and specificity, but it requires a relatively large volume of sample and must be ran on a benchtop plate-reader by a trained scientist to interpret the results. HPLC is relatively quick to perform the analysis, but uses large quantities of expensive organics, and is difficult to implement on a handheld device.

Affinity biosensors offer an attractive solution for scientists within the animal husbandry industry, as well as regulatory bodies and consumers for the detection of antibiotics in animal meat products. Affinity biosensors leverage biomarker detection through a recognition element that specifically targets the biomarker of interest. The chemical reaction between the target biomarker and the recognition element is then transduced to a measure signal output related to the concentration of the targeted biomarker. While some screening methods for detecting antibiotic residues exist,²¹ these tests are either based on microbial growth inhibition rather than detection of the analyte itself or chromatographic methods which are expensive and time-consuming. Efforts to incorporate nanomaterials in antibiotic biosensors have been emerging in

literature,²² however many of these biosensors either require labelling of the targeted antibiotic or have not demonstrated the ability to detect antibiotics in meat samples.

We have previously demonstrated many affinity-based biosensors using non-faradaic electrochemical impedance spectroscopy (EIS) to detect a range of biomarkers for various agricultural and human health and wellness applications.^{23,24} Here, we present an affinity-based biosensor that utilizes non-faradaic EIS to detect the presence of antibiotics in turkey and pork meat samples. A highly specific immunoassay is constructed on the sensor surface to encode specificity toward ceftiofur – the antibiotic of interest.

5.3 Experimental Section

5.3.1 Sensor Fabrication Process

The biosensor was fabricated on PET substrates using the e-beam deposition technique. Electrodes were deposited using electron beam physical vapor deposition at a pressure of $5 * 10^{-6}$ torr. The electrode patterns were deposited with 125 nm Au onto the precleaned PET substrate. A polydimethyl-siloxane (PDMS) confinement well was prepared to restrict the sample fluid in a controlled volume around the site of the three electrodes. To prepare the sensors for electrochemical measurements, the surface of the gold electrodes and the PET substrate were rinsed with 70% Isopropyl Alcohol (IPA), and distilled water (DI water) to remove organic residues. The electrodes were then dried with inert N₂ gas to prepare the surface for self-assembly of the immunoassay. Construction of an immunoassay first chemisorbs a linker molecule to the electrode surface then binds a capture antibody for subsequent detection of a dynamic range of the ceftiofur antigen. The linker molecule specific to our biosensor is the amine-reactive crosslinker dithiobis (succinimidyl propionate) (DSP). DSP has an *N*-hydroxysuccinimide (NHS) ester that is highly reactive with the primary amines which are abundant in antibodies and a cleavable disulfide bond in the molecule's spacer arm that interacts with the electrode surface via gold-thiol interaction. DSP forms highly ordered self-assembled monolayers (SAM)^{25,26} which immobilize the anti-ceftiofur (α -ceftiofur) capture antibody. High-affinity of the ceftiofur antigen toward the α -ceftiofur antibody allows for rapid binding interactions.

5.3.2 Electrochemical Evaluation of Biosensor Surface Modification via Electrochemical Impedance Spectroscopy

Electrochemical experiments were performed using a Gamry Reference 600 potentiostat. Non-faradaic electrical impedance spectroscopy (EIS) was used as a label-free approach to quantify impedance changes in the electric double layer capacitance. An input 10 mV sinusoidal voltage with a DC bias of -0.3 V vs. Ref was applied at the working electrode, and then scanned across a frequency range of 1 Hz – 1 MHz. The resultant current response was measured, and the complex impedance was calculated as the ratio of the input voltage to the output current. Ceftiofur doses were diluted in 1x Dulbecco's phosphate buffered saline (1x PBS) to obtain concentrations of 0.01 ng/mL – 10 ng/mL for either virus. A 'blank' sample (absent of the ceftiofur antigen) was tested after functionalization with the antibody to serve as a baseline measurement before administering subsequent doses.

After validating the electrochemical response to ceftiofur in a relatively low noise physiological buffer, the biosensor was then tested using turkey meat samples to characterize the feasibility as an antibiotic sensor for animal food products. The turkey meat used in this study was USDA verified antibiotic free to ensure that no ceftiofur residuals would be already present in the samples. 220 mg meat samples were first submerged in 300 μ L of 1x PBS (control), a 0.1 ng/mL ceftiofur dose, or a 10 ng/mL ceftiofur dose for 15 minutes to ensure uptake of the ceftiofur antigen. The samples were then placed on the sensor and tested for affinity binding of the ceftiofur biomarker to the immunoassay.

5.4 Results and Discussion

5.4.1 Characterization of Electrode Surface Modifications by Fourier-Transform Infrared Spectroscopy (FTIR) Analysis

Chemisorption of the DSP cross-linker and anti-ceftiofur antibody on the gold electrode surface was validated using FTIR. Gold thin films were deposited on PET substrates using e-beam vapor deposition at parameters mimicking those used for sensor fabrication and used for FTIR analysis. Functionalization of the electrode surface was carried out as described in the previous section. Prior to FTIR measurements, each sample was rinsed thoroughly with DI water then dried with N₂ air to rid the surface of any unbound material that may interfere with the analysis. The infrared spectra of surface modified samples were recorded with a Nicolet iS50 FTIR spectrometer.

Absorbance spectral measurements were obtained with a scan resolution of 4 cm^{-1} for 64 scans in the spectral range of 4000 cm^{-1} to 600 cm^{-1} . Absorption spectra was recorded for PET-gold surface conjugated to DSP molecules, and the gold surface with anti-ceftiofur antibodies linked via the DSP linker molecules.

The absorbance peaks observed in the DSP spectrum of Figure 5.1 at 1799 cm^{-1} and 1724 cm^{-1} indicate the symmetric and asymmetric carbonyl stretches (respectively) of the NHS ester. Furthermore, the peak at 1251 cm^{-1} confirm the presence of the asymmetric C-N-C stretch of the NHS ester while the peak at 1112 cm^{-1} can be identified as the succinimide N-C-O stretch. Finally, the peak at 1822 cm^{-1} indicates the ester carbonyl stretch. The presence of these peaks is characteristic of a self-assembled monolayer of DSP, confirming the chemisorption of DSP to the gold surface.

The reaction between the NHS group with the antibody's primary amine group can be noted in the anti-ceftiofur spectrum. The C-O bonds of the NHS ester are broken and react with primary amines of the antibody, resulting in a stable amide bond. A suppression of peaks associated with the NHS ester (1799 cm^{-1} , 1724 cm^{-1} , 1251 cm^{-1}) is observed, while peaks at $\sim 1644\text{ cm}^{-1}$ and $\sim 1552\text{ cm}^{-1}$ are indicative of amide I and amide II peaks. These results show a stable formation of the immunoassay through the binding of the anti-ceftiofur antibodies to the DSP functionalized surface.

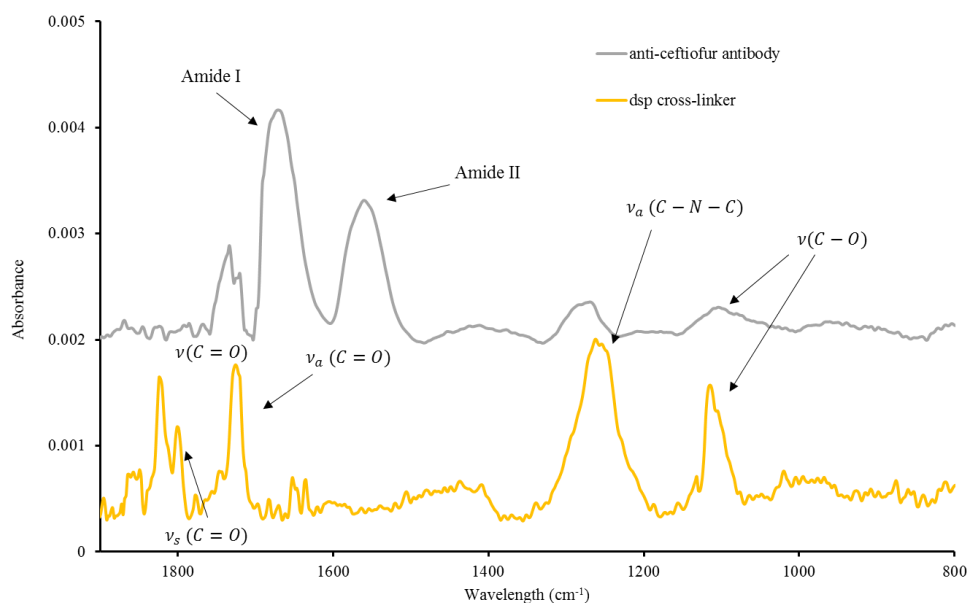


Figure 5.1. FTIR spectra of (a) DSP crosslinker immobilized on Au surface, (b) anti-ceftiofur antibody conjugated to DSP cross-linker.

5.4.2 Electrochemical Evaluation of Biosensor Surface Modification via Electrochemical Impedance Spectroscopy

The electrochemical response was evaluated at each step of the immunoassay through EIS measurements. The bulk and interfacial phenomena were visualized using Nyquist impedance plots (Figure 5.2a), and values of the impedance modulus (Z^*) were extracted at 10 Hz to highlight the impedance changes as the immunoassay was chemisorbed onto the sensor surface as seen in Figure 2b. A 1x PBS measurement was performed prior to any surface modifications to evaluate the baseline EDL properties at the electrode-electrolyte interface. In the absence of any surface modifications, the 1x PBS measurement exhibits a compressed semicircle in the Nyquist impedance plot, indicating a resistance-dominated system where hydrolysis and/or gold oxidation is occurring as charges leak across the electrode-electrolyte interface due to the applied DC bias. After subsequent binding of the DSP linker, a second 1x PBS measurement was taken to examine how the DSP monolayer impacts interfacial properties. When the DSP linker self-assembles an insulative layer forms at the interface, both reducing the propensity for charge transfer across this interface and increasing the charge separation between the solvent ions and the electrode surface.

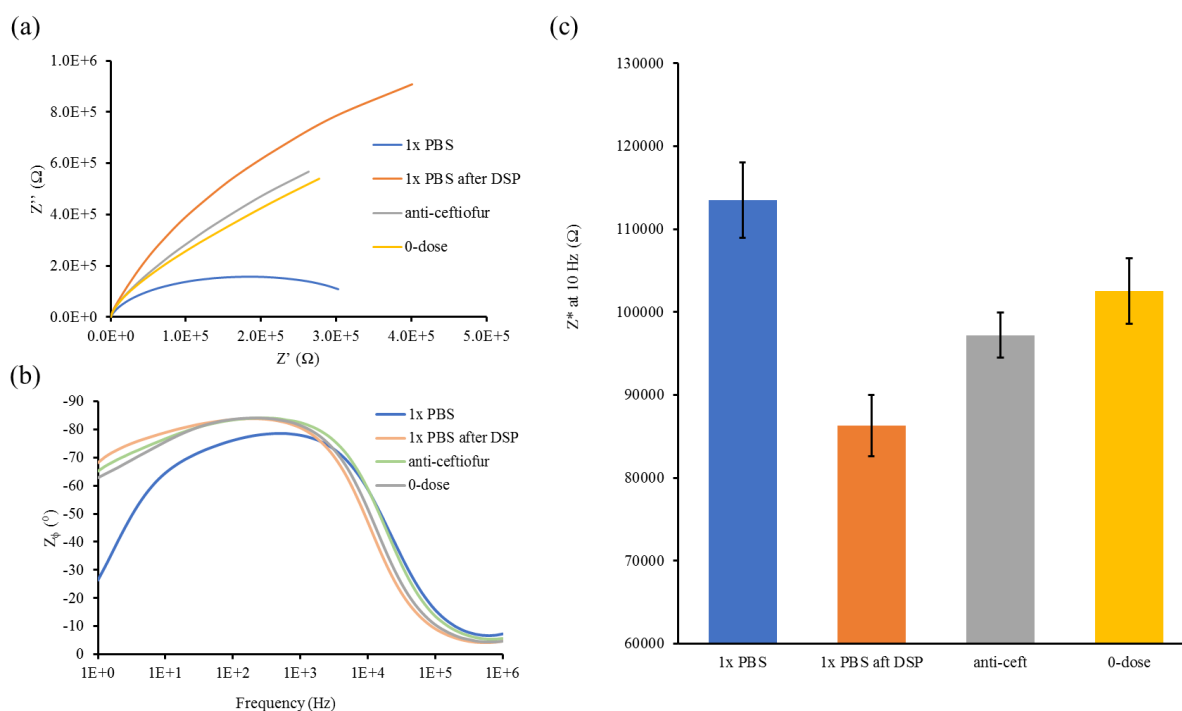


Figure 5.2. (a) Nyquist impedance plot (b) Bode Phase plot and (c) extracted Z^* values at 10 Hz for EIS measurements to validate the chemisorption of the immunoassay.

When extracting the impedance at 10 Hz (Figure 5.2c), the Z^* drops from 113,528 Ω to 86,295 Ω after binding DSP to the gold electrode surface. The impedance drop is driven both by changes in both the real and imaginary impedance response. The decrease in charge transfer across the interface is observed as a large reduction in Z' , a small increase in Z'' , and an increase in the semi-circle diameter of Figure 5.2a. Binding of the DSP molecules also creates a separation of charges leads to a reduction in the EDL capacitance (hence the increase in Z''), shifting the low frequency phase response toward -90° as seen in the Bode phase diagram in Figure 5.2b.

After the DSP modified the surface, the addition of the antibody introduces excess charges at the electrode interface, resulting in a small increase in Z' as well as the phase. This increase is reflected in the overall impedance as the Z^* value at the antibody step was 97,208 Ω. A third 1x PBS measurement (0-dose) was taken to validate the antibodies remain bound to the electrode surface. While there was a slight increase in the Z^* value (to 10,2537 Ω) there was no significant change observed between the antibody and the subsequent PBS, indicating that the NHS esters on the DSP

molecule have reacted with the primary amines on the anti-ceftiofur antibody, anchoring them to the electrode surface.

5.4.3 Analysis of Dose-Dependent Response via Electrochemical Impedance Spectroscopy in 1x PBS

The third 1x PBS measurement after the antibody also serves as a ‘blank’ for subsequent ceftiofur dose steps. Doses of ceftiofur were prepared in 1x PBS from 0.1 ng/mL to 10 ng/mL and the resulting Nyquist capacitance plots are shown below in Figure 5.3:

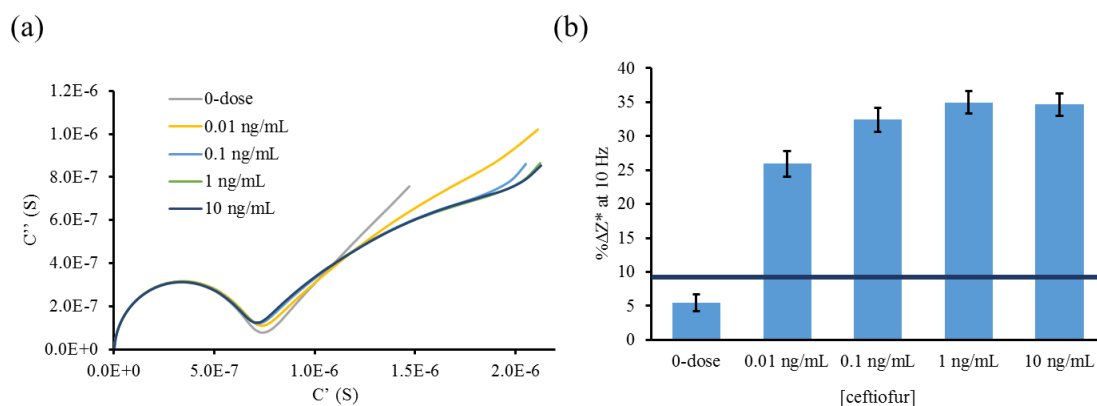


Figure 5.3. Calibrated dose response across varying concentrations of ceftiofur represented as (a) Nyquist capacitance plot and (b) percent change in impedance with respect to the antibody measurement at 10 Hz with SST in dark blue (n=4).

The measured concentration range was selected as it spans the typical concentrations measured in commercially available ceftiofur ELISA kits. As ceftiofur molecules bind to the immunoassay, the dielectric permittivity of the EDL is modulated. Changes in impedance spectra due to biomarker binding are not always resolvable depending on the nature of the support matrix and the biomarker of interest. To address the poor resolution between ceftiofur concentrations, the impedance data is transformed into a complex capacitance which highlights the storage characteristics occurring at the interface rather than resistive terms which are emphasized in EIS. A complex capacitance plot is shown in Figure 5.3a with the imaginary capacitance (C'') on the y-axis and the real capacitance (C') on the x-axis. Here, a semicircle is observed for every dose of ceftiofur with a diameter of $\sim 7.5E-6$ S, corresponding to the primary relaxation constant of the immunoassay.

A second, concentration-dependent semicircle manifests at lower frequencies with higher doses of the ceftiofur biomarker. This second semicircle appears due to a second relaxation process in response to the applied potential. The polar structure of the ceftiofur molecule likely introduces additional degrees of freedom when binding to the adsorbed immunoassay. However further investigation into the immunoassay structure would need to be investigated before validating this claim. The percent change in impedance at 10 Hz was calculated change for each concentration of ceftiofur with respect to the antibody measurement and plotted vs ceftiofur concentration between 0.01 ng/mL and 100 ng/mL with the initial “0-dose” corresponding to a measurement in 1x PBS without any ceftiofur antigens.

When the ceftiofur molecule binds to the immunoassay, a second dipolar relaxation process emerges, raising the capacitance thus decreasing the impedance response. For ceftiofur spiked in PBS, the impedance response varies with a dynamic range between 75967 Ω (0.01 ng/mL) and 67020 Ω (100 ng/mL) corresponding to a 26% to a 34% change with respect to a blank solution. A signal-to-noise ratio of 3 was selected to calculate the specific signal threshold (SST) impedance as indicated in the following equation:

$$SST = \mu_{blank} + 3 * SD_{blank} \quad (4.2)$$

The Limit of Detection (LOD) is identified as the lowest concentration of ceftiofur which can be reliably and feasibly detected from a ‘blank’ solution. The LOD can be calculated by using the mean and standard deviation for a the 1x PBS measurement after binding the antibody:

$$LOD = [ceftiofur]_{low} \quad when \quad (\mu_{[ceftiofur]} - SEM_{[ceftiofur]}) > SST \quad (4.3)$$

The LOD was found by subtracting the SEM for each concentration of the ceftiofur ($SEM_{[ceftiofur]}$) from the mean $\mu_{[ceftiofur]}$. This value was then compared to the SST for each concentration of the ceftiofur, and the lowest concentration that exhibited a value larger than the SST was determined as the LOD. Concentrations at and above the LOD show significant impedance responses indicating the ceftiofur is reliably detectable. Using Equation 4.3, the LOD for ceftiofur was 0.01 ng/mL in 1x PBS.

5.4.4 Analysis of Dose-Dependent Response via Electrochemical Impedance Spectroscopy in Turkey Meat Samples

Translating from 1x PBS to the turkey meat enhanced the resolution of bulk capacitive response as indicated by the Nyquist impedance plots shown in Figure 5.4a. This is likely because the turkey samples exhibited a more resistive response, implying a lower effective ionic content, thus enhancing the effect of interfacial bulk capacitance. To remove the bulk electrochemical effects and focus on affinity binding at the interface the imaginary impedance (Z'') was isolated and analyzed at the low-frequency spectrum to determine dose-dependent changes as seen in Figure 5.4b.

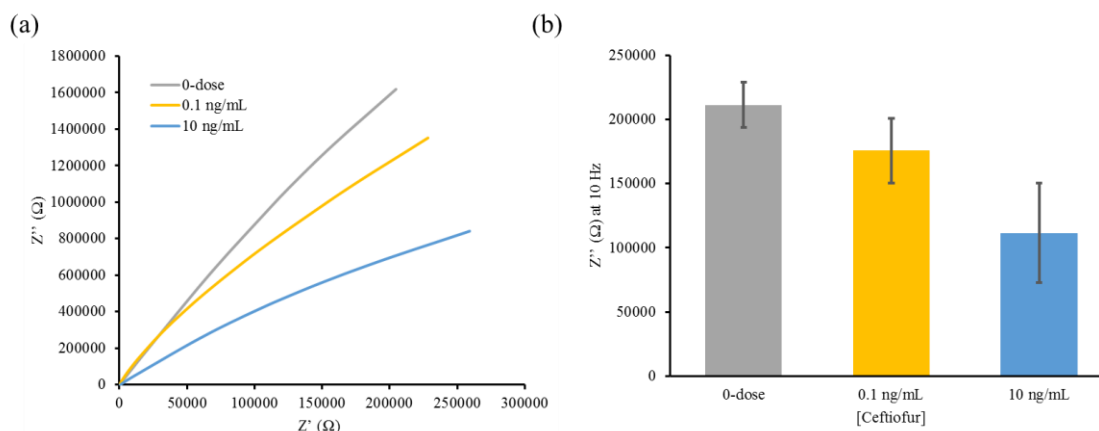


Figure 5.4. Calibrated dose response across varying concentrations of ceftiofur in turkey meat samples represented as (a) Nyquist impedance plot and (b) Z'' at 10 Hz ($n=3$).

The turkey samples act as a porous solid retaining the electrolyte within the meat. The addition of these porous boundaries interferes with the distance for the ions to travel in the bulk of the solution and is seen as an increase in the high frequency solution resistance. The low-frequency response of the sample is less impacted by the meat sample as it measures interfacial properties and does not probe into the bulk of the solution. At the low frequency range, it is evident that as larger concentrations of ceftiofur are added to the meat samples, a decrease in Z'' is observed. This decrease is caused again by the binding of electrically charged ceftiofur molecules modulating the dielectric permittivity within the EDL. The LOD was again found for the ceftiofur doses in turkey meat. Here the SST was found to be 159050.3 Ω using equation 4.4:

$$SST = \mu_{blank} - 2 * SD_{blank} \quad (4.2)$$

making the 10 ng/mL dose the only dose reliably distinguishable from the blank solution. It can be concluded that the sensor performance is effective at detecting ultra-low concentrations of ceftiofur within meat samples and the flexible sensor prototype would greatly reduce the time and financial burden to test meat samples for the presence of antibiotic residues.

5.5 Conclusions

Antibiotic detecting in meat samples has tremendous importance in the livestock and consumer marketplace. As new strains of antibiotic resistant bacteria continue to emerge, regulatory authorities like the FDA and USDA will continue to place more restrictions on the use of medically important antibiotics in food animals. These restrictions place a larger financial and time burden on livestock farmers to comply with appropriate dosing of antibiotics and regulators to ensure compliance. To prevent these operations from being too costly or time consuming, a faster, cheaper method of antibiotic detection is needed.

This paper proposes a low-cost, proof-of-concept biosensor for the detection of antibiotic residuals. Based on our review of literature in the public domain, this is the first impedimetric biosensor for the detection of antibiotics in meat samples. The biosensor demonstrates high sensitivity ($LOD = 0.01 \text{ ng/mL}$) in a physiological buffer, without the use of any external labels or redox reagents. Monitoring both changes in EDL capacitance (through Nyquist impedance plots) and SAM dielectric capacitance (through Nyquist capacitance plots), allows for the detection medium to be readily swapped for other more complex samples like turkey meat. In the turkey meat samples, the sensor demonstrates a decreasing trend in the Z'' response at 10 Hz at concentrations of ceftiofur well below the current standard detection thresholds. Additionally, the sensor was still able to capture dose-dependent changes within the meat samples with good sensitivity ($LOD = 10 \text{ ng/mL}$). The higher limit of detection was due to the complex nature of the meat sample matrix. The porous nature of the meat interferes with the non-Faradaic current conduction, and physical contact of the meat sample onto the sensor surface may also impede access to the self-assembled immunoassay. However, this is – to our knowledge – the first

demonstration of a label-free, electrochemical biosensor for the detection of any antibiotic material.

5.5.1 Future Work

This paper demonstrates strong feasibility toward a rapid, versatile antibiotic biosensor. An easy to use biosensor that can detect the presence antibiotic material directly in the meat samples would allow regulatory authorities, livestock farmers, and everyday consumers to better monitor the quality of their meat. As antibodies can be produced for nearly any target antigen, it is feasible that this platform can be modulated to detect other antibiotics across a range of meat samples. Additionally, to increase the resolution for detection in meat samples, additional surface modifications may be necessary to create a physical barrier between the meat sample and the immunoassay constructed on the sensor surface (e.g. hydrogel deposition or another physical polymer barrier). The barrier would prevent physical interaction between the meat sample and the immunoassay, likely leading to better stability and sensitivity.

5.6 References

1. Marshall, B. M. & Levy, S. B. Food animals and antimicrobials: impacts on human health. *Clin. Microbiol. Rev.* 24, 718–733 (2011).
2. Holmes, A. H., Holmes, M., Gottlieb, T., Price, L. B. & Sundsfjord, A. End non-essential use of antimicrobials in livestock. (2018).
3. You, Y. & Silbergeld, E. K. Learning from agriculture: understanding low-dose antimicrobials as drivers of resistome expansion. *Front. Microbiol.* 5, 284 (2014).
4. Van Boeckel, T. P. *et al.* Global trends in antimicrobial use in food animals. *Proc. Natl. Acad. Sci.* 112, 5649–5654 (2015).
5. Hughes, P. & Heritage, J. Antibiotic growth-promoters in food animals. *FAO Anim. Prod. Heal. Pap.* 129–152 (2004).
6. Tilman, D., Balzer, C., Hill, J. & Befort, B. L. Global food demand and the sustainable intensification of agriculture. *Proc. Natl. Acad. Sci.* 108, 20260–20264 (2011).
7. Silva, N. C. C. *et al.* Molecular characterization and clonal diversity of methicillin-susceptible *Staphylococcus aureus* in milk of cows with mastitis in Brazil. *J. Dairy Sci.* 96, 6856–6862 (2013).
8. Zhu, Y.-G. *et al.* Diverse and abundant antibiotic resistance genes in Chinese swine farms. *Proc. Natl. Acad. Sci.* 201222743 (2013).
9. Osterberg, D. & Wallinga, D. Addressing externalities from swine production to reduce public health and environmental impacts. *Am. J. Public Health* 94, 1703–1708 (2004).
10. Massé, D. I., Saady, N. M. C. & Gilbert, Y. Potential of biological processes to eliminate antibiotics in livestock manure: an overview. *Animals* 4, 146–163 (2014).
11. Gassner, B. & Wuethrich, A. Pharmacokinetic and toxicological aspects of the medication of beef-type calves with an oral formulation of chloramphenicol palmitate. *J. Vet. Pharmacol. Ther.* 17, 279–283 (1994).
12. White, D. G. *et al.* The isolation of antibiotic-resistant *Salmonella* from retail ground meats. *N. Engl. J. Med.* 345, 1147–1154 (2001).
13. Hiramatsu, K. *et al.* Multi-drug-resistant *Staphylococcus aureus* and future chemotherapy. *J. Infect. Chemother.* 20, 593–601 (2014).
14. Organization, W. H. The Medical impact of the use of antimicrobials in food animals: report of a WHO meeting, Berlin, Germany, 13-17 October 1997. (1997).
15. Maron, D. F., Smith, T. J. S. & Nachman, K. E. Restrictions on antimicrobial use in food animal production: an international regulatory and economic survey. *Global. Health* 9, 48 (2013).
16. Fey, P. D. *et al.* Ceftriaxone-resistant *Salmonella* infection acquired by a child from cattle. *N. Engl. J. Med.* 342, 1242–1249 (2000).

17. Hornish, R. E. & Katariski, S. F. Cephalosporins in veterinary medicine-ceftiofur use in food animals. *Curr. Top. Med. Chem.* 2, 717–731 (2002).
18. Dunne, E. F. *et al.* Emergence of domestically acquired ceftriaxone-resistant *Salmonella* infections associated with AmpC β -lactamase. *Jama* 284, 3151–3156 (2000).
19. Winokur, P. L. *et al.* Animal and human multidrug-resistant, cephalosporin-resistant *Salmonella* isolates expressing a plasmid-mediated CMY-2 AmpC β -lactamase. *Antimicrob. Agents Chemother.* 44, 2777–2783 (2000).
20. Schneider, M. J. & Lehotay, S. J. A comparison of the FAST, Premi® and KIS™ tests for screening antibiotic residues in beef kidney juice and serum. *Anal. Bioanal. Chem.* 390, 1775–1779 (2008).
21. Virolainen, N. & Karp, M. in *Bioluminescence: Fundamentals and Applications in Biotechnology-Volume 2* 153–185 (Springer, 2014).
22. Lan, L., Yao, Y., Ping, J. & Ying, Y. Recent advances in nanomaterial-based biosensors for antibiotics detection. *Biosens. Bioelectron.* 91, 504–514 (2017).
23. Lisdat, F. & Schäfer, D. The use of electrochemical impedance spectroscopy for biosensing. *Anal. Bioanal. Chem.* 391, 1555 (2008).
24. Wang, J. Electrochemical biosensors: towards point-of-care cancer diagnostics. *Biosens. Bioelectron.* 21, 1887–1892 (2006).
25. Vericat, C., Vela, M. E., Benitez, G., Carro, P. & Salvarezza, R. C. Self-assembled monolayers of thiols and dithiols on gold: new challenges for a well-known system. *Chem. Soc. Rev.* 39, 1805–1834 (2010).
26. Rudzinski, W. E. & Francis, K. Evaluating the surface density and heterogeneity of a dithiobis (succinimidylpropionate) self-assembled monolayer on gold and its coupling with DNA embedded within a matrix. *Appl. Surf. Sci.* 256, 5399–5405 (2010).

CHAPTER 6

THC SENSOR

6.1 Abstract

Marijuana is listed as a Schedule I substance under the American Controlled Substances Act of 1970. As more U.S. states and countries beyond the U.S. seek legalization, demands grow for identifying individuals driving under the influence (DUI) of marijuana. Currently no roadside DUI test exists for THC, the primary psychoactive in marijuana. Urine tests are commonly performed but are limited to detecting THC metabolites, which only appear beyond the window of intoxication. Here, we propose a novel, rapid, electrochemical biosensor for the detection of THC in saliva down to, and beyond, the established 4 ng/mL cut-off limit for roadside DUI tests. The biosensor integrates with a portable saliva swab for rapid identification of THC in saliva samples.

6.2 Introduction

Marijuana is commonly used as a recreational drug due to its stimulant and euphoric effects. Tetrahydrocannabinol (THC) is the primary psychoactive compound in marijuana, which acts on the endocannabinoid system within the central nervous system.^{1,2} Its agonism on the cannabinoid receptors alters the concentrations of various neurotransmitters (e.g. dopamine and norepinephrine) which are closely associated with THC's effect on mood and conscious perception.² Effects of consuming marijuana include but are not limited to: euphoria, stress reduction, increased humor and music appreciation, metacognition, and creativity.³ Anxiety and or panic attacks are the most common side effects of smoking marijuana when consumed at doses exceeding the psychotropic threshold.⁴ When smoking marijuana, these effects can wholly manifest within a few minutes and last 1-3 hours.⁴ Whereas oral consumption of marijuana drastically prolongs the time for effects to arise and subsequently diminish due to the slower adsorption through the gut.⁴ THC is a lipophilic molecule and will bind nonspecifically to other fat-containing body parts such as adipose tissue.³ Because it can store in fat tissue, THC yield a longer elimination half-life (EHL) relative to other recreational drugs. Furthermore, the EHL is also dependent on metabolism, and quantity/frequency of use. In fact, the redistribution of THC from tissue to blood is the rate-limiting step in its metabolic pathway.³

Aside from the mind-altering effects of marijuana, there are potential health benefits of the drug as well.⁵ Quality evidence supports that marijuana and its derivatives can be used to treat chronic and neuropathic pain, spasticity due to multiple sclerosis, nausea and vomiting associated with cancer chemotherapy, and lack of appetite in HIV or cancer patients.⁶ In June 2018 the first marijuana-based drug, Epidiolex, was approved by the FDA for the first time, however marijuana remains a Schedule I substance which is defined as having “no currently accepted medical use and a high potential for abuse.”⁷

There is evidence that suggests long-term use of marijuana may lead to addiction in approximately 9% of those who use marijuana.^{8,9} Certain groups are at an elevated risk for addiction; those who start using marijuana as teenagers have a 1 in 6 chance of developing marijuana dependency and daily user dependency rates are between 25 to 50%.⁸ Furthermore, early and regular use of marijuana shows an increased risk of addiction and the use of other illicit drugs.⁸ The *Diagnostic and Statistical Manual of Mental Disorders*, 4th edition (DSM-IV) demonstrates that of the 5.1 million people that meet the criteria for dependency on any illicit drug, over half of these cases are due to marijuana.⁹ In addition to risks of addiction, consumption of marijuana can impair neural connectivity and lead to learning and memory loss, diminished alertness and self-awareness, as well as degradation of habit and routine management.¹⁰ These effects on development and memory are often topics within debates regarding the repeal marijuana prohibition in the US, citing child addiction rates and vehicular crash risks as the primary argument against its repeal.

Marijuana is among the most commonly detected drugs in random roadside screenings.¹¹ Increased blood THC concentrations and recent smoking (within 2 hours) are strongly associated with higher crash and culpability risks.¹² These risks arise because THC interferes with visual and auditory perception as well as key psychomotor abilities.⁴ A 2012 review of marijuana consumption found that driving under the influence of marijuana correlates to nearly a 2x increased risk of motor vehicle collisions, especially in fatal collisions.¹³ Another study found that marijuana was among the most frequently detected drug among motor vehicle crash victims admitted to regional Level-I trauma centers within the US.¹⁴ Onsite, roadside testing for THC is routinely performed in urine despite urine being a poor indicator of recent marijuana use. Instead, there is a push for law

enforcement to utilize tests using saliva as the detection medium, as the salivary THC profile closely correlate to levels in blood.¹¹

Urine and blood are the most common matrices used to test for marijuana use. However, saliva, sweat, and hair have also been explored for alternative, less invasive tests.¹⁵ The window of detection and cut-off limit for each of these matrices vary significantly. THC can be detected in blood for up to 5 hours with a cutoff limit of 10 ng/mL, in urine for up to 95 days with a cutoff limit of 15 ng/mL, and in saliva for up to 34 hours with a 0.5 ng/mL limit.^{16,17} However, these values are based on only a few seminal studies as approval for testing illicit products like marijuana are difficult to get approval for. The lack of reliable tests and cut-off limits for intoxication are common topics amongst debates to repeal marijuana prohibition. Furthermore, variable EHL and metabolism make setting cutoff concentrations for urine tests more difficult as the window of detection can vary drastically from subject to subject.¹⁸ These large detection windows may be beneficial in the workplace where a zero-tolerance policy is in effect, but for roadside DUI testing a detection window should correlate closely to intoxication levels.

It is generally accepted that the presence of THC in oral fluid is an indicator of recent cannabis use.¹⁹ When smoking marijuana, THC is deposited in the oral cavity through direct contact with oral mucosa; reuptake into saliva from blood also occurs but its effects are minimal.¹⁹ Additionally, THC appears immediately within blood after the first inhalation and peaks within 8 minutes.¹⁶ Despite that salivary THC levels have only an insignificant contribution directly from THC in blood, the time course in these two biological fluids follow very similar concentration profiles.¹⁹ This finding suggests that saliva is a good indicator for active drug use.

Other reports of electrochemical detection of THC in saliva samples have been reported.^{20,21} However, this is the first biosensor that, to our knowledge, utilizes affinity-based detection through impedimetric measurements. Here, we present an affinity-based biosensor that utilizes non-faradaic EIS to detect the presence of a BSA-THC hapten in human saliva samples. Affinity biosensors leverage biomarker detection through a recognition element that specifically targets the biomarker of interest. The chemical reaction between the target biomarker and the recognition element is then transduced to a measure signal output related to the concentration of the targeted

biomarker. Affinity biosensors toward THC already exist as home-kit lateral¹¹ flow assays, however to maintain an accurate reading these tests require: highly precise sample volumes, careful reagent handling by the user, and often relatively long wait times to results.¹¹ The electrochemical biosensor presented here could streamline the testing process, eliminate the need for any sample preparation and reduce the wait-time as the sensor does not rely on slow diffusion-limited processes.

6.3 Materials & Methods

6.3.1 Sensor Fabrication Process

The biosensor was fabricated on PET substrates using the e-beam deposition technique. Electrodes were deposited using electron beam physical vapor deposition at a pressure of $5 * 10^{-6}$ torr. The electrode patterns were deposited with 125 nm Au onto the precleaned PET substrate. After fabrication, the surface of the gold electrodes and the PET substrate were rinsed with 70% Isopropyl Alcohol (IPA), and distilled water (DI water) to remove organic residues. The electrodes were then dried with inert N₂ gas to prepare the surface for self-assembly of the immunoassay. Construction of an immunoassay first chemisorbs a linker molecule to the electrode surface then binds a capture antibody for subsequent detection of a dynamic range of the THC-BSA hapten. The linker molecule specific to our biosensor is the amine-reactive crosslinker dithiobis (succinimidyl propionate) (DSP). DSP has an *N*-hydroxysuccinimide (NHS) ester that is highly reactive with the primary amines which are abundant in antibodies and a cleavable disulfide bond in the molecule's spacer arm that interacts with the electrode surface via gold-thiol interaction.²² DSP forms highly ordered self-assembled monolayers (SAM)²³ which immobilize the anti-THC capture antibodies. The THC-BSA hapten possess high affinity toward the anti-THC antibody allowing for rapid binding interactions.

6.3.2 Zeta Potential Evaluation as a Function of pH for the THC-BSA Hapten

A Malvern ZetaSizer Nano ZS was used to determine the zeta potential of the THC-BSA hapten as a function of pH. Samples of 0.05 g/L THC-BSA were prepared in 0.001 M KCl after titrating to varying pH by adding either 0.1M HCl or 0.1M NaOH. Samples were loaded into the folded capillary cell using a diffusion barrier technique as described in literature provided by Malvern. First, 700 μ L of the 0.001M KCl was loaded into the DTS1070 capillary tube, then 100 μ L of 0.05

g/L THC-BSA at matching pH was added to the bottom of the capillary cell using a gel-loading pipette. This diffusion barrier suspends the sample at the bottom of the cuvette, separating the THC-BSA hapten from the electrode protecting the molecule from damage by contact with the electrode. The zeta potential was measured using the electrophoretic mobility technique, which measures the velocity of the particles under the influence of an electric field, and then calculates zeta potential via the Smoluchowski equation given in Equation 5.1:

$$\mu = \frac{\epsilon\zeta}{\eta} \quad (5.1)$$

where μ represents the electrophoretic mobility, ϵ is the dielectric constant of the KCl dispersant, ζ is the zeta potential, and η is the viscosity of KCl dispersant (measured using a viscometer).

6.3.3 Evaluation of Dose-Dependent Response via Electrochemical Impedance Spectroscopy

Electrochemical Impedance Spectroscopy (EIS) was employed as rapid, label-free approach to study the affinity-based detection of the THC-BSA hapten. The binding of the THC-BSA hapten to the anti-THC antibody conjugated to the sensor surface was analyzed by non-faradaic changes in the dielectric properties at the electrode-electrolyte interface. A Gamry Reference 600 potentiostat was used to measure the EIS response. An input 10 mV sinusoidal voltage with a DC bias of -0.3 V vs. Ref was applied at the working electrode, and then scanned across a frequency range of 1 Hz – 1 MHz. The resultant current response was measured, and the complex impedance was calculated as the ratio of the input voltage to the output current.

EIS experiments were carried out first by diluting the THC-BSA hapten in 1x PBS to obtain concentrations between 0.1 ng/mL to 10 g/mL to establish the baseline electrochemical interaction of the THC-BSA hapten with the electrode. After establishing the response in 1x PBS, the THC-BSA hapten was diluted in synthetic saliva at pH 4 and pH 6 to determine how pH affects the sensor's dynamic response. Finally, the hapten was spiked into human saliva samples collected at concentrations between 0.1 ng/mL and 100 ng/mL.

6.3.4 Optimal Operating Frequency Selection for Electrochemical Impedance Spectroscopy Experiments

When interpreting non-faradaic EIS data, many researchers self-select the frequency range for their analysis based on assumptions about the chemical processes dominant at these frequencies.²⁴ This

decision is largely dependent on the resistive and capacitive nature of the electrode, electrolyte, and biomarker of interest. Thus, some initial knowledge of the system characteristics should be understood before attempting to extract information. Researchers typically identify the optimal frequency for sensor operation by finding the frequency with a maximal signal-to-noise ratio (SNR) between their test samples and control (no analytes present).²⁴ This optimal frequency is selected where either capacitive or resistive effects are dominant. Thus, biasing their analysis to one aspect of the electrochemical response and ignoring the remainder of the spectrum. While this is a widely accepted practice, the presence of the analyte may alter low frequency double layer capacitance (or charge transfer resistance) and high frequency solution resistance simultaneously.

Feature selection techniques can be classified as filters, wrappers, or embedded techniques. Filter methods score the input features (here impedance measurements at different frequencies) by some statistical measure regarding the dependent variable. The scoring criterion is used to rank then eliminate features that are below a certain threshold. Filtering removes features before classification based on a measure of each features' usefulness in discriminating the different classes. This paper does not explore wrapper or embedded techniques as these methods are computationally expensive with a very large feature space.

A method of down-selecting the optimal frequencies is employed through a systematic, unbiased approach of feature selection methods developed for reducing data dimensionality. A Fast Correlation Based Filter (FCBF)^{25,26} was used to identify which combination of features contain the maximum discrimination information about the output. Using FCBF, features are deemed irrelevant only if they are conditionally independent of the different classes to predict on. FCBS has been demonstrated to improve learning algorithm speed and accuracy over other commonly employed filter methods. By removing irrelevant or highly correlated frequencies from the spectrum noise and redundancy are reduced which improves the generalization of the algorithm's prediction power on new datasets. Additionally, by removing unwanted data, the algorithm's learning rate is dramatically improved, allowing for faster training and deployment.^{25,26} FCBF was employed to remove features that that are poor predictors of the output class or highly correlated to 'better' input features. The goal of the FCBF algorithm was to identify a single best feature to pull from 1) the raw impedance dataset, 2) the dataset normalized to the antibody, and 3) the dataset

normalized to the synthetic saliva, while ensuring that each of these three features are not correlated to one-another.

6.3.5 Binary Classification of *THC* +/- Human Saliva Samples

Binary classification is the process of classifying a given set of inputs into two distinct groups based on some classification rule(s). Here two binary classification algorithms: Logistic Regression and a Support Vector Machine (SVM) were tasked with separating the *THC* + inputs from the *THC* – inputs. The resulting models were evaluated in terms of classification performance characteristics. The percentage of *THC* + samples that were correctly identified were calculated as the True Positive Rate (TPR), while the percentage of *THC* + samples that were incorrectly classified referred to the False Positive Rate (FPR).

Receiver Operating Characteristic (ROC) curves were plotted with TPR, or sensitivity, on the y-axis and FPR on the x-axis.²⁷ The AUC provides the aggregate performance for the model's classification ability by exploring all possible threshold parameters. Because the AUC is classification-threshold-invariant, it indicates the quality of the classifier by examining the overall separability between the two classes.²⁷

To evaluate the prediction power of each model on unseen data points, a test set is randomly sampled from the dataset to hold out during the training phase. Because both the training and test sets are from the same overall population, this train-test split provides a less biased evaluation of the model's fit on the training dataset. However, the random sampling of the test set does not guarantee a perfect fit, so often cross-validation methods are used to better evaluate the bias on the trained model. K-folds cross-validation sequentially selects one bin as the validation set and the remaining 9 bins as the training set. This cross-validation process is repeated 10 times using each bin exactly once as the validation dataset. This allows all observations to be used for both training and validating the model. The 10 validation set performances are averaged across each iteration to produce a single estimation. K-folds cross-validation generalizes the model's prediction performance by penalizing solutions that exhibit overfitting or high selection bias.^{28,29}

Logistic Regression utilizes a binomial variant of the generalized linear model as the hypothesis function to make predictions on:

$$h_{\theta}(x) = g(\theta^T x) = \ln\left(\frac{1}{1+e^{-\theta^T x}}\right) \quad (6.1)$$

Where $g(\theta^T x)$ is the sigmoid function applied to inputs x parameterized by θ . Logistic Regression is commonly used to describe dichotomous data with an S-shaped distribution function. The model predicts the probability (bounded between 0 & 1) that the output belongs to either class given the inputs and model parameters:

$$h_{\theta}(x) = P(y = 1|x; \theta) = 1 - P(y = 0|x, \theta) \quad (6.2)$$

To determine the appropriate parameters for Logistic Regression a cost function based on the logarithm of the hypothesis is defined to minimize classification errors:

$$Err(h_{\theta}(x), y) = \begin{cases} -\log(h_{\theta}(x)) & \text{if } y = 1 \\ -\log(1 - h_{\theta}(x)) & \text{if } y = 0 \end{cases} \quad (6.3)$$

As seen in the black curves of Figure 6.1, making incorrect predictions with the Logistic Regression's cost function results in a high classification error while making correct predictions does not penalize the classifier. The cost function is then averaged across all m input-output combinations to define an objective optimization function:

$$J(\theta) = \frac{1}{m} \sum_{i=1}^m Err(h_{\theta}(x^{(i)}), y^{(i)}) \quad (6.4)$$

The derivative of this objective function finds the parameters θ that minimize the overall cost function. Because the cost function is convex, Logistic Regression classifiers avoid converging at local minima, enabling the classifier to reliably reach an optimal solution.²⁸ The optimal parameters are then used to draw a hyperplane decision boundary which best separates the two output classes based on a user-selected probability threshold.

Support Vector Machines (SVMs) are another form of linear, binary classification models. The SVM algorithm follows a similar procedure of minimizing an objective optimization function. The SVM cost function estimates the logarithm transform of the sigmoid function with a piecewise linear function as seen in the red function plotted in Figure 6.1.

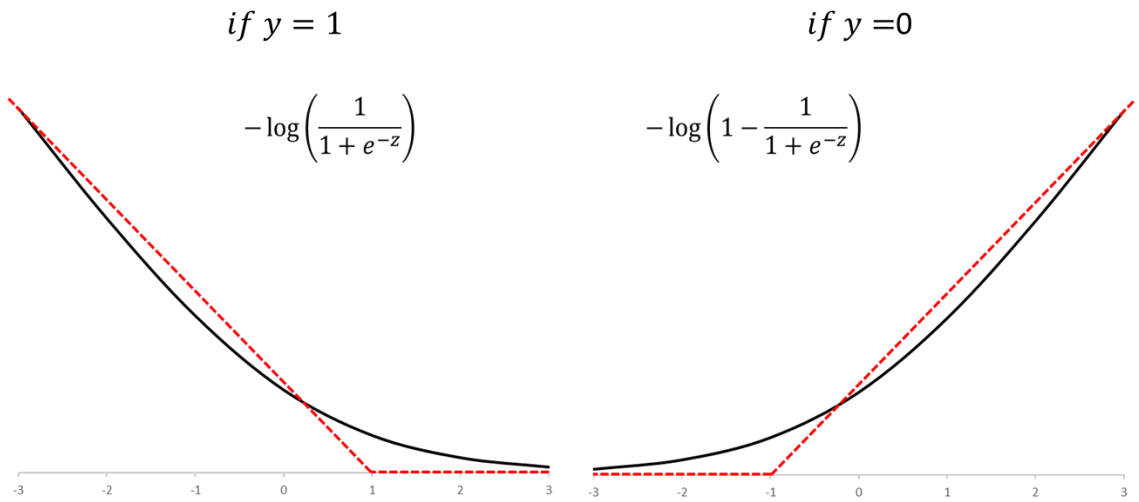


Figure 6.1. Cost functions for Logistic Regression (black) and SVM piecewise approximation (red).

Because the SVM cost function is an estimation of the Logistic Regression cost function, SVMs also converges to a global minimum. This eliminates the need for classifier retraining with different architectures.²⁸ The SVM algorithm is often referred to as a large margin classifier because it's objective is to define a decision boundary which maximizes the Euclidian distance from the boundary to specific data points referred to as support vectors. The support vectors are identified as the data points lying closest to the proposed hyperplane, and after optimization the margin between these support vectors and the decision boundary is optimized. While this process, as explicitly stated, is highly subjective to outliers, the SVM algorithm includes a regularization term which allows for adjusting the decision boundary's margin to reduce the influence of outliers and produce a more generalized decision boundary. An example of the linear separation of two classes can be seen in Figure 6.2.

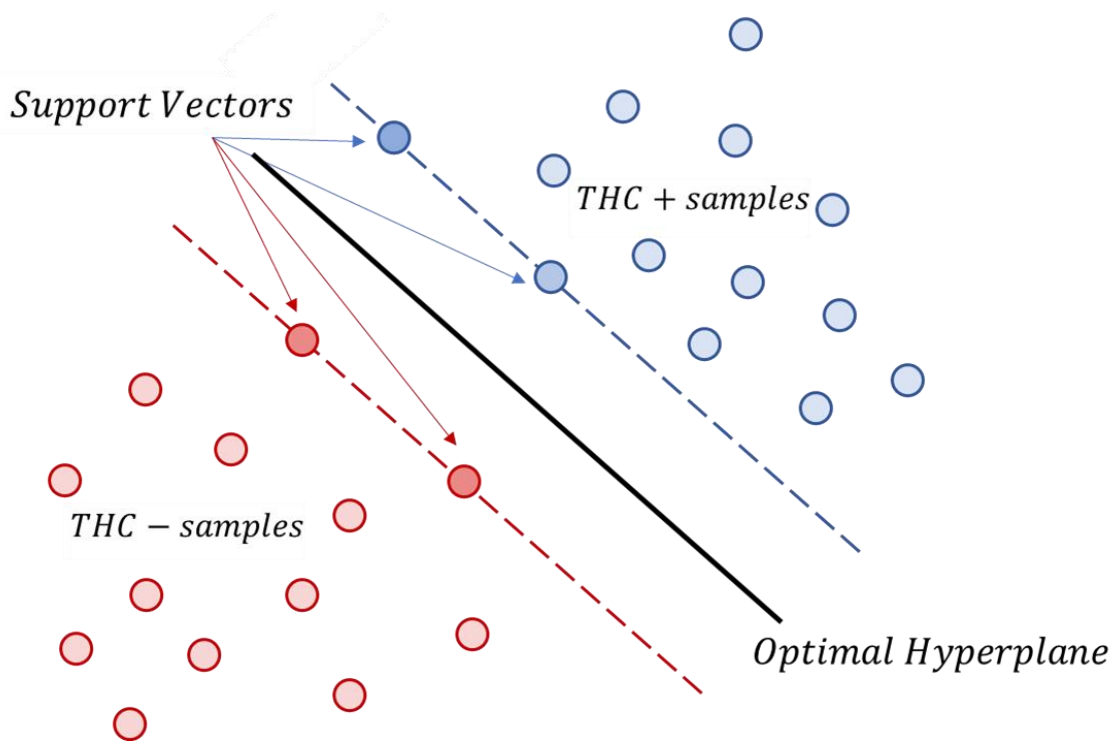


Figure 6.2. Linearly separable example of $THC +/ -$ binary classification by SVM with the optimal hyperplane defined by the maximum-margin between the red & blue dashed lines.

A “soft margin” SVM was implemented when fitting to the dataset.²⁸ The so-called “soft margin” introduces a parameter, C , that controls the influence of each individual support vector. C is a regularization parameter that adjusts the size of the margin for the classifier. Large values of C a lower-margin hyperplane is used, while a small value of C uses a large-margin classifier. This regularization parameter is particularly useful when there are outliers in the dataset.²⁸ The value of C was iteratively explored, however only the models with optimal C are presented.

One powerful advantage of SVM is that the algorithm can search in higher dimensional space to create non-linear decision boundaries using a kernel function.²⁸ The kernel function constructs a linear decision boundary in a high dimensional space then projects back down to the dimensions of the input space. The first SVM model explored in this paper used a linear kernel. Linear SVM assumes that the data are linearly separable in the input space (i.e. a line in 2D space, a plane in 3D space). The second SVM model used a radial bias function (rbf) kernel. The rbf kernel uses a gaussian distribution to describe the distance from the support vectors to the separating hyperplane,

allowing non-linear, curved decision boundaries to be drawn. The gamma parameter (specified only for the rbf kernel) is correlated to the inverse of the radius of influence of the chosen support vectors. As gamma increases and the radius of influence decreases the model becomes more susceptible to outliers and overfitting.

6.4 Results & Discussion

6.4.1 Characterization of Electrode Surface Modifications by Fourier-Transform Infrared Spectroscopy (FTIR) Analysis

Chemisorption of the DSP cross-linker and anti-THC antibody on the gold electrode surface was validated using FTIR. Gold thin films were deposited on PET substrates using e-beam vapor deposition at parameters mimicking those used for sensor fabrication and used for FTIR analysis. Functionalization of the electrode surface was carried out as described in the previous section. Prior to FTIR measurements, each sample was rinsed thoroughly with DI water then dried with N₂ air to rid the surface of any unbound material that may interfere with the analysis. The infrared spectra of surface modified samples were recorded with a Nicolet iS50 FTIR spectrometer. Absorbance spectral measurements were obtained with a scan resolution of 4 cm⁻¹ for 64 scans in the spectral range of 4000 cm⁻¹ to 600 cm⁻¹. Absorption spectra was recorded for PET-gold surface conjugated to DSP molecules, and the gold surface with anti-THC antibodies linked via the DSP linker molecules.

The absorbance peaks observed in the DSP spectrum of Figure 6.3 at 1786 cm⁻¹ and 1749 cm⁻¹ indicate the symmetric and asymmetric carbonyl stretches (respectively) of the NHS ester. Furthermore, the peak at 1212 cm⁻¹ confirm the presence of the asymmetric C-N-C stretch of the NHS ester while the peak at 1069 cm⁻¹ can be identified as the succinimide N-C-O stretch. Finally, the peak at 117 cm⁻¹ indicates the ester carbonyl stretch. The presence of these peaks is characteristic of a self-assembled monolayer of DSP, confirming the chemisorption of DSP to the gold surface.^{22,23}

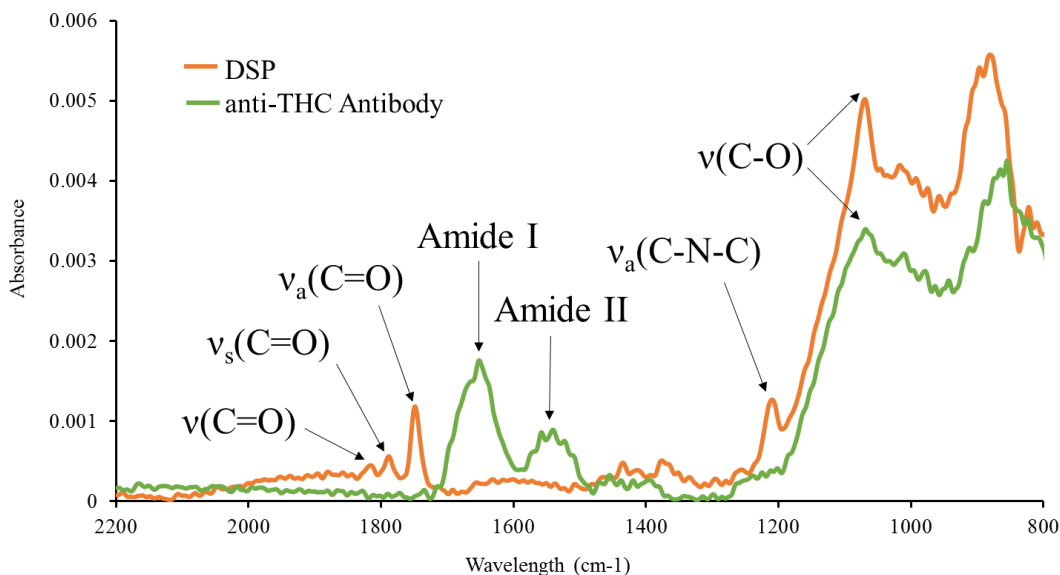


Figure 6.3. FTIR spectra of (a) DSP crosslinker immobilized on Au surface, (b) anti-ceftiofur antibody conjugated to DSP cross-linker.

The reaction between the NHS group with the antibody's primary amine group can be noted in the anti-ceftiofur spectrum. The C-O bonds of the NHS ester are broken and react with primary amines of the antibody, resulting in a stable amide bond.²³ A suppression of peaks associated with the NHS ester (1799 cm^{-1} , 1724 cm^{-1} , 1251 cm^{-1}) is observed, while peaks at $\sim 1644\text{ cm}^{-1}$ and $\sim 1552\text{ cm}^{-1}$ are indicative of amide I and amide II peaks. These results show a stable formation of the immunoassay through the binding of the anti-THC antibodies to the DSP functionalized surface.

6.4.2 Analysis of Zeta Potential as a Function of pH for the THC-BSA Hapten

A sigmoid curve was fit to the experimental Zeta potential values using the nonlinear regression model in GraphPad Prism (Figure 6.4). For the THC-BSA hapten the resulting sigmoid curve had an R-squared value of 0.9288, from which the isoelectric point was interpolated to be 3.756. An upper and lower 95% confidence interval was established for the sigmoid curve to estimate the bounds of the IEP which were 4.27 and 3.40. The sigmoid curve can be divided into three regions: steady positive zeta potentials, steady negative zeta potentials, and a transition phase. THC-BSA demonstrated positive zeta potentials (18.73 mV to 12.60 mV) at below pH 3, and negative zeta potentials (-5.67 mV to -12.26 mV) above pH 6. The transition phase of THC-BSA is between pH

3-5. The pH 3-5 phase is also the pH region in which the molecule is most unstable as its charge is closest to 0 mV.

To decouple the electrochemical nature of the hapten molecule, Zeta potential measurements were also taken under identical conditions with BSA proteins unconjugated to the THC biomarker. For the Zeta potential measurements on the BSA protein (no THC conjugation) a similar sigmoid curve was fit (R-squared value of 0.9785), to calculate its IEP of 4.53 with an 95% confidence interval bounds 4.85 and 4.21 (Figure 6.4). Reported theoretical and experimental IEP values for BSA are around 4.7 and 4.6 respectively^{32,33,34}.

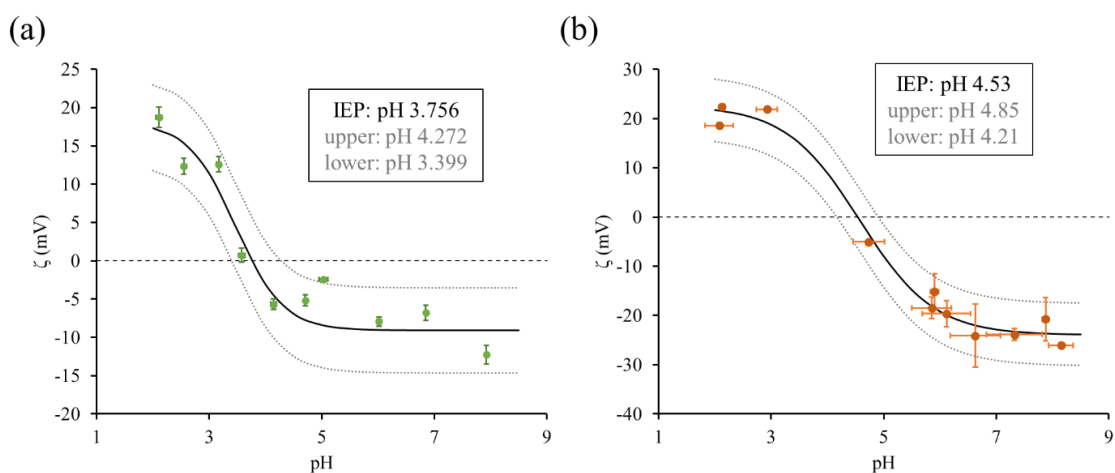


Figure 6.4 Zeta potential measurements in synthetic saliva at various pH for (a) the THC-BSA hapten and (b) BSA with no conjugation.

Very little overlap exists in the 95% confidence intervals for the extrapolated IEP values for THC-BSA and BSA, thus it is likely that the presence of the THC dominates the electrochemical signature of the THC-BSA hapten. This finding supports that the EIS signal response measured using the electrochemical biosensor is driven by the presence of the THC molecule and not the BSA. Additionally, the Zeta potential for the THC-BSA hapten shows a relatively stable response within the normal pH range of human saliva (6.2-7.6), indicating that the THC-BSA charge and stability should be relatively stable across samples.

6.4.3 Analysis of Dose-Dependent Response via Electrochemical Impedance Spectroscopy

The electrochemical response due to binding events of the THC-BSA were reported as Nyquist capacitance plots (Figure 6.4a-c) to resolve SAM dipolar characteristics and ionic permittivity. For

experiments conducted in 1x PBS, the Nyquist capacitance plots exhibits a higher frequency semicircle with a less pronounced, low-frequency semicircle emerging with increasing concentrations of the THC-BSA hapten. Each of the semicircles corresponds to a time constant indicating that the immunoassay experiences two relaxation events. As the THC-BSA biomarker is introduced onto the sensor surface, a consequent decrease in the large semicircle diameter is observed. The decrease in semicircle diameter corresponds to a change in the Debye relaxation process due to a lengthening of the immunoassay as well as hindrance of ionic ingress toward the electrode surface. As the concentration of THC-BSA bound to the surface increases, rotational hinderance increases, reducing the size and number of pin holes in the immunoassay. Impedance values were extracted at 10 Hz and normalized across replicates ($n=4$) by subtracting the Z^* of the 0-dose step from each dose step (Figure 6.4a inset). As higher doses are administered onto the sensor, an increase in the impedance response is observed. A similar trend is observed for the dose response experiment conducted in synthetic saliva at a pH of 6 (Figure 6.4b). As the hapten binds to the immunoassay a similar decrease in the high frequency semicircle diameter is observed with similar manifestation of a second low-frequency semicircle. When plotting the dose response at 10 Hz after normalizing to the 0-dose step (subtracting the Z^* of the 0-dose step from each dose step), the same trend was observed as the responses in 1x PBS and synthetic saliva at a pH of 6. This indicates that despite different capacitive processes dominating at the interface, the sensor can reliably detect varying doses of the THC-BSA hapten.

At a pH of 4 the dose response in the synthetic saliva exhibited slightly different interfacial characteristics as seen in Figure 6.4c. The Nyquist capacitance plots display a similar high frequency semicircle corresponding to the Debye relaxation of the immunoassay. However, the low-frequency response is dominated by the diffusion of ions to the electrode surface as indicated by the 45° diffusion tail. This could in part, be due to the surface charges of the THC-BSA hapten at pH values near it's IEP. The hapten exhibited only a weak surface charge at a pH of 4 ($\zeta \approx -5 \text{ mV}$), reducing the effect of the second Debye relaxation process and allowing the ionic diffusion to dominate the low-frequency response. However, a decrease in the higher frequency semicircle diameter is still observed, indicating that binding events of the THC-BSA hapten still play a role in the Debye relaxation process. While this pH lies outside of the normal salivary pH

range, and thus not indicative of a normal sample, it is important to note that large fluctuations in saliva pH can occur after eating, drinking, or in response to infection.

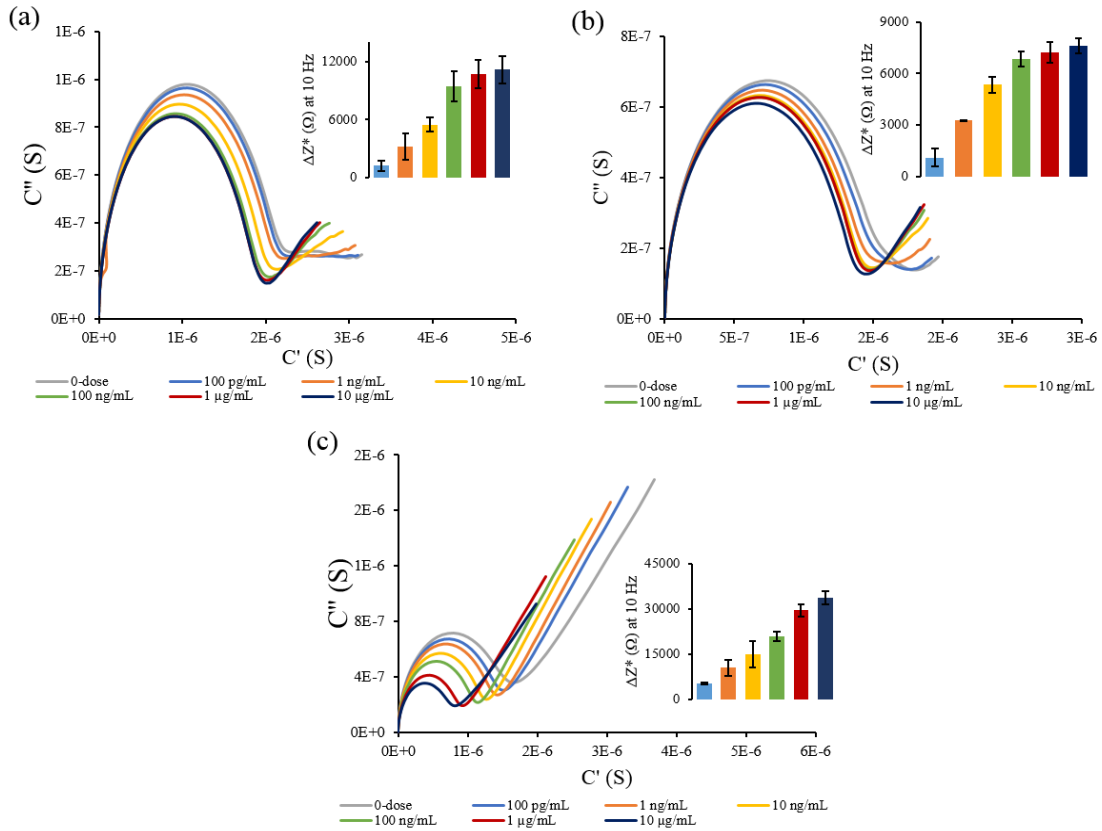


Figure 6.4. Calibrated dose response represented as Nyquist complex impedance plots with calibrated dose response inset for (a) 1x PBS (b) synthetic saliva at pH of 6 and (c) synthetic saliva at pH of 4. All inserts represent the change in imaginary impedance (with respect to the 0-dose step) extracted at 10 Hz.

6.4.4 Human Saliva Data Correlation

After assessing the sensor response in synthetic saliva, the sensor was tested on human saliva samples collected through the University of Texas at Dallas Institutional Review Board to assess its performance as a salivary DUI dataset. EIS measurements were taken again in response to the varying doses of THC, and correlation heatmaps were plotted in Figure 6.5 – Figure 6.7 to motivate the need for feature selection. The heatmaps demonstrate high correlation across each measurement type (i.e. Z^* values are highly correlated to Z^* values at nearby frequencies). The Z^*

& Z'' features between 1 Hz & 505 Hz show correlation coefficients of 0.7 and above, while the Z_ϕ coefficients vary between 0.3 & 1.0 within the same frequency range.

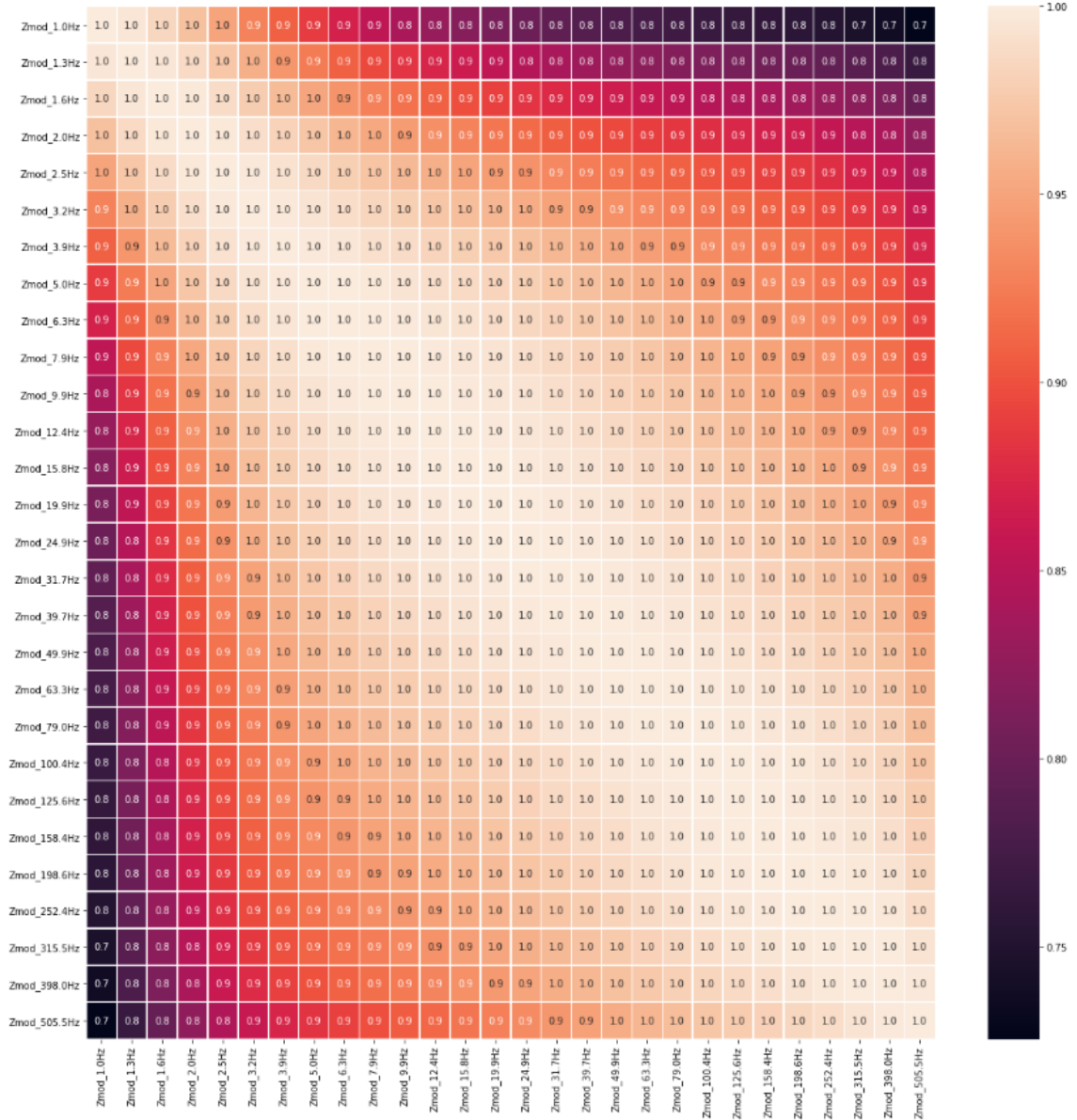


Figure 6.5. Correlation heatmap of Z^* data between 1 Hz and 505 Hz.

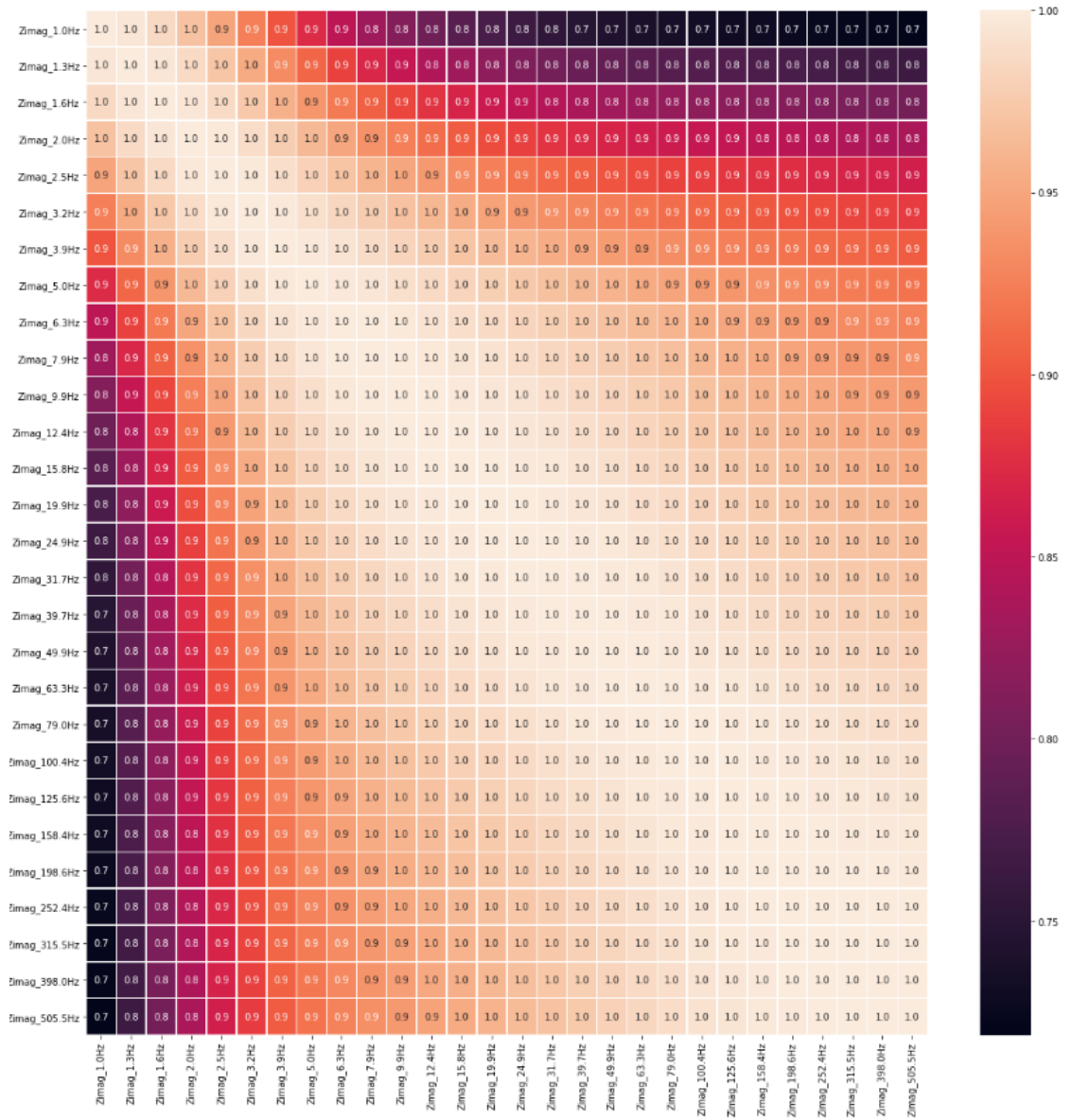


Figure 6.6. Correlation heatmap of Z'' data between 1 Hz and 505 Hz.

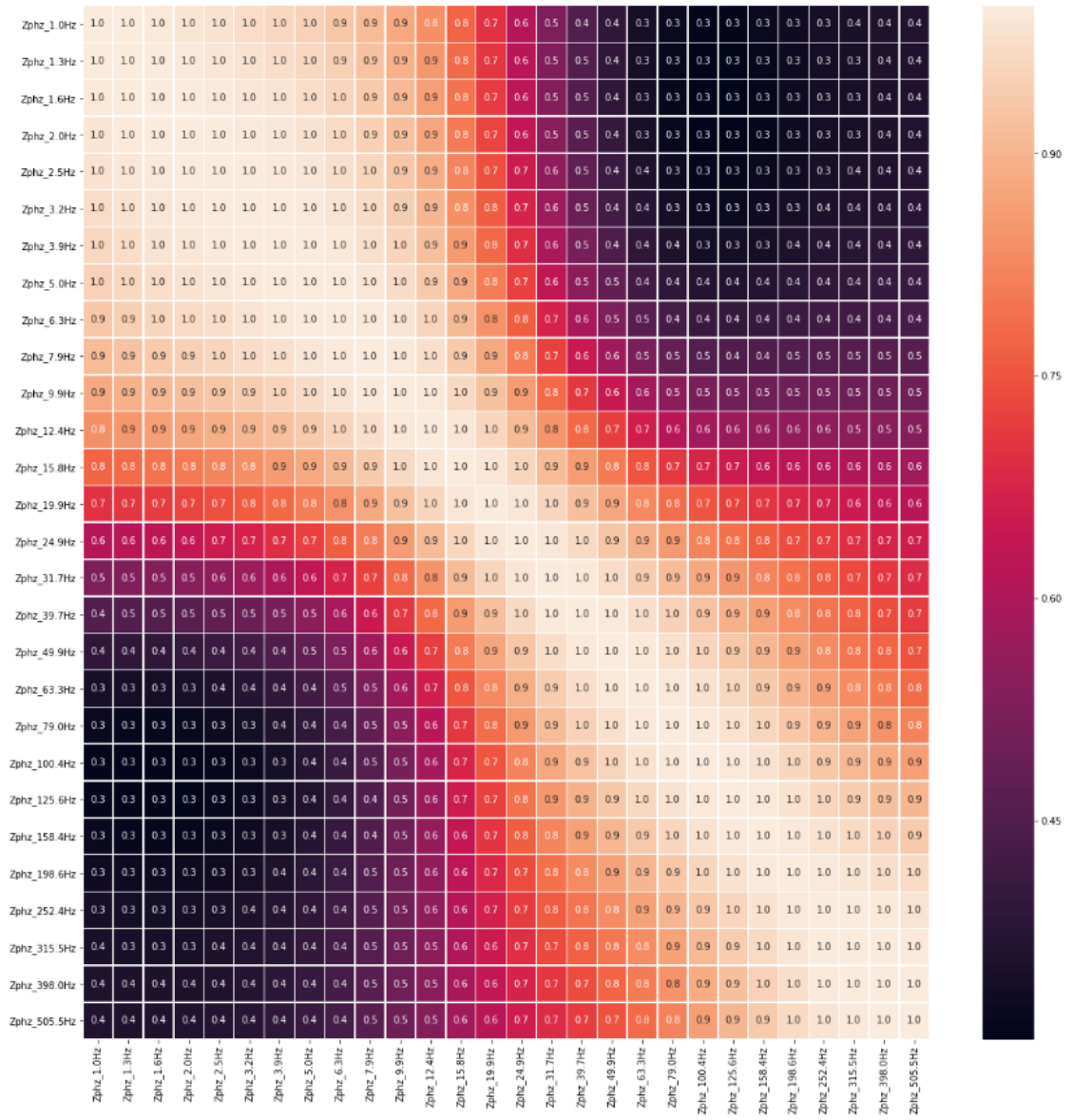


Figure 6.7. Correlation heatmap of Z_ϕ data between 1 Hz and 505 Hz.

6.4.5 Optimal Operational Frequency Selection via FCBF

Both a simple decision tree classifier and a Logistic Regression classifier were employed to test the performance before and after applying the FCBF algorithm. Decision trees are classifiers that search for the best location to split the data into pure groups given a random subset of features and inputs. The process begins in a root node where the model searches for the variable(s) with the largest information gain and splits the data accordingly into subsequent decision nodes. This process is repeated until a user-specified stop point, typically when any additional splits on the decision node would increase the node impurity (how often a randomly chosen element would be incorrectly labelled).³⁵ Decision trees are fast and easy to implement but are prone to overfitting the data when the feature space is too large, and a maximum tree depth is not specified. Here the depth of the decision tree was limited to 5, 10, or 15 decision nodes. To select the most predictive feature(s) the symmetrical uncertainty (SU) is used to determine the information gained by including an individual feature. The FCBF algorithm was also slightly modified to include the k best features (FCBFK). Decision tree algorithms are a good candidate for FCBF validation as the classification accuracy should improve when selecting features with the highest information gain.

The FCBF algorithm was evaluated separately first on the raw dataset, then on the dataset containing the impedance values normalized to the antibody step, and finally on the dataset containing impedance values normalized to the synthetic saliva step to select the most predictive feature from each. By removing noisy or correlated variables, FCBF selects a best performing feature with the goal of improving both the Decision Tree and Logistic Regression classifier accuracy and summarized below in Table 6.1. The FCBF algorithm improved the performance on both the raw impedance data and the data normalized to the synthetic saliva measurement by selecting a single feature from each of the sets: Z^* at 398.0 Hz and $\%dZ_\phi$ at 198.6 Hz – where Z^* represents the raw impedance modulus and $\%dZ_\phi$ represents the percent change in phase with respect to the synthetic saliva measurement.

Table 6.1. Classification accuracy of both Decision Tree and Logistic Regression on dataset with no feature selection and feature selection using FCBF and FCBFK algorithms.

	Raw Impedance Data (no normalization)		Normalized to Synthetic Saliva Measurement		Normalized to Antibody Measurement	
	Decision Tree	Logistic Regression	Decision Tree	Logistic Regression	Decision Tree	Logistic Regression
No Feature Selection	0.710	0.713	0.746	0.721	0.765	0.724
FCBF	0.901	0.845	0.824	0.813	0.699	0.632
FCBFK	0.820	0.702	0.652	0.813	0.742	0.746

However, the performance on the data normalized to the antibody measurement did not improve after reducing the feature space to a single feature. Results of the 5 best features from this dataset are shown in Figure 6.9. The dZ^* (change in impedance modulus with respect to the antibody measurement) at 505.5 Hz shows a bimodal distribution for the *THC* + class with the mean of the *THC* - class falling between both modes. This distribution of the data would greatly increase the complexity of the algorithm, so the dZ'' (change in imaginary impedance with respect to the antibody measurement) at 9.9 Hz was selected as the best feature for separating the data by class (*THC* +/-).

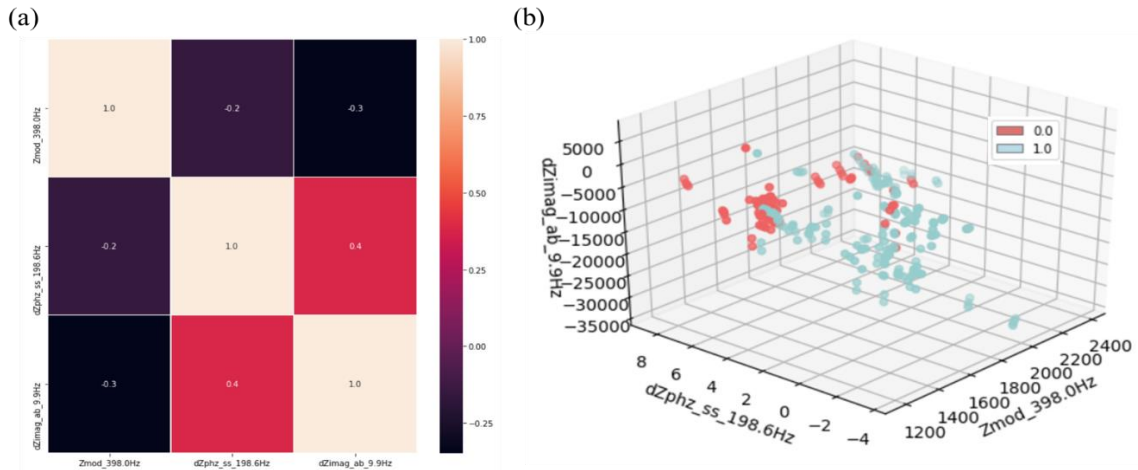


Figure 6.9. (a) Violin plots displaying normalized distributions and (b) correlation heatmap displaying Pearson’s correlation of the 5 features identified as most predictive by the FCBFK algorithm for the normalized to the antibody step.

The final three features selected after implementing the FCBF(K) algorithm were Z^* at 398.0 Hz, $\%dZ_\phi$ (wrt synthetic saliva) at 198.6 Hz, and dZ'' (wrt antibody) at 9.9 Hz. Figure 10a shows that none of these features are correlated to one another while Figure 10b demonstrates the dispersion of the data points in the reduced feature space.

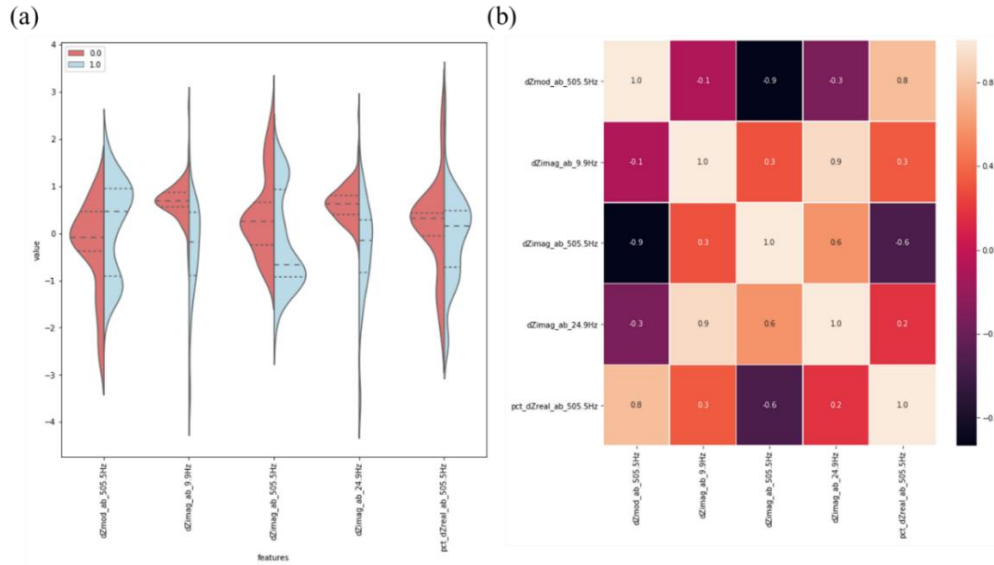


Figure 6.10. (a) Correlation heatmap and (b) 3D scatter-plot of final three selected features after the FCBF & FCBFK algorithms.

6.4.6 Binary Classification of THC +/- via Logistic Regression

Two Logistic Regression classifiers were constructed to make predictions on the data. The first logistic regression classifier was trained on a random subsample consisting of 80% of the input dataset with the remaining 20% held-out for model validation. The second logistic regression model implements cross-validation by partitioning the data into 10 equal bins using K-Folds cross-validation. The performance of each Logistic Regression model was evaluated on the data stored in the test dataset. Summaries of both the Logistic Regression and SVM classifiers are outlined below in Table 6.2.

When performing Logistic Regression without K-folds cross-validation the AUC was 0.911. This high AUC points toward relatively good generalizability, and at a classification threshold of 0.39 the TPR of the model is 97.1%. However, at this threshold the FPR was 60% indicating that the

majority of *THC* – samples were being misclassified. A threshold of 0.722 reduced the FPR to 15%. However, this comes as a trade-off when classifying the *THC* + samples; increasing the threshold decreases the TPR to 88.6%. The cross-sections of the 3D feature space (Figure 6.11b-d) demonstrates how the linear decision boundary fails to separate the data in the cross-sectional planes, and how misclassifications occur primarily among the *THC* – samples.

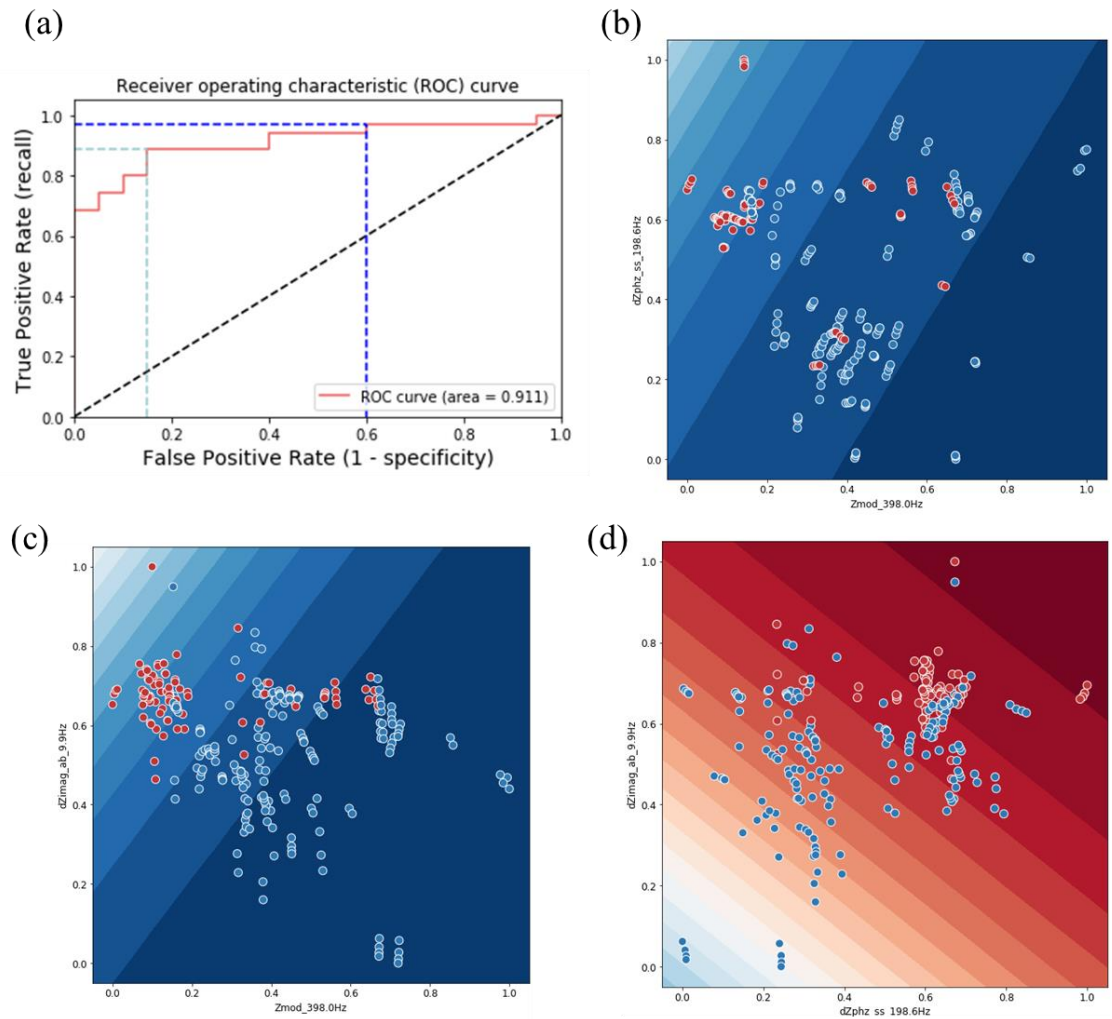


Figure 6.11. Logistic Regression classification performance metrics. (a) ROC curve with TPR and FPR identified at thresholds 0.303 (dark blue) and 0.769 (light blue). (b-d) 2D cross-sections of the classification probability.

The AUC was 0.916 for the Logistic Regression model using K-folds cross-validation. At a classification threshold of 0.303, again the model had a TPR of 97.1% and a FPR of 60%. By increasing the threshold to 0.769, the TPR and FPR decreased to 88.6% and 10% respectively. This indicates that using K-folds cross-validation, the model had slightly better performance at predicting the *THC* + samples, however the marginal increase in AUC demonstrates that the general performance was not significantly improved. The cross-sections of the 3D feature space (Figure 6.12b-d) show only slight variation in the decision boundary from the Logistic Regression without K-folds cross-validation.

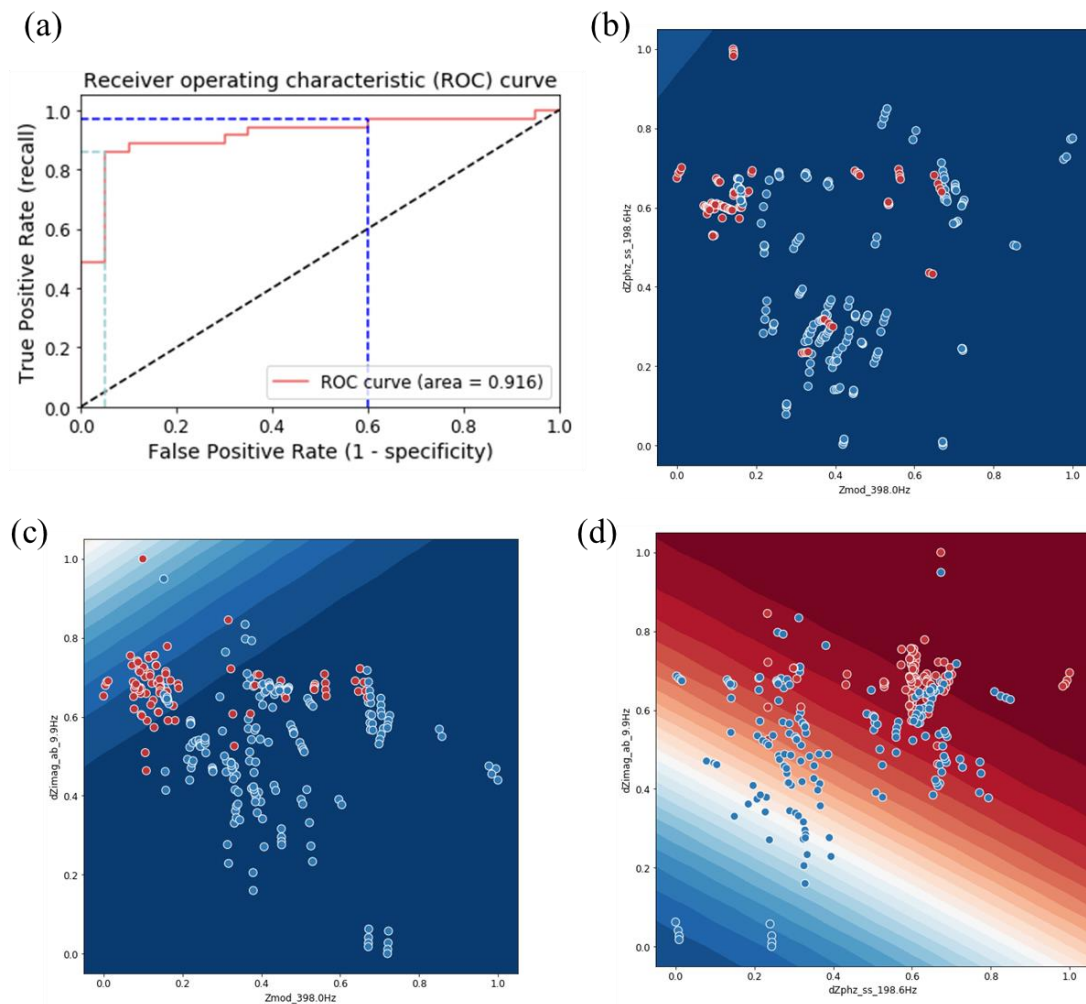


Figure 6.12. Logistic Regression classification performance metrics. (a) ROC curve with TPR and FPR identified at thresholds 0.303 (dark blue) and 0.769 (light blue). (b-d) 2D cross-sections of the classification probability.

6.4.6 Binary Classification of *THC* +/- via Support Vector Machines

In each of the SVM models, the kernel type and the regularization parameter C were passed as additional inputs for the SVM algorithm (gamma was also specified for the rbf SVM). For the linear kernel SVM a regularization parameter of $C=1$ was set to reduce the impact of outlier data points when fitting the hyperplane. Other values of C were explored, however there were no significant changes in the model performance. The rbf kernel SVM used a C value of 100. While this reduces the margin size, a low value for the gamma parameter (set to 10) was used to discourage overfitting by increasing the radius of influence of the support vectors.

The linear kernel SVM was nearly identical to the first Logistic Regression model. Both models had similar ROCs with equivalent AUCs. This does not come as a large surprise, as SVM uses a linear approximation of the Logistic Regression cost function. Both models showed similar TPR and FPR (at slightly different cut-off thresholds), however a linear kernel SVM did not perform better than Logistic Regression with K-folds cross-validation. The cross-sections of the 3D feature space (Figure 6.13b-d) after linear kernel SVM demonstrate a similar decision boundary to the Logistic Regression models. However, it is important to note that the decision boundaries are not in the exact same location.

The rbf kernel SVM had the highest overall model performance and generalizability. As seen in Figure 6.14b-d, most of the *THC* – data points are clustered in a spherical region. Circular decision boundaries better grouped the two classes as indicted by the AUC (0.951). Furthermore, at a threshold of 0.621 the TPR and FPR for the rbf SVM were 97.1% and 15% respectively. The FPR reduced to 5.0% by increasing the threshold to 0.797 while only reducing the TPR to 94.3%.

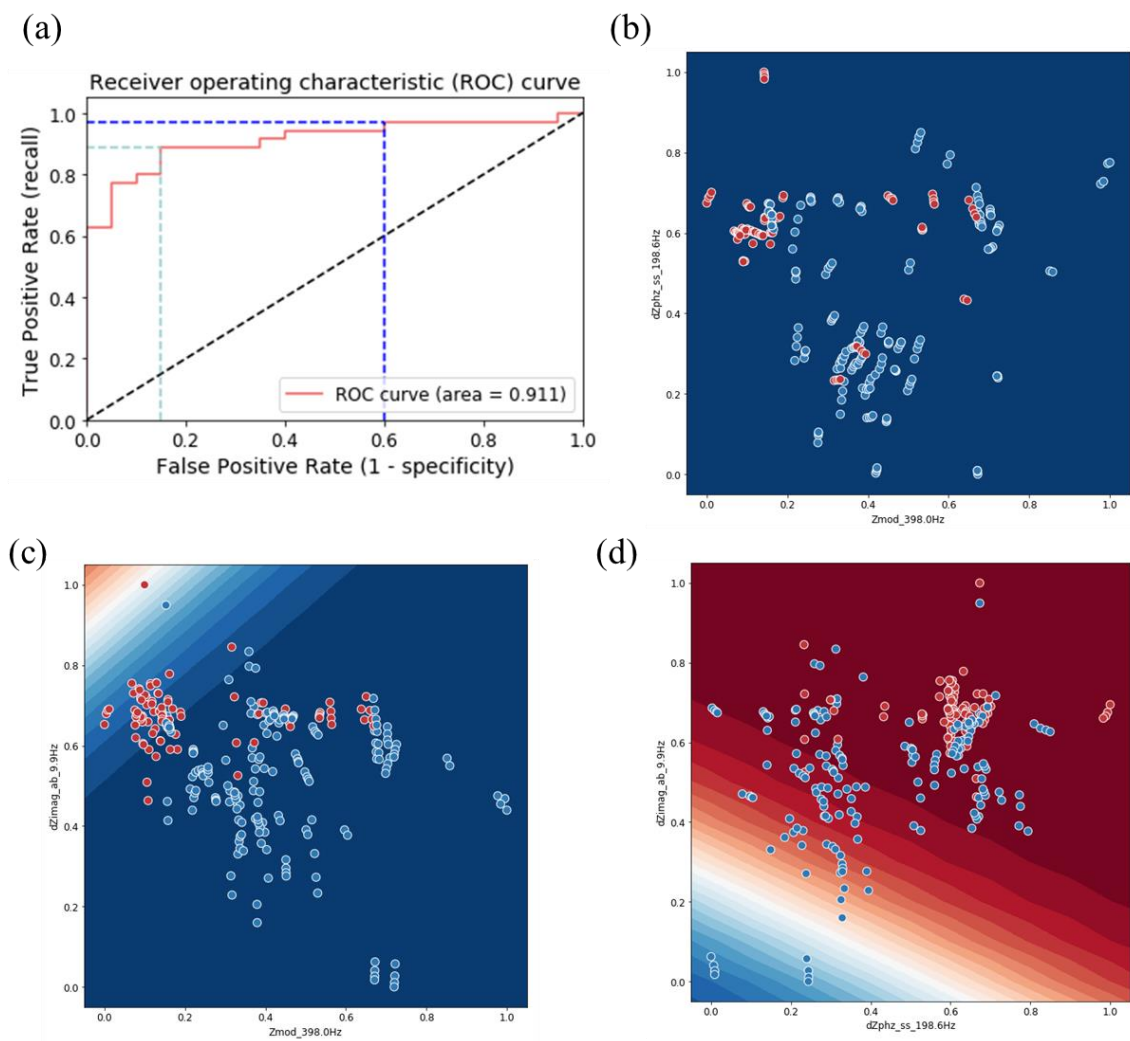


Figure 6.13. Linear kernel SVM classification performance metrics. (a) ROC curve with TPR and FPR identified at thresholds 0.214 (dark blue) and 0.829 (light blue). (b-d) 2D cross-sections of the classification probability.

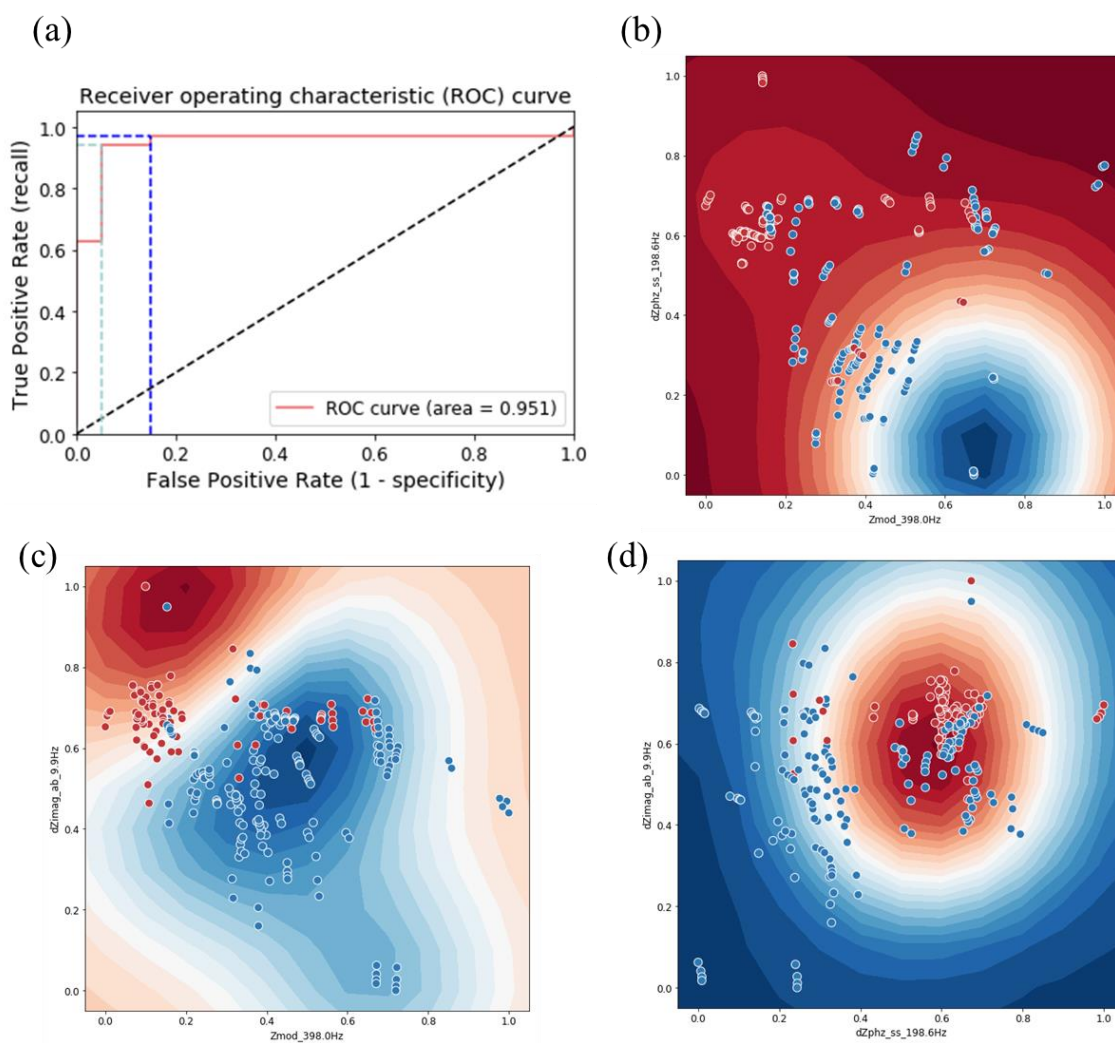


Figure 6.14. Rbf kernel SVM classification performance metrics. (a) ROC curve with TPR and FPR identified at thresholds 0.621 (dark blue) and 0.797 (light blue). (b-d) 2D cross-sections of the classification probability.

Table 6.2. Performance summary of Binary Classification Algorithms

Classifier Name	AUC	Threshold	TPR	FPR
Logistic Regression	0.911	0.39	97.1	60.0
		0.722	88.6	15.0
Logistic Regression with K-folds cross-validation	0.916	0.303	97.1	60.0
		0.769	88.6	10.0
Linear kernel SVM	0.911	0.214	97.1	60.0
		0.829	88.6	15.0
Radial Bias Function kernel SVM	0.951	0.621	97.1	15.0
		0.797	0.943	5.0

6.5 Conclusion

We have developed a biosensor capable of detecting THC spiked within human saliva samples. This paper utilizes non-faradaic EIS to rapidly detect the THC-BSA hapten with high specificity and sensitivity. Machine Learning algorithms were employed to determine the optimal operating frequencies as well as evaluate the sensor's performance characteristics. An rbf kernel SVM algorithm was used to perform binary classification on samples of collected human saliva, resulting in a very high general performance (AUC = 0.951) at predicting the presence of THC. Because salivary THC concentrations correlate strongly with intoxication from marijuana, this technology could serve law enforcement as a rapid, DUI breathalyzer-equivalent for detecting recent marijuana consumption. Additionally, this biosensor could serve concerned parents or family members as a home test kit to identify suspected marijuana consumption by children.

6.5.1 Future Work

This paper identifies a highly sensitive and highly specific biosensor when detecting the THC-BSA hapten biomarker. Future studies would seek evaluating the saliva of participants who have recently smoked or consumed marijuana directly rather than spiking the biomarker. The pre-trained SVM model can be deployed to make predictions on these samples to determine if any refinement in the algorithm or pre-processing is required.

While the work presented here focused on binary classification to identify the presence of THC, a different learning algorithm could be selected to perform a regression analysis and predict concentrations of THC in saliva. A regression analysis could help identify a more accurate measurement of THC's intoxicating effects and establish more precise cut-off limits for activities like driving under the influence. Another cannabinoid present in marijuana, cannabidiol, greatly impacts the psychoactive effects of THC. Thus, multiplexed detection of cannabidiol alongside THC would likely give a better idea of the subject's intoxication level.

6.6 References

1. Pacher, P., Bátkai, S. & Kunos, G. The Endocannabinoid System as an Emerging Target of Pharmacotherapy. *Pharmacol. Rev.* 58, 389 LP-462 (2006).
2. Marzo, V. Di, Bifulco, M. & Petrocellis, L. De. The endocannabinoid system and its therapeutic exploitation. *Nat. Rev. Drug Discov.* 3, 771 (2004).
3. Huestis, M. A. Human Cannabinoid Pharmacokinetics. *Chem. Biodivers.* 4, 1770–1804 (2007).
4. Ashton, C. H. Pharmacology and effects of cannabis: A brief review. *Br. J. Psychiatry* 178, 101–106 (2001).
5. KP, H. Medical marijuana for treatment of chronic pain and other medical and psychiatric problems: A clinical review. *JAMA* 313, 2474–2483 (2015).
6. Hill, K. P. Medical Marijuana: More Questions than Answers. *J. Psychiatr. Pract.* 20, 389–391 (2014).
7. Controlled Substances Act, 21 U.S.C §§ 802 (1990).
8. Lopez-Quintero, C. *et al.* Probability and predictors of transition from first use to dependence on nicotine, alcohol, cannabis, and cocaine: Results of the National Epidemiologic Survey on Alcohol and Related Conditions (NESARC). *Drug Alcohol Depend.* 115, 120–130 (2011).
9. Hall, W. & Degenhardt, L. Adverse health effects of non-medical cannabis use. *Lancet (London, England)* 374, 1383–1391 (2009).
10. Aldworth, J. (2013). *Results from the 2013 National Survey on Drug Use and Health: Summary of National findings*. DIANE Publishing.
11. Volkow, N. D., Baler, R. D., Compton, W. M. & Weiss, S. R. B. Adverse Health Effects of Marijuana Use. *N. Engl. J. Med.* 370, 2219–2227 (2014).
12. Wanklyn, C. *et al.* Disposable screen printed sensor for the electrochemical detection of delta-9-tetrahydrocannabinol in undiluted saliva. *Chem. Cent. J.* 10, 1 (2016).
13. Hartman, R. L. & Huestis, M. A. Cannabis Effects on Driving Skills. *Clin. Chem.* 59, 10.1373/clinchem.2012.194381 (2013).

14. Asbridge, M., Hayden, J. A. & Cartwright, J. L. Acute cannabis consumption and motor vehicle collision risk: Systematic review of observational studies and meta-analysis. *BMJ* 344, 1–9 (2012).
15. Walsh, J. M. *et al.* Epidemiology of alcohol and other drug use among motor vehicle crash victims admitted to a trauma center. *Traffic Inj. Prev.* 5, 254–260 (2004).
16. Drummer, O. H. Drug Testing in Oral Fluid. *Clin. Biochem. Rev.* 27, 147–159 (2006).
17. Hamilton, H. E. *et al.* Cocaine and benzoylecgonine excretion in humans. *J. Forensic Sci.* 22, 697–707 (1977).
18. Lee, D. *et al.* Oral Fluid Cannabinoids in Chronic, Daily Cannabis Smokers during Sustained, Monitored Abstinence. *Clin. Chem.* 57, 1127 LP-1136 (2011).
19. Huestis, M. A., Mitchell, J. M. & Cone, E. J. Detection times of marijuana metabolites in urine by immunoassay and GC-MS. *J. Anal. Toxicol.* 19, 443–449 (1995).
20. Karimi, A., & Dweik, B. Design and Development of Electrochemical Analyzer for Detection of Δ^9 -Tetrahydrocannabinol (THC). *Meeting Abstracts* (No. 42, pp. 2433-2433). The Electrochemical Society (2018).
21. Niedbala, R. S. *et al.* 2001_Niedbala_Journal of Analytical Toxicology_Detection of marijuana use by oral fluid and urine. 25, (2001).
22. Pensa, E. *et al.* The Chemistry of the Sulfur–Gold Interface: In Search of a Unified Model. *Acc. Chem. Res.* 45, 1183–1192 (2012).
23. Lim, C. Y. *et al.* Succinimidyl ester surface chemistry: Implications of the competition between aminolysis and hydrolysis on covalent protein immobilization. *Langmuir* 30, 12868–12878 (2014).
24. Munje, R. D., Muthukumar, S. & Prasad, S. Lancet-free and label-free diagnostics of glucose in sweat using Zinc Oxide based flexible bioelectronics. *Sensors Actuators B Chem.* 238, 482–490 (2017).
25. Yu, L., & Liu, H. Feature selection for high-dimensional data: A fast correlation-based filter solution. In *Proceedings of the 20th international conference on machine learning (ICML-03)* (pp. 856-863) (2003).
26. Senliol, B., Gulgezen, G., Yu, L. & Cataltepe, Z. Fast Correlation Based Filter (FCBF) with a different search strategy. *2008 23rd Int. Symp. Comput. Inf. Sci. Isc. 2008* (2008). doi:10.1109/ISCIS.2008.4717949

27. Metz, C. E. Basic principles of ROC analysis. *Semin. Nucl. Med.* 8, 283–298 (1978).
28. Mountrakis, G., Im, J., & Ogole, C. Support vector machines in remote sensing: A review. *ISPRS Journal of Photogrammetry and Remote Sensing*, 66(3), 247-259 (2011).
29. Cortes, C. & Vapnik, V. Support-Vector Networks. *Mach. Learn.* 20, 273–297 (1995).
30. Cawley, G. C. & Talbot, N. L. On Over-fitting in Model Selection and Subsequent Selection Bias in Performance Evaluation. *J. Mach. Learn. Res.* 11, 2079–2107 (2010).
31. Mountrakis, G., Im, J. & Ogole, C. Support vector machines in remote sensing: A review. *ISPRS J. Photogramm. Remote Sens.* 66, 247–259 (2011).
32. Salgin, S. Effects of ionic environments on bovine serum albumin fouling in a cross-flow ultrafiltration system. *Chemical Engineering & Technology: Industrial Chemistry-Plant Equipment-Process Engineering-Biotechnology*, 30(2), 255-260 (2007).
33. Salgin, S., Salgin, U., & Bahadir, S. Zeta potentials and isoelectric points of biomarkers: the effects of ion types and ionic strengths. *Int. J. Electrochem. Sci.* 7(12), 12404-12414 (2012).
34. Salis, A., Boström, M., Medda, L., Cugia, F., Barse, B., Parsons, D. F. & Monduzzi, M. Measurements and theoretical interpretation of points of zero charge/potential of BSA protein. *Langmuir*, 27(18), 11597-11604 (2011).
35. Dietterich, T. G. Ensemble methods in machine learning. In *International workshop on multiple classifier systems* (pp. 1-15). Springer, Berlin, Heidelberg (2005).

CHAPTER 7

CONCLUSION & FUTURE WORK

This dissertation has presented a prototype of a highly sensitive, rapid-response biosensor with applications across a wide array of markets and industries. The biosensor is also easily transmutable to leverage Faradaic or non-Faradaic processes when detecting the targeted biomarker. This research has contributed toward 1) exploring a methodical biosensor design strategy 2) determining the optimal detection modality across an array of biomarkers in complex matrices 3) evaluating sensor performance characteristics by applying un-biased evaluating criterion. We have laid the groundwork for a highly versatile platform that can implement various electrochemical measurement techniques and achieve highly sensitive and selective outputs.

Each of the sensing platforms explored in this dissertation have demonstrated the detection of a single biomarker in a complex matrix. To expand on the robustness of this biosensing platform, the sensor design could be modified to promote multiplexed biosensing of 2 or more biomarkers in the same sample. Selective functionalization of electrodes can allow for capture probes (e.g. antibodies) to be isolated at a single working electrode in a multi-electrode array. Multiplexed biosensing would give a more complete view of the condition being detected whether it be GMO proteins, wheat pathogens, antibiotics in meat, or cannabinoids in saliva. Additionally, we hope to utilize the algorithms developed in Chapter 5 on another dataset to determine the model's generalizability at binary classification. The algorithms used on the THC dataset can easily translate across matrices, across biomarkers, and across detection techniques to make un-biased predictions. We would also like to explore other machine learning techniques such as clustering concentrations into pre-defined ranges (i.e. low medium and high [THC]) or regression analysis to predict concentrations directly (i.e. $[\text{THC}] = 10.5 \text{ ng/mL}$). The platform presented in this dissertation has demonstrated repeatable, permutable, and highly specific affinity-based biosensing, and is a promising prototype toward the advancement of point-of-use biosensors.

BIOGRAPHICAL SKETCH

Hunter Stevenson graduated from Saint Louis University with a Bachelor of Science in Biomedical Engineering in 2014. During his undergraduate studies he worked in Dr. Silviya Zustiak's Soft Tissue Engineering Laboratory and Dr. Daniel S. Zahm's research lab in the Department of Pharmacological and Physical Sciences. His research under Dr. Zustiak focused on developing mathematical models to describe hydrogel fabrication, geared toward drug delivery and tissue engineering applications. In Dr. Zahm's lab he worked on mapping the GABAergic pathway within the basal forebrain through locomotion and risk/reward experiments. After graduating from Saint Louis University Hunter spent a year teaching Algebra and Geometry to high school students in Taipei, Taiwan at Kang Chiao International School. In August of 2015, Hunter joined the Biomedical Microdevices and Nanotechnology Lab at The University of Texas at Dallas as a graduate researcher to pursue his PhD under the supervision of Dr. Shalini Prasad. His research interests lie in developing highly customizable electrochemical biosensors to detect biomarkers in complex matrices and enhancing sensor performance through more powerful analytical techniques for both non-Faradaic and Faradaic affinity-based biosensors. In 2019 Hunter will begin working as a Senior Engineer at Cytovale Inc. a Series B start-up in San Francisco developing a microfluidic diagnostic device for early sepsis detection.

CURRICULUM VITAE

Hunter S. Stevenson, Ph.D.

HUNTER.STEVENSON@UTDALLAS.EDU

www.linkedin.com/in/HunterStevenson

EDUCATION

Doctor of Philosophy, Bioengineering

Thesis Defense Date: Fall 2018

The University of Texas at Dallas, Richardson, TX

GPA 3.9

Awards & Honors: Jonsson Family Graduate Student Ambassador (2018), U.S. NSF Travel Grant (2018), Graduate Teaching Assistant of the Year (2018), Jonsson Family Graduate Fellowship (2017), Phi Kappa Phi Honor Society (2017), Graduate Teaching Assistantship (2015)

Bachelor of Science, Bioengineering

May 2014

Saint Louis University, St. Louis, MO

GPA 3.3

Awards & Honors: Parks College of Engineering Dean's Scholarship (2010), Parks College Dean's Honor List (2013, 2014), Billiken Scholar Athlete (2011 – 2013)

RESEARCH EXPERIENCE

Graduate Research Fellow, The University of Texas at Dallas August 2015 – December 2018

Biomedical Microdevices and Nanotechnology Laboratory

Advisor: Dr. Shalini Prasad, Associate Department Head for Bioengineering

- Develop handheld electronics to test novel biosensor platform for consumer health & wellness working toward high impact, first-author journal publications
- Design experiments and implement supervised machine learning classification and dimensionality reduction algorithms in MATLAB & Python to analyze sensor output
- Perform clinical subject testing through Institutional Review Board to establish saliva sensor feasibility
- Lead interdisciplinary teams to develop protocols resulting in novel detection modalities
- Presented both GMO biosensor and marijuana saliva swab at international conferences to a private audience of over 100 attendees, resulting in an increase in external collaborations

Regulatory Advisor, The University of Texas at Dallas

January 2018 – June 2018

Medical Devices Regulations & Regulatory Strategies

Advisor: Dr. Diana Easton, Clinical Professor

- Consulted with client, Steven Leeds, M.D., on both short- and long-term marketing objectives
- Prepared *De Novo* application toward FDA approval for novel medical device
- Reviewed SOPs to enhance design control and risk management processes including ISO 14971

Research Assistant, Saint Louis University

May 2013 – May 2014

Soft Tissue Engineering Lab

Advisor: Dr. Silviya Zustiak, Associate Professor

- Organized lab expendables database to streamline purchasing and better manage budget
- Documented research objectives and challenges, improving hydrogel fabrication methodologies
- Quantified relationship between fabrication techniques for tunable hydrogels toward drug delivery and tissue engineering applications

Research Assistant, Saint Louis University

May 2013 - May 2014

Lab of Pharmacological and Physiological Sciences

Advisor: Dr. Daniel Zahm, Associate Professor

- Developed and utilized novel and conventional animal behavioral testing paradigms assessing patterns of organization in basal forebrain structures
- Prepared and analyzed cryostat brain sections for neural interconnectivity

TEACHING EXPERIENCE

Graduate Teaching Assistant

August 2015 -

Present

UT Dallas Bioengineering Department, Dallas, TX

- Lecture and evaluate student performance on static system mechanics
- Facilitate learning and improve engineering skills during weekly office hours

Mathematics Teacher

August 2014 - July 2015

Kang Chiao International School, Taipei, Taiwan

- Developed curriculum and lesson plans raising average test scores for Algebra and Geometry students
- Organized and oversaw 3D printing/AutoCAD Design Club stimulating student interest in STEM careers

JOURNAL PUBLICATIONS

H. Stevenson, N.R. Shanmugam, A.P. Selvam, and S. Prasad. The Anatomy of a Non-Faradaic Electrochemical Biosensor, *SLAS Technology*, (2017)

S. Subramanian, R.A. Reichard, **H. Stevenson**, Z.M. Schwartz, K.P. Parsley, D.S. Zahm. Lateral preoptic and ventral pallidal roles in locomotion and other movements, *Brain Structure & Function*, (Submitted Feb 21, 2018)

S.Sheth, E. Jain, A. Karadaghy, Syed, S., **H. Stevenson**, & S.P. Zustiak, (2017). UV Dose Governs UV-Polymerized Polyacrylamide Hydrogel Modulus. *International Journal of Polymer Science*, 2017.

CONFERENCE PROCEEDINGS

Stevenson, H. Chary, P. Pin, J. Bacon, A. Nagaraj, V.J. Prasad, S. *Handheld GMO Biosensor*. Poster session accepted for the annual meeting of the Biomedical Engineering Society, Atlanta, GA. October 2018

Stevenson, H. Chary, P. Pin, J. Bacon, D. Kinnamon, A. Nagaraj, V.J. Prasad, S. *Handheld GMO Biosensor*. Oral presentation accepted for the annual meeting of the World Congress on Biosensors, Miami, FL. June 2018

Stevenson, H. Kinnamon, D. Prasad, S. *Rapid DUI Saliva Swab for THC Detection*. Poster session accepted for the annual meeting of the World Congress on Biosensors, Miami, FL. June 2018

Stevenson, H. Chary, P. Pin, J. Bacon, A. Nagaraj, V.J. Prasad, S. *Handheld GMO Biosensor*. Poster session accepted for the annual meeting of the Society for Laboratory Automation and Screening, San Diego, CA. February 2018

Stevenson, H. Kinnamon, D. Prasad, S. *Rapid DUI Saliva Swab for THC Detection*. Poster session presented at the annual meeting of the Biomedical Engineering Society, Phoenix, AZ. October 2017

TECHNICAL SKILLS

Software: Matlab, Python, Visual Basic (Excel), SPICE, COMSOL, Prism, Origin, R, AutoCAD, SolidWorks, C/C++, Zview, Echem Analyst

Fabrication & Characterization Tools: Physical vapor deposition, photolithography, atomic force microscopy, scanning electron microscopy, profilometry, 3D printing, Fourier transform infrared spectroscopy, Wet-lab skills, ELISA & microplate readers, UV/Vis spectroscopy, & Zetasizer